INFORMATION TO USERS

This manuscript has been reproduced from the microfilm master. UMI films the text directly from the original or copy submitted. Thus, some thesis and dissertation copies are in typewriter face, while others may be from any type of computer printer.

The quality of this reproduction is dependent upon the quality of the copy submitted. Broken or indistinct print, colored or poor quality illustrations and photographs, print bleedthrough, substandard margins, and improper alignment can adversely affect reproduction.

In the unlikely event that the author did not send UMI a complete manuscript and there are missing pages, these will be noted. Also, if unauthorized copyright material had to be removed, a note will indicate the deletion.

Oversize materials (e.g., maps, drawings, charts) are reproduced by sectioning the original, beginning at the upper left-hand corner and continuing from left to right in equal sections with small overlaps. Each original is also photographed in one exposure and is included in reduced form at the back of the book.

Photographs included in the original manuscript have been reproduced xerographically in this copy. Higher quality 6" x 9" black and white photographic prints are available for any photographs or illustrations appearing in this copy for an additional charge. Contact UMI directly to order.

.

NOTE TO USERS

The original manuscript received by UMI contains pages with indistinct and/or slanted print. Pages were microfilmed as received.

This reproduction is the best copy available

UMI

UNIVERSITY OF OKLAHOMA

GRADUATE COLLEGE

HEAVENLY METAL: A STUDY OF NEUTRON-CAPTURE ELEMENT ABUNDANCES IN METAL-POOR GALACTIC HALO STARS

A Dissertation

SUBMITTED TO THE GRADUATE FACULTY

in partial fullfillment of the requirements for the

degree of

Doctor of Philosopy

By

Debra L. Burris

Norman, Oklahoma

1998
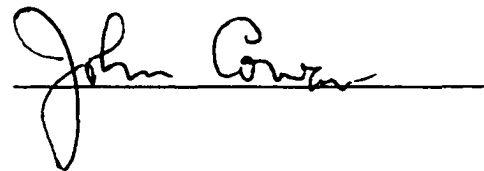
HEAVENLY METAL: A STUDY OF NEUTRON-CAPTURE ELEMENT

ABUNDANCES IN METAL-POOR GALACTIC HALO STARS

A Dissertation APPROVED FOR THE

DEPARTMENT OF PHYSICS AND ASTRONOMY

BY

ACKNOWLEDGEMENTS

Chapter I: "In the Beginning..."

"...Seek, then,

no learning from the starry men,

Who follow with the optic glass

the whirling ways of stars that pass."

W.B. Yeats

A. Introduction

Everything is the Universe is made up of elements that exist in stars. Some elements, such as H, He and Li were formed at the time of the formation of the Universe in the Big Bang. The elements up to the Fe peak are formed during a star's lifetime in fusion processes. What about the elements that are heavier than Fe? Where do they come from? They must come from different processes than those previously mentioned, since they are much lower in abundance than the elements lighter than the iron peak elements (see Figure 1.1, Anders & Grevesse 1989).

The majority of the atomic nuclei above the Fe peak are formed during neutron capture processes. The presence of these processes was suspected when Merrill (1952) saw Technetium (Tc) in S-type stars. Tc has no stable isotopes and the half-life of the longest lived isotope is only about 2 million years. It takes the S-type stars approximately 10^7 years to evolve to the giant branch, so any Tc that was present at the formation of the stars would have already decayed. Therefore the Tc must have been synthesized in the stars during their lifetimes. One positive aspect of the extensive nuclear testing in the late 40's and 50's was the determination that this synthesis was due to capture of neutrons on seed nuclei. There are two distinct processes which are distinguished

from one another by the time scale for neutron capture (n-capture) versus the time scale for β decay. If the neutron density is low enough to permit β decay before the next n-capture, this is the slow (s-)process. The isotopes that result from the s-process exist near the valley of β stability, the narrow mass region where stable isotopes of each element exist. If the densities are high enough that there is not sufficient time for decay before the next n-capture, this is the rapid r-process. This process forms isotopes that are far from stability in the highly radioactive regime. Most isotopes are not formed exclusively in one of these processes, but are a combination of both (Cameron 1982, Käppeler et al. 1989, Wisshak et al. 1996).

The r-process will be the primary focus of this dissertation. This process is of particular importance for several reasons. Firstly, it is the r-process that is responsible for the formation of the long-lived nuclear chronometers ^{232}Th, ^{235}U, ^{235}U, and ^{244}Pu. Also, the r-process provides insight into the temperature and density conditions of the explosive events (possibly supernovae) that are sites for this process. Lastly, understanding the operation of the r-process provides information about the chemical evolution of the Galaxy.

B. Nuclear Physics

Two studies in the 1950's helped lay the groundwork for the connection between the nuclear physics which describes these processes and the stellar evolution astrophysics which explains the observed abundances. Burbidge, Burbidge, Fowler, and Hoyle (1957) and Cameron (1957) identified and defined these processes for the first time as responsible for the formation of the heavy (n-capture) elements. Although some of the work in these papers has now been improved upon, much of it still stands, and these two papers serve as the starting point for all work in n-capture element nucleosynthesis.

Abundance peaks occur at closed neutron shells occur, around mass numbers 50, 82, 126, where there are neutron "magic" numbers. The magic number of neutrons is a very stable configuration for the nucleus. The closed shells have small neutron capture cross-sections, making the capture of another neutron very unlikely. Also, nuclei with even mass numbers have a smaller cross-section for neutron capture than odd-number nuclei, causing peaks at even numbers (i.e/, the odd-even effect). The s-process has peaks at mass numbers 87, 138, and 208 with a strong odd-even effect. However, the r-process has peaks at mass numbers 80, 130, and 195 with no apparent odd-even effect. The odd-even effect is not observed in the r-process signature. Most isotopes are not formed exclusively in one of these processes, but are a combination of both as demonstrated in Figure 1.2 (see Appendix 1, also Anders & Grevesse 1989, Käppeler et al.1989).

Meyer (1994) provides an excellent review of the recent progress in understanding the physics involved in the n-capture processes. The requirements for the two processes are quite similar: a source of free neutrons and seed nuclei to capture these neutrons. The s-process uses Fe peak nuclei formed earlier by nuclear fusion. The r-process, on the other hand, occurs at the same time that the seed nuclei are formed, by bombarding the newly formed Fe-peak nuclei with lighter nuclei.

The r-process is believed to operate in the following scenario. A system consisting of free nucleons, light nuclei, and Fe-group nuclei at high temperature exists in nuclear statistical equilibrium (NSE). As this system expands, the temperature will drop. This drop in temperature will cause the slowing down of some nuclear reactions. When the reaction rates become too low, equilibrium will be lost and these reactions are said to experience "freeze out". The first reactions to freeze out are the charged-particle reactions (i.e. electrons, protons, etc.). The n-capture reactions can continue unimpeded. The nuclei that are present after the charged-particle reactions

3

cease will eventually capture all the free neutrons.

For the r-process to occur, a very high neutron density is needed. This means that there will be many neutrons available for the seed nuclei to capture after the freezeout of the charged-particles. This doesn't mean however, that the nuclei can continue adding neutrons with wild abandon. Eventually, a nucleus will have so many neutrons added to it, that the binding energy for the next capture will be negative. This nucleus, which is unable to capture any more neutrons until it β-decays, is said to have reached neutron drip. The system will reach an equilibrium between captures and photo-disintegration. Once the nucleus β-decays, causing the nucleus' charge to increase, further neutron captures are allowed.

The s-process is not a freezeout process, but rather the system never quite makes it to NSE. The system never reaches NSE because the timescale to reach equilibrium is too long compared to the dynamical timescale of the system and the conditions needed to obtain the high numbers of photons (e.g., very high temperatures). Light nuclei are being synthesized into heavier nuclei, but the system never achieves NSE. The seed nuclei are provided by the progenitor stars and free neutrons come from fusion products. The two reactions responsible for liberation of neutrons are $^{13}C(\alpha,n)^{16}O$ and $^{22}Ne(\alpha,n)^{25}Mg$. In order to fit the solar system s-process distribution, there must be more than one neutron exposure. The main component, which produces nuclei in the mass range 90<A<204, requires a neutron exposure of 0.30 mb^{-1} (1 barn (b)= 10^{-24} cm^2). Another exposure of 7.0 mb^{-1} contributes to the A$\leq$90 s-nuclei abundances. The presence of these two components indicates that two separate sites contribute to the abundance of solar s-nuclei.

C. From Whence it Came

The s-process site is believed to be well understood. The main component is created in the helium burning shell of an asymptotic giant-branch (AGB) star (see

4

Meyer 1994 for extensive references). This star's structure consists of an inert carbon-oxygen core, over which there exists a convective helium burning shell. Over this burning shell there is a hydrogen-rich convective envelope atop a hydrogen burning shell. The ^{12}C processed in the helium burning shell is the source for the neutrons via ^{12}C(p, γ)^{13}N(β^+,ν)^{13}C. When the helium shell turns off, dredge up of these carbon nuclei allows them to combine the protons in the hydrogen envelope to produce ^{13}C which would then provide the neutrons to drive the s-process.

The helium shell governs the timescale for these processes to occur. The helium burning in the core is interupted by pulses, while between these pulses, the hydrogen burns in a thin shell. The helium shell is thin and unstable, therefore the helium shell burning takes place in pulses or flashes. These helium burning pulses last on the order of tens of years, and the interpulse periods are thousands of years. When the helium burning pulse begins, there is tremendous release of energy causing the hydrogen-burning shell to shut off and the envelope to become convective. While the hydrogen burning shell is off, dredge-up of the processed material that was in the inter-shell region can occur. The processed material is moved to the surface of the star by the overlapping convection regions, where it is observed. Once the processed material reached the surface, it is ejected into the interstellar medium (ISM) via a wind from the star's surface. Alternatively, the material that cannot make it to the surface during the stars lifetime can be released into the ISM at the time of planetary nebula ejection. Gallino et al. (1998) perform a test of this site, which confirms the plausibility of the this as the main s-process site.

The weak s-process component occurs in a different site altogether. It is believed to come from the He burning in the cores of massive stars ($\geq$15M$_\odot$) (Truran & Iben 1977, Lamb et al. 1977, Rateri et al. 1991). It is hot enough in these stars for the ^{22}Ne(α, n)^{25}Mg reaction to produce a significant amount of neutrons. The material

is ejected from the star into the ISM via winds. The fact that these stars are much more massive than the stars responsible for the main component of the s- process implies that this component will be incorporated into the ISM at earlier times in the Galaxy's history.

Unfortunately, the site of the r-process is not as well understood. Burbidge et al. (1957) suggested that the process could be associated with supernovae (SNe), since these events could provide the extreme temperatures and neutron densities needed in a short timescale. However, they suggested that the site would be the Type I SN, believing that the production of Cf^{254} powered the observed light curves. Later, is was found that nickel was in fact responsible for the shape of the Type I light curves, not californium. Cameron (1957) considered the mass cut of the SN Type II as potential site for the r-process. The mass cut is the boundary between the matter that gets ejected into space and the matter that is left behind in the remnant of the massive star after it has undergone core collapse. This site is still considered one of the most promising, because the distribution of the material ejected in the models gives a reasonably good fit to the solar system r-process distribution (Meyer 1994 and references therein).

The first models of the r-process were hampered by inadequate nuclear data and insufficient knowledge of the astrophysics of the potential sites. New ideas were needed. Instead of assuming steady flow, Seeger, Fowler, & Clayton (1965) assumed $(n,\gamma) \rightleftarrows (\gamma,n)$ equilibrium and used a β-decay reaction network. Improved nuclear data allowed Seeger et al. (1965) to fit more (but not all) of the r-process distribution features. However, to fit the distribution they considered two sites, one of short duration ($\simeq$ 4s) and another of longer ($\geq$ 4s) duration. Before better fits could be obtained, improvements in the understanding of the both the astrophysics of the core collapse and the nuclear physics of the neutron capture reaction were

needed.

Schramm (1973) also used a dynamical r-process model, and demonstrated that after the majority of the neutrons had been captured during the "freeze out", $(n,\gamma) \rightleftarrows (\gamma,n)$ equilibrium was no longer valid. Schramm also showed if nonequilibrium processes were taken into account, the odd-even effects created by $(n,\gamma) \rightleftarrows (\gamma,n)$ equilibrium could be smoothed out naturally during the freeze out. Previous authors had to use nonphysical approaches to account for the smoothing. Schramm (1973) also suggested that the observed r-process distribution could successfully be produced by one site, rather than several sites as previously suggested by Seeger et al. (1965).

Cowan, Cameron, and Truran (hereafter CCT) took a new approach to understanding the physics of the r-process in a series of papers from 1978 to 1985, prompted by the anomalies in the inclusions of the Allende meteorites. These inclusions were enhanced contributions of the r-process odd isotopes of Nd and Ba. Instead of assuming that steady-state conditions exist, they did a dynamical r-process calculation. This scenario considers rapidly changing neutron density, rather than the longer time scale for density changes considered by Burbidge et al. (1957) and Cameron (1957). In a previous paper, Cameron and Truran (1977) had suggested that the primitive solar nebula contained the products of nucleosynthesis from SN. This r-process enrichment in the meteorite along with failure of previous SN models to reproduce the solar r-process distribution prompted CCT to consider the helium zone of a supernova as a site for the r-process. This had been previously suggested by Burbidge et al. (1957) but they had suggested the Type I supernovae, from lower mass stars. CCT considered the Type II supernovae, which are due to higher mass stars. Specifically, they examined the effect of a shock wave passing through the He region of the pre-supernova star. One difficulty faced by CCT is

7

that lack of a consistent and complete source of nuclear data. The data used in CCT comes from a myriad of different sources, since there simply did not exist a source from which all the data could be obtained. Unfortunately, this inconsistency introduces errors in the calculated values.

In calculating their r-process paths, CCT considered the following points: 1) n-capture cross-sections, 2) β decay half-lives, 3) β-delayed neutron emission rates, and 4) fission effects. There are several fission related effects which must be considered. First, fission can stop the r-process path at $Z \simeq 92$ and prevent production of the superheavy elements. Also, as the neutron density declines, the r-process will eventually freeze out, and the nuclei will be free to undergo β-decay and β-delayed fission. Lastly, if there is a long duration of neutron exposure, "fission cycling" can occur, where the fission products themselves can capture neutrons and form more heavy nuclei, which in turn will undergo fission. The penultimate paper in this series (Cowan, Cameron, & Truran 1985) allowed some important conclusions to be drawn. The dynamical r-process calculations provided a more satisfactory fit to the observed solar system r-process distribution than the older steady-state calculations. However, the site chosen for these processes to occur (the helium zone), was discovered to be unsatisfactory, since the required ^{13}C concentration to produce the necessary neutron density was inconsistent with realistic predictions of stellar evolution models. Cowan, Thielemann, & Truran (1991) present a summary of the dynamical r-process calculations as well as a discussion of possible r-process sites.

Mathews, Bazan, and Cowan (1992) tested several of the possible sites of the r-process by comparing predicted abundance outputs from the various sites to abundances observed in several of the surveys presented in the next section. The fit of their models to the observed stellar Eu/Fe ratio showed that the r-process elements increased along with iron over the history of the Galaxy, thus ruling out a

pregalactic primordial origin for the majority of the r-process elements. Also, the correlation of the europium and iron abundances at early times or low metallicities indicates that these two elements were likely formed in the same type of objects. Based on goodness-of-fit to the data, Mathews et al. (1992) suggest the low mass SN II (7-8 $M_\odot$) are the most probable sites. The model still remains one of the most popular candidates. However one problem with confirming this as the r-process site is that the astrophysics of the core collapse itself is not well understood, and the mass distribution of the material in the ejecta is model-dependent.

Numerous other sites have been proposed for the r-process, including binary neutron star mergers (Symbalisty & Schramm 1982) ejecting neutron rich material, neutron star-black hole (NS-BH) interactions (Lattimer & Schramm 1974,1976), and the winds of nascent neutron stars (Meyer 1994). In the NS-BH scenario, the neutron star is disrupted by the black hole and part of the neutron stars material is ejected. As the material is decompressing, the r-process can take place. In the wind scenario, the neutron star is the remnant of a Type II SN. The wind has a high photon to baryon ratio, therefore frequent photodissociation occurs in the wind, generating large numbers of free neutrons. As the material in the wind cools, the nuclei that remain are exposed to a region of very high neutron density ($\simeq 10^{20} cm^{-3}$), thus driving the r-process. This potential site provided abundances which were a good match with the solar system distribution as well (Meyer 1994). Again, the problem with all of these proposed sites is the lack of understanding of the mechanism. In the midst of all this uncertainty, one thing can be stated with relative certainty: The r-process is produced in the same relative proportions every time, which will lead to an interesting result (see Chapter III).

Cowan et al. (1998) have made new r-process calculations using improved nuclear data, again assuming the classical waiting-point approximation of $(n,\gamma) \rightleftarrows (\gamma,n)$.

The model is site independent, consisting of a continuous superposition of r-process components with a varying r-process path related to neutron separation energies in the range 2-4 MeV (determined by neutron number density and temperature). The fit is adjusted by changing the weight of individual components for different separation energies and time duration for the constant conditions of density and temperature. They reproduced the solar isotopic abundances in detail including the heaviest isotopes of Pb and Bi. Even though this model is site independent, the conditions that must exist to produce the curve can be used to suggest possible sites.

D. Seeing is Believing

One of the first important observational studies of these n-capture elements was done by Spite and Spite (1978). This study focused on the abundances of these elements in metal-poor ([Fe/H]$\leq$-1.5) halo stars. These metal-poor stars are an excellent choice for studying n-capture abundances, since the low level of iron in these stars allows the much weaker features of n-capture elements to be detected. Also, many of these stars are in an advanced evolutionary state (i.e. giants) which makes them brighter, and thus easier to observe. Also, another advantage of giants is that the atmospheres are of such low density that effects of microturbulent velocity on the strength of the lines are (almost) negligible. As we shall see later, since these halo objects are presumed to be quite old, their abundances will give important clues about the history of the nucleosynthesis early on in the Galaxy and the chemical evolution of the halo.

The Spites' study observed four very metal-poor stars (HD 122563, HD 128279, HD 84903, and HD 184711). Also, they gleaned information about seven other stars from various literature sources. HD 122563 is a very well observed star since it is quite bright, and hence is often used as a "standard star" in many halo star surveys. They took the raw spectra from the seven literature stars and the abundances

were re-established using the same analysis techniques as used on the four new observations. The temperatures were determined using the (R-I) color index for each star. When the temperature was determined, the ionization equilibrium of iron, titanium and chromium were used to determine the stars' gravity. The only r-process element that was observed in the stars was Eu, via the 4129 Å line. The analysis of the Eu line included consideration of the hyper-fine splitting of the line due to the contributions of the two odd isotopes of Eu. They observe that the Eu/Fe ratio seems to remain about the same early on in the Galaxy's history and suggest that the r-process takes place at the same time as that of silicon burning that forms Fe nuclei. They also observed the s-process element Ba in the program stars. The Spites pointed out that there seemed to exist an initial Ba enrichment at the beginning of the life of the Galaxy. They suggested that this could be due to an initial enrichment from massive short-lived stars that existed in the halo before the collapse of the disk. These stars would have manufactured their Ba via the r-process rather than the s-process. The Spites hinted at this by commenting that the Ba seemed to track with the Fe production as a squared function rather than linear as was expected.

Since the Spites' study, there have been many observational studies on this population of stars. One of the most important observational catalogs of halo stars was done by Luck and Bond (1981). Their catalog of 36 metal-poor field red giants was the starting point for many of the abundance analysis papers that were written in the late 1980's and early 1990's. Luck and Bond obtained their spectra with the 4m telescopes at Kitt Peak (KPNO) and Cerro Tololo (CTIO). This study consisted of several papers describing the reduction of the data and establishment of parameters for some 18,000 lines for these stars. They noticed that the s-process elements (e.g. Ba) were underabundant in these extremely metal poor stars, but

that they were present. The explanation offered by Luck and Bond for the presence of these s-process elements was that the high mass stars that lived early on in the Galaxy's lifetime must have been producing these elements via the s-process. Truran (1981) pointed out that the observed abundances of these s-process elements in fact matched the solar system r-process distribution. Therefore, the stars were in fact producing these s-process elements via the r-process.

Sneden and Parthasarathy (1983) observed the famous (or infamous) HD 122563 at the McDonald Observatory 2.7m telescope and found many new spectral features for these n-capture elements in the UV. Since this star is extremely metal-poor ($[Fe/H] \simeq -2.7$), the usually inaccessible lines in this UV region were able to be observed. They adopted a lower temperature and gravity than used by Spite and Spite (1978) and Luck and Bond (1981), but point out that for these weak lines, the choice of temperature and gravity has little effect on the final abundance. They found that the s-process elements Ba, La, Ce, Pr, Nd, and Sm were deficient by nearly a factor of 10 compared to the Sun. The r-process elements Eu, Gd, Dy, Er, and Yb were found to be less deficient, but still were found in lower abundance than they are observed in the Sun. A consequence of these conditions was that there was no s-process model which could reproduce the observed Ba/Eu ratio. Sneden and Parthasarathy suggest that this ratio could be reproduced by the solar system r-process, as suggested by Truran (1981).

Sneden and Pilachowski (1985) present a study of HD 110184 compared to Sneden and Parthasarathy's (1983) analysis of HD 122563. The spectra for HD 110184 were obtained at the KPNO 4m telescope using a Cassegrain echelle spectrograph. They also obtained identical spectra for HD 122563, for use as comparison. These stars are quite similar, therefore a comparison between them would point out any star-to-star variation in the abundances of the n-capture elements. To perform the analysis,

Sneden and Pilachowski chose to take mean values of the atmospheric parameters and used this set of values for both stars. They adopted the following parameters for both stars $(T_{eff}/logg/[Fe/H]/v_{micro})=(4700K/1.20/-2.6/2.3$ km sec^{-}1). Their analysis for the n-capture elements found that the abundances of these elements in HD 110184 were much larger than those in HD 122563. The abundances in HD 110184 were a nearly perfect match to the r-process abundance curve. Although they tried several s-process models in an attempt to match the observed abundances, all of them failed to reproduce the observations, just as in Sneden and Parthasarathy (1983). Sneden and Pilachowski also pointed out that although the r-process curve fits the elements from Ba-Pr well, it underproduces Sr and Zr. This difficulty in understanding the behavior of strontium and zirconium has yet to be resolved in the observational surveys, and seems to indicate that the r-process as we understand it may not be responsible for the production of these elements early in the Galaxy's history.

Gilroy et al. (1988) published abundance results for 20 very metal-poor halo stars. The observations were done at the KPNO 4m and the McDonald 2.7m telescopes. The abundance analyses were done using MOOG (Sneden 1973), an LTE line analysis program which shall be used extensively in the results from Chapters II, III, and IV. This study included stars previously analyzed by Sneden and Parthasarathy (1983) (HD 122563) and Sneden and Pilachowski (1985) (HD 110184). The results obtained by Gilroy et al. were in excellent agreement with these previous studies. A more interesting result was found for the star HD 115444. This star was previously believed to be a "barium star" (Griffin et al. 1982), meaning that it seemed to have an enhanced Ba abundance compared to the abundance of other n-capture elements. The new analysis performed by Gilroy et al. showed that HD 115444 was not a barium star, and in fact the abundances of this star matched the solar system

r-process abundances (scaled for metallicity). Another interesting result in Gilroy et al. is the scatter plot of average n-capture abundance to Fe abundance. This plot demonstrates that at early times in the Galaxy's history there does exist real star-to-star variation in the abundances of these elements. Chapter III contains a more extensive discussion of this star-to-star scatter and how it relates to the current survey presented therein.

A very large survey of 1044 metal-poor stars was done by Beers et al. (1992). This survey was approximately 66% main-sequence turnoff stars, with the balance being first ascent Giants and AGB stars. This is an important survey since it quadrupled the number of observed stars with [Fe/H]$\leq$-2.0. Also, it increased the number of observed stars with [Fe/H]$\leq$-3.0 by *sevenfold*, so this impressive survey provided many opportunities to study extremely metal deficient stars. Norris et al. (1993) used four stars from the Beers et al. (1992) survey. These stars were all in the metallicity range from -4.2 to -3.2. Their analysis results are typical of past results except that the Sr results couldn't easily be matched to the r-process abundance distribution. This is a problem which still continues to plague us, and as of yet has no good explanation.

Butcher (1987) used the Th/Nd ratio from 18 F and G dwarfs, ranging in metallicity from -1.5 < [Fe/H] < 0.5, to determine the Galactic age. Although ^{232}Th is radioactive, it has a half-live of 14 billion years and therefore it is useful as a chronometer. Using the Th II λ4019.129 line and the Nd II λ41018.823 line, Butcher obtained a Galactic age limit of 9.6 billion years, assuming a constant production rate. If an exponentially decaying production rate was assumed, ages of 11-12 billion years were achieved. Both of the ages are lower than the accepted age of the Galaxy, achieved by other methods (e.g., globular clusters). However, there were a few inconsistencies in Butcher's analyses, which were addressed in Morell, Källander, and

14

Butcher (1992). Firstly, the Th II feature suffers from blending by Co I λ4019.126, which was not considered in the 1987 paper. Secondly, there is an unidentified line at λ4019.10 which had not been included in the previous investigation. Based upon the re-analysis of the Butcher (1987) data and more carefully determining the Nd abundance Morell et al. (1992) state that the large scatter in the [Th/Nd] ratio prevent any age determinations from being made. The Th/Nd ratio was the not the best choice of ratio to use since Th is formed exclusively in the r-process while Nd is formed almost equally by the r- and s-processes. A better choice would be to use an entirely r-process ratio, such as Th/Eu, as seen in Cowan et al. (1998a,b) for the metal-poor halo stars CS22892-052 and HD 115444. Pagel (1993) used the [Th/Eu] ratio to estimate the age of stars from the Butcher (1987) sample in addition to stars from other samples to compare the age of the halo to ages determined from the HR diagram of globular clusters. Pagel (1993) obtained ages for the stars on the order of 15 Gyr which did agree with the globular cluster ages.

François, Spite, & Spite (1993) also observed the Th/Eu ratio in metal-poor halo stars. They find that the behavior of the Th/Fe ratio as a function of metallicity mimics the behavior of the Eu/Fe ratio down to a metallicity of $\simeq$ -2.3. However, below this value, François et al.'s (1993) data seems to show that the Th/Eu ratio becomes oversolar, indicating that the two elements were not evolving in the same way. Although more data is this regime is need to confirm this statement, if it is proved correct, this statement weakens the use of the Th/Eu ratio as an age indicator.

Gratton and Sneden (1994) observed 19 stars with a metallicity range of -2.80$\leq$ [Fe/H]$\leq$0.0. As with other authors in the past, Gratton and Sneden found that the elements that were formed primarily via the s-process were overdeficient in the metal-poor stars compared to the r-process elements.These observations provided

data in the "in-between" range of metallicity that ties the halo stars to the disk stars.

McWilliam et al. (1995 a,b) analyzed 33 extremely metal deficient stars (-4.0≤[Fe/H]≤-2.0) from the Beers et al.(1992) survey. Of these 33 stars, 14 had both Eu and Ba. McWilliam et al. found the [Eu/Ba] ratio to be very close to the solar system r-process values and again found an intrinsic dispersion in the n-capture abundance results from star to star. They suppose that this dispersion must be primordial in origin because it cannot be explained by and s-process contribution either by self-contamination or by binary mass transfer. The dispersion must come from the range in the supernovae (SN) yields in the n-capture elements and from the inhomogeneity of the Galactic material early in the Galaxy's lifetime. Also, this survey first introduces CS22892-052, the star that is the focus of Chapter II of this work. McWilliam et al. did not consider that hyperfine splitting (HFS) would affect the abundances derived for the Ba lines in the 1995 paper. McWilliam (1998) reanalyzed the Ba abundance of these stars, taking this hyperfine splitting into account. The data from this new analysis is presented in Chapter III, and a full discussion of the effects of HFS is presented in Chapter II.

Woolf et al.(1995) observed Eu in 81 Disk F and G dwarf stars from the Edvardsson et al. (1993) survey. These stars provided data at the near solar metallicity range with all stars in the survey having a [Fe/H]≥-1.0. Again, [Eu/Ba] was found to increase with decreasing metallicity, due to the domination of the r-process at low metallicity. Their figure 13 shows the dispersions early on in the Eu abundance with a tighter correlation later on, providing further confirmation of the star-to-star scatter proposed by Gilroy et al. (1988). These stars are also included in the analysis section of Chapter III of this work.

Magain (1995) used the analysis of the barium isotopic ratio in the metal-poor

subgiant HD 140283 to determine what process was in operation early in the Galaxy's history. Chapter II has a full discussion of the effect of isotopic splitting in Ba, so here it is sufficient to point out that the odd isotopes are formed primarily via the r-process, while the even isotopes are formed via the s-process. Thus, determining the isotopic mixture which contributes the line profile is an indication of the processes that were in operation before the formation of HD 140283. Although previous authors indicate that the r-process is solely responsible for nucleosynthesis at early times, Magain finds for this example that the total solar system abundance provides the best fit to the line profile, and that there is no need to have an enhancement of the r-process at early times in Galactic history. Françios & Gacquer (1998) have repeated Magain's (1995) investigation with better quality spectroscopic data. They derive an isotopic mix for HD 140283 which is consistent with a purely r-process synthesis origin.

Françios (1996) combined the results of Françios et al. (1993) with an analyses of barium in a sample of metal-poor stars. The focus of the paper was to determine if in fact the scatter seen in the Gilroy et al. (1988) sample was intrinsic or observational in origin. Although the point is made that there is scatter in the [Ba/Fe] ratio at an [Fe/H]<-1.80, Françios believed that the dispersion was observational error, rather than an intrinsic scatter. The lack of intrinsic scatter negates the hypothesis of Truran (1981) that the r-process is solely responsible for the synthesis of n-capture elements early in the Galaxy's history. To explain this, Françios assigns an error of ±0.40 dex to the abundances determined for barium. As will be shown in the following chapters, these are rather over-conservative error bars, and with better quality data, the scatter can in fact be shown to be intrinsic.

Ryan, Norris & Beers (1996) analyzed 22 very metal-poor dwarfs and giants, all of which had [Fe/H] < -2.5, and 10 of which were below -3.0. Ryan et al. (1996)

find a spread in Sr abundances greater than a factor of 100. This, they say can in no way be attributed to observational error. Ryan et al. also find scatter in the results for the Ba abundances, which unlike the continuous, broad scatter found for the Sr result, appears to be bimodal. The majority of the trends are found for stars having [Ba/Fe] < 0, while there are a few stars lying well off the trend, with [Ba/Fe] > 0. This scatter provides further confirmation that the scatter seen in Gilroy et al. (1988) is real, rather than due to observational error. Another interesting result from Ryan et al. (1996) is the overabundance of the "light" n-capture elements (Sr-Y-Zr) with respect to the "heavy" n-capture elements (e.g., Ba). This may demonstrate the operation of the weak s-process early in the Galaxy, or it may point to another case of the as yet unexplained behavior of these elements, which will be addressed in Chapter III. Some of the more recent studies of the n-capture elements are included in the following chapters of this dissertation

E. The Big Picture

Understanding how, when, and where the r-process takes place sheds lights on many important issues. Detecting the r-process signature in metal-poor halo stars provides insight into the conditions that must have existed early in the Galaxy's history. The [Ba/Eu] ratio is a diagnostic of the extant conditions, since in solar system material Ba is primarily produced via the s-process, while Eu is produced via the r-process. However the [Ba/Eu] ratio is subsolar, which indicates that the halo must contain a larger fraction of r-process material than s-process material. Since the r-process must have specific astrophysical conditions (i.e., temperature, density) to operate in, certain types of objects must have existed which satisfied these conditions. These objects can be identified with certainty, once the site of the r-process is confirmed.

The 300-fold dispersion in the n-capture abundances in the metal-poor halo stars

shows that the Galactic material was not well mixed at the time of formation of these stars (McWilliam 1997 and references therein). This dispersion is also seen in abundances observed in halo planetary nebulae of low metallicity (Howard 1998). A search for the metallicity at which this dispersion disappears will help constrain the timescale for the homogenizing of the Galactic material and may indicate the time at which the SN I begin contributing iron to the ISM. Understanding the operation of the r-process and throughout the entire n-capture element mass range enables us to use nucleocosmochronology to determine the age of the Galaxy. Since the important nuclear chronometers uranium and thorium are formed exclusively via the r-process, it is crucial to confirm the operation of the r-process over the entire mass range. Then, when either U or Th are detected in stars, their abundances can be used to "date" the star, in much the same manner as radioactive carbon is used to date organic material. This was first suggested by Burbidge et al. (1957) and several attempts to use this method have been made, including results presented in this dissertation.

This dissertation contains recent observational studies on a large sample of metal-poor halo stars. It attempts to use the observed abundances of the n-capture elements to address the aforementioned issues: the astrophysical processes occuring during a star's evolution, the population of objects existing early in the Galaxy's history, the chemical evolution of the Galaxy, and the age of the Galaxy (and Universe). Chapter II contains the results of the study of a single, unusual star (CS 22892-052). Chapter III is the large sample survey of metal-poor Bond giants, looking at n-capture element transitions available to ground-based telescopes. Chapter IV includes both ground-based and Hubble Space Telescope (HST) data on three of these halo stars. Chapter V presents a summary of the results obtained and a discussion of their implications.

In Appendix I, a list of the isotopes used to generate the solar curves is presented along with the elemental abundances of the neutron-capture elements. Appendix II contains examples of syntheses for every star presented in Chapter III.
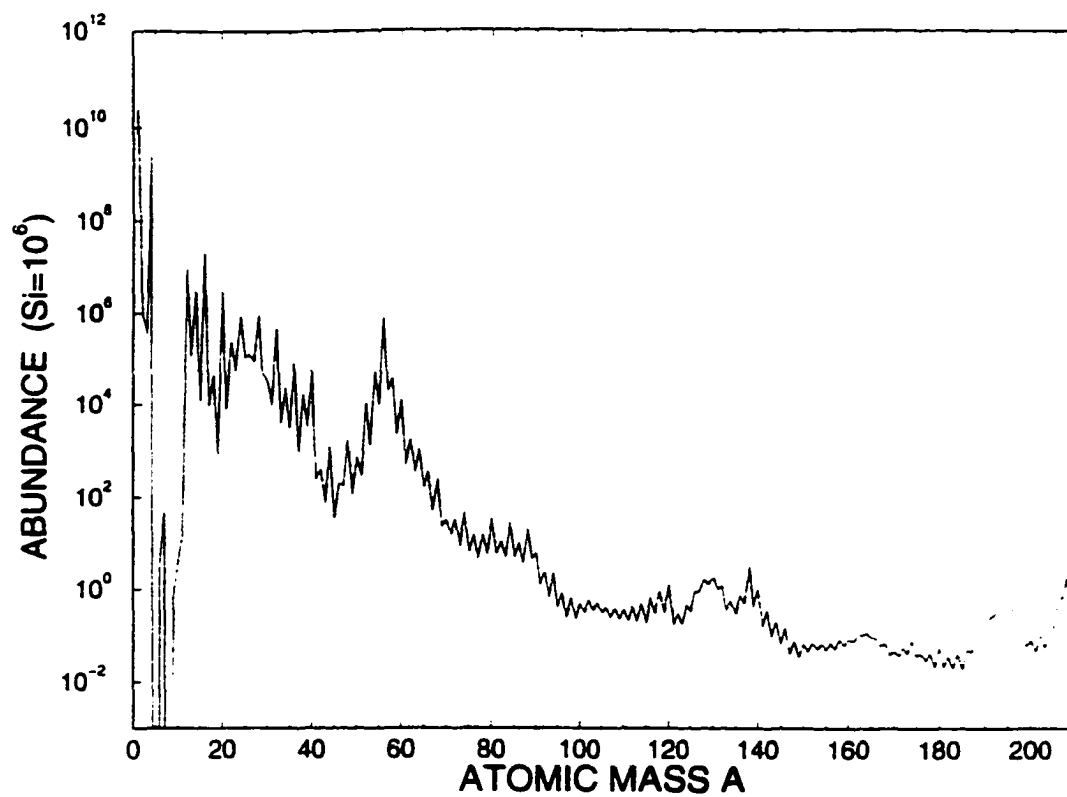
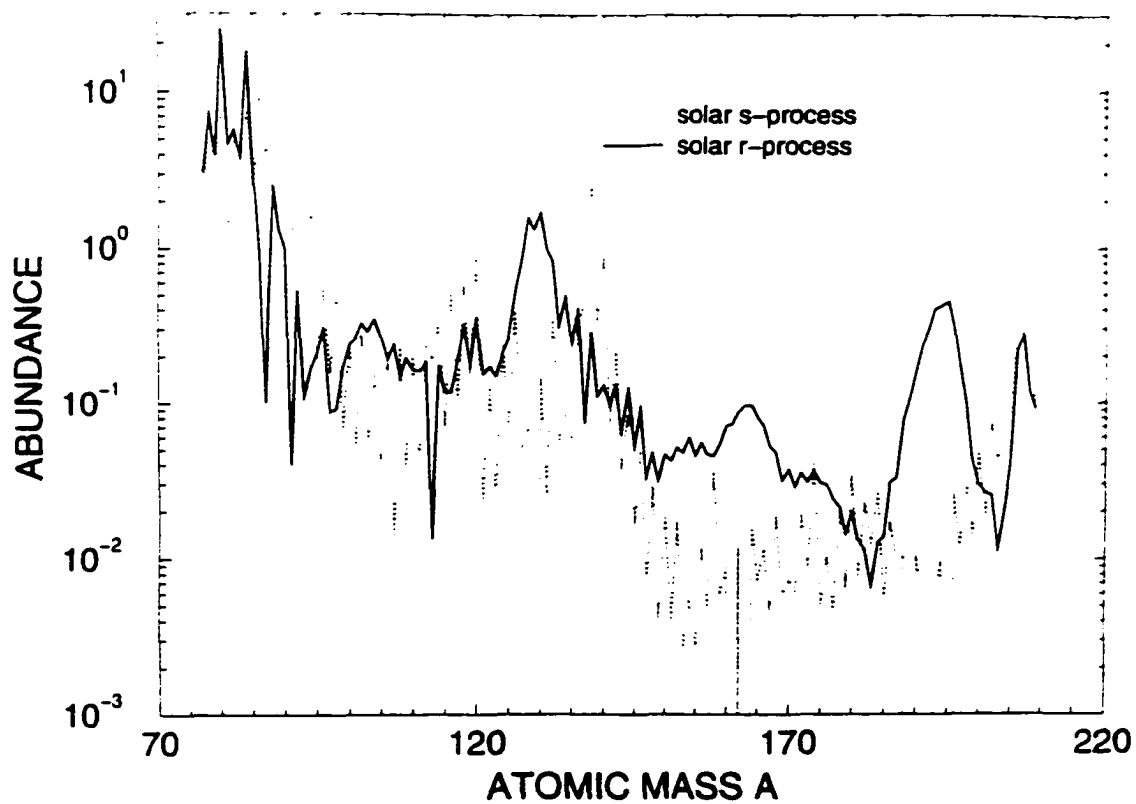Figure 1.1 Solar system elemental distribution from Anders & Grevesse (1989)

Figure 1.2 *s*-process and *r*-process fractional breakdown for *n*-capture elements from Käppeler et al. (1989)

Chapter II: CS22892-052:"Twinkle, Twinkle, Little Star ...."

A. Introduction

The K giant star CS22892-052 is ultra-metal-poor (([Fe/H])$\simeq$-3.1), but it has the largest abundance enhancements of neutron-capture elements yet discovered in any normal halo star (e.g.,[Eu/Fe] =1.7). Because of these conditions, the star presents an excellent spectrum for the study of n-capture elements. It has both low surface temperature and low gravity, which strengthens the many low-excitation singly ionized species transitions of these elements. This star was a Beers et al. (1992) survey star and is named for being the 52nd star on plate number 22892. The Beers survey consisted of 1044 extremely metal-poor stars primarily from the Southern Galactic Halo. The observations were done on the 61cm Curtis-Schimidt (CS) telescope at CTIO using the 4° HK Objective-Prism, with the H and K representing the H and K lines of CaII. The 289 plates were 5°x5°, and the long (90 min) exposure time allowed quite faint (B$\simeq$16.0) objects to be observed. The Beers survey was particularly important since it quadrupled the sample size of observed stars at [Fe/H]$\simeq$ -2.0.

CS22892-052 was chosen for analysis by Sneden et al. (1994, hereafter SPMS). Their observations were done at the Las Campanas 2.5m telescope with Schectman's Cassegrain echelle spectrograph, and the spectra had a signal-to-noise (S/N)$\simeq$35 and a resolution (R)$\simeq$22,000. Their analysis was done to determine abundances of 12 n-capture elements. The distinctive signature of the r-process was evident in the abundances of the second n-capture peak elements: [<Ba, La, Ce>/<Eu, Gd, Dy>]$\simeq$-0.6. The observational data for the star are contained in Table 2.1. If the age-metallicity relation is valid (i.e., low metallicity objects equals early history of

Galaxy), the Galaxy was quite young and likely not well mixed at the time of the formation of CS22892-052. The large overabundances of the heavy, neutron-rich elements are most likely explained as resulting from a single, local nucleosynthetic event, i.e., a supernova explosion near the formation site of CS22892-052

Cowan et al. (1995, hereafter CBSMP) took the abundances, except for Dy, of SPMS and attempted to fit the solar system r-process curve to these observed abundances. Such a fit would demonstrate that only the r-process had contributed to the abundances of these elements, which is to be expected at early times in the Galaxy's history if the site of the r-process comes from the Type II SNe. The Type II SNe are believed to come from the core-collapse of single massive stars. Such objects would have had sufficient time to have evolved and died before the formation of CS22892-052.

A new analysis, which included more spectral features, was performed to obtain a new Dy abundance. New laboratory studies on the Dy II line done by Grevesse, Noels, & Sauval (1993) and Biémont & Lowe (1993) provided updated values for the oscillator strengths. Five features (3996, 4050, 4073, 4103, 4449Å) were used in the analysis. Synthetic spectrum matches obtained from MOOG (Sneden 1973) to the CS22892-052 spectrum gave $<$[Dy/Fe]$> = +1.690\pm0.05$. This is in good agreement with the value of $+1.79$ from SPMS, but is a preferred value due to the larger number of features and the improved values of the laboratory oscillator strengths.

B. Observations

New high-resolution (R$\simeq$20,000), high signal-to-noise (S/N ranging from 30 to 130, dependent on wavelength) spectra of CS22892-052 were acquired with the Cerro Tololo Inter-American Observatory 4 m telescope and Cassegrain Echelle

24

Spectrograph during a four night run in 1994 by Chris Sneden. For three nights, spectra was gathered in the wavelength range $3600 \leq \lambda \leq 4700$ Å. On the last night, spectra were taken at the longer wavelength range: $4950 \leq \lambda \leq 8000$Å.

In order to achieve the high S/N of this faint cool star (V=13.18, B-V=0.78), multiple exposures were obtained, with a total of eight for the shorter wavelength spectra, and four for the longer wavelength spectra. Standard IRAF packages were used to reduce the spectra into FITS images for use in abundance analysis. The extreme deficiency of all elements with $Z \leq 30$ (except C) nearly erases all of the forest of lines that are found in the solar spectrum in this region. There is very little absorption in CS22892-052 except for a few strong Fe I and CH lines and the uncovered n-capture lines. We were able to measure many of the n-capture features' equivalent widths (EWs) since they were unblended in CS22892-052. This allowed the abundances to be determined directly from the EWs, rather than by spectral synthesis. These new spectra provided improved abundances for the 12 elements previously detected and provided data on several elements previously undetected.

C. Abundance Analysis

C.1 *The Model Atmosphere*

We adopted the model atmosphere derived by McWilliam et al. (1995). The adopted model atmosphere parameters are given in Table 2.2. We did not attempt to rederive model parameters from the Fe peak spectral features on our new spectra, treating these features only as contaminants to be considered in the abundance analysis. The lack of concern about the Fe peak is justified since almost all of the n-capture spectral features analyzed arise from low excitation potential ($\chi \simeq 1.0$eV) states of singly ionized species.

C.2 *Line Selection*

The spectral region $\lambda \leq 4700$ Å is rich in n-capture element lines. We selected appropriate transisitons for analysis in the following manner. For each n-capture element, we first predicted the approximate relative strengths for all lines that appear in the Kurucz (1995a,b) database for atomic and molecular transitions. For each line of interest, the relative strengths of neighboring n-capture transitions were also computed. We adopted the CS 22892-052 abundances of SPMS. For elements not considered in that paper, we assumed a solar r-process abundance distribution (Käppeler et al. 1989) scaled to the observed abundances. This allowed a preliminary culling of features that would be too weak for detection or too severely blended to isolate. We then consulted the solar spectrum line list of Moore, Minneart, & Houtgast (1966), discarding those n-capture lines that were like to be contaminated by strong residual Fe peak lines and by lines of CH.

We searched the literature for laboratory transition probabilities for the selected features. Fortunately, at least one lab transition probability study has been published within the last 20 years for each element of interest in our study. A full list of these studies can be found in Appendix A of Sneden et al. (1996). For species with more than five lines that are both accessible in the CS22892-052 spectrum and that have reliable lab transition probabilities, we eliminated lines that might be strong yet had no recent lab studies. For a few elements with not enough features meeting these criteria, we mixed lab transition probabilities with those of Kurucz (1995a,b).

The final list of lines chosen for the analysis of CS22892-052 is given in Table 2.3. It contains all elements that are "standard" in the past n-capture studies of metal-poor stars, and it has some transitions either rarely or never before used because of the near disappearance of many of the normal Fe peak blending transitions in CS22892-052.

C.3 General Abundance Results

We derived abundances for all selected n-capture features in CS22892-052 using single-line EW fits or synthetic spectrum analyses with the line lists previously described. The elemental abundances are listed in Table 2.3, with the mean abundances given in Table 2.4. A graphical representation of them is given in Figure 2.1. In Table 2.4, we quote standard deviations of the mean abundances and also the line-to-line scatters σ. We used the more conservative σ values in Figure 2.1 and in other figures to account for the uncertainties in the transition probability scales that we used. Our results are in good agreement with SPMS, but we have substantially added to the number lines employed for the elements considered and have detected six new elements with $Z \geq 64$.

C.4 Abundance Uncertainties

The uncertainties in the relative abundance results ratios from mainly (1) continuum placement errors in the spectrum, (2) uncertainties in the influence of blending by other transitions, and (3) scale and random uncertainties in laboratory transition probabilities. Uncertainties in the model atmosphere had little effect on the ratios. The abundance ratios among these elements are not significantly dependent on T_{eff} and the log g values. In our study, all species except Os I are first ions of atoms with relatively low ionization potentials (5.5 eV- 6.8 eV). Additionally, almost all of our lines arise from low excitation states (0.0-1.0 eV). And the majority of lines have EWs less than about 60 mÅ. For all of these reasons, most derived abundances have identical responses to changes in model atmosphere parameters. For changes of ± 75k in T_{eff}, $\pm$ in log g, and ± 0.1 in v_t, the following changes were produced in the [element/H] values: ± 0.06 ($\sigma = 0.02$) from changing T_{eff}, ± 0.07 ($\sigma = 0.02$) from changes in log g, and ∓ 0.02 ($\sigma = 0.02$) for changes in v_t.

The response of [Os/H] was ± 0.12, ∓ 0.01, and ∓ 0.01 for the same changes in

atmospheric parameters noted above. The strong lines of Sr II, Ba II and Eu II are much more sensitive to the microturbulent velocity parameter v_t. The average abundance changes from these lines is ∓ 0.1 for variations of ± 0.1.

D. Elements of Special Interest

Five elements (Tb, Ho, Tm, Hf, and Os) never before detected in low-metallicty stars were present in the spectra of CS22892-052. This brought the total of n-capture elements for which abundances could be determined to 20. This is the highest number of detections in any metal-poor star to date. However, there were a few potentially interesting elements which could not be detected in our study. The relevance of the thorium detection is discussed later in this chapter, while the importance of the Os detection is discussed at length in Chapter IV.

Holmium was detected for the first time in a metal-poor halo star. We attempted to observe the Ho II features included in Przybylski's (1963) analysis of HD 101065 (Przybylsk's Star) as well as features gleaned from standard lab references. All of the qualitatively strong features attributed to Ho II in HD 101065 that we didn't analyze in CS22892-052 proved to be too blended, of too high excitation, or too weak to be detectable in our spectra.

Terbium was detected for the first time in a cool star. In the solar spectrum, Tb II lines are quite weak, and available lines occur in the crowded spectral regions below 4500 Å. The derivation of Tb abundances for the Sun and stars is further complicated by the lack of extensive laboratory analyses. We hoped that the strength of the other n-capture features would extend to Tb as well and searched our spectrum for lines included in Biemont et al. (1981a,b). We detected seven Tb II transitions from their list. Three Ti features, as well as several other n-capture features, are located in the 3700-3900 Å region. This region is usually obscured by the strong CN band. Luckily, in spite of a high C abundance in CS22892-052, the

presence of CN is strong only near the band head, thus allowing analysis of the features within the band.

The barium abundance in the star is dependent on some assumptions. The Ba features in CS22892-052 are very strong, and therefore the abundance is sensitive to the microturbulent velocity. The two resonance lines at 4554Å and 4934Å also have hyperfine structure due to the odd-N isotopes Ba^{135} and Ba^{137}. Inclusion of hyperfine splitting was important to the analysis, since several of the n-capture transitions are heavily saturated in the spectrum. The abundance corrections due to hfs are always decreasing the previously calculated abundance. The even-N isotopes Ba^{134}, Ba^{136}, and Ba^{138} do not have hyperfine structure. In addition, the five Ba isotopes have very small isotopic wavelength offsets from each other. In order to obtain accurate abundances, spectrum syntheses must be used. In order to perform such syntheses, assumptions must be made about the isotopic abundance mixture. The Ba elemental abundance is significantly dependent on the chosen isotopic mix. Although Ba is primarily an s-process element, the s-process is not believed to be operating at the time of the formation of CS22892-052. Therefore the isotopic mix could be constrained to isotopes formed via the r-process. Ba^{134} and Ba^{136} have no r-process component. The most abundant Ba isotope, Ba^{138}, has a small r-process component, but is produced primarily in the s-process. The two odd isotopes, Ba^{135} and Ba^{137}, are the only ones with substantial r-process contributions. If only these two isotopes are used for the mixture contained in CS22892-052, the Ba/Eu conforms to the ratio predicted from the results of previous studies of n-capture elements in metal-poor stars. Also, the abundances of the other so-called s-process elements (i.e., La, Ce, and Pr) are depressed relative to the r-process elements (Eu, Gd, and Dy). These criteria led to choosing a final mixture that was a solar system r-process mixture with a microturbulent velocity of 2.3 km s^{-1}. This yielded a Ba abundance

of $<\log\epsilon>= -0.01\pm0.04$ ($\log \epsilon(M) \equiv \log_{10} (N_M/N_H) + 12.0$).

E. Fitting the Observed Abundances

Details of the calculation of the solar system elemental r-process and s-process curves are given in Appendix I. The solar system curves were compared to the observations of SPMS along with the new Dy abundance of CBSMP. Since CS22892-052 is very metal-poor with respect to the Sun, the solar system curves were shifted vertically downward (by a single scale factor) to compensate for the lower metallicity. The results of the comparison are shown in Figures 2.2 and 2.3, which plot the observed abundances compared to the scaled solar system r- and s-process curves, respectively, in spectroscopic units of $\log \epsilon$, versus atomic number, Z . The relative proportions of the elements Ba-Er correspond well with the solar system r-process distribution. For Figures 2.2 and 2.3, both the r- and s-process curves were arbitrarily fitted to the best average match to the observed abundances. After inspecting the figure, it is clear that the choice of normalization does not matter for the r-process curve. For the s-process curve, the distribution could be scaled vertically to try and improve the fit, but again inspection of the figure shows that the s-process can fit very few of the observed elements in CS22892-052.

While most of the elements from $Z=56$ to $Z=76$ are synthesized today by a combination of the r- and s-process, and some even are dominated by the s-process, osmium is formed almost entirely by the r-process and thorium is formed exclusively via the r-process. Thus, the detection of Os and Th in CS22892-052 is a confirmation that the entire r-process was in operation early in the history of the Galaxy in the progenitor(s) of this star. This result, coupled with the results to be presented in Chapter IV, strongly support the idea that very early in the history of the Galaxy, the r-process was responsible for the synthesis of heavy elements.

Sr, Y, and Zr were observed in CS22892-052, but no elements were observed

between Zr and Ba. Nevertheless, the r- and s-process curves were extended down to this lower mass region, in an attempt to fit these elements' abundances as well. Sr is the only element in CS22892-052 for which two ionization species can be obtained (SMPCBA). Two of the three detectable SrII (4077Å, 4215Å) lines in CS22892-052 are very strong and blended resonance lines. In addition, the SrI (4607Å) feature is very weak, so the Sr abundance from SMPCBA has a large uncertainty. While the Sr and Zr abundance seem to fit the solar system r-process abundances, the Y abundance is not successfully reproduced by this distribution. New laboratory studies have been performed by Wissack, Voss & Käppeler (1996) to more accurately determine the r- and s-process contributions to selected elemental abundances. In Table A.1 of Appendix 1, the numbers given in italics are Wissack et al's new calculations. If these numbers are used to generate the solar system curves, a better fit to the Sr abundance is obtained in the r-process curve, but Y is still not successfully reproduced (see Figure 2.4).

As mentioned in the introduction, the heavier nuclei in the main component of the s-process are believed to be produced in the low- and intermediate-mass red giants during the late stages of stellar evolution. The s-process isotopes up to mass $A \simeq 90$ are thought to be synthesized in the cores of massive stars ($M=10M_\odot$) near the end of the helium burning phase (Lamb et al. 1977; Prantzos, Hashimoto, & Nomoto 1990). This is referred to as the weak s-process, and provides a large contribution to the abundance of the Sr-Zr nuclei. The models of Raiteri et al. (1993), for the synthesis of the weak s-process nuclei in massive stars, were used to obtain an elemental curve for this component of the s-process. In an attempt to match the observations of Sr-Zr, we arbitrarily fitted this curve to the abundance of Y, as seen in figure 2.5 (Cowan et al. 1995). From inspection of the figure, it can be seen that the relative proportions of the abundances of Sr and Y can be matched

by the weak s-process. However, this model cannot match the abundance of Zr isotopes with mass numbers from 90-96. If the models of Käppeler, Beer, & Wisshak (1989) are employed, an even lower production of Zr is found. In an attempt to fit these three elements' abundances, an arbitrary mixture of weak s-process with an additional 50% contribution of r-process for Zr only was used. In concert with the solar system r-process for Ba-Er, a good fit to the observed abundances in CS22892-052 can be achieved. This, however, implies a very sharp and seemingly unphysical turnoff/turnon of the the weak s-process/r-process near mass number 90.

F. In Theory

As we have seen in the previous section, the observed abundances for the n-capture elements in CS22892-052 can be successfully matched up to the scaled solar system r-process abundance curve determined from solar system abundances. The next step is to fit these observed abundances with theoretical models, such as the dynamic r-process code of Cowan (Cowan et al. 1991, Cowan et al. 1997). The dynamic r-process model calculates the production of these n-capture elements due to certain conditions (e.g. neutron number density) independent of astrophysical site. These calculations do not assume any equilibrium conditions. Instead, it determines abundances under conditions of rapidly falling temperature, density, and neutron number density, where equilibrium assumptions aren't valid.

The first theoretical fit is based upon the work of Cowan et al. 1991 (hereafter designated as theory-1). This model attempts to reproduce the solar system r-process abundances by mass number by supposing that the site of the r- process is a helium-driven supernova shock. One problem with this proposed site is that it requires excessive mixing of hydrogen into the helium zone of the presupernova star. However, this model still achieves a reasonably good fit to the solar r-process abundance, which demonstrates that although the site may be incorrect, the

32

conditions employed are suitable to reproduce the r-process signature. Therefore, this theoretical model can be used to study r-process nucleosynthesis independent of knowing the actual site.

A full discussion of the nuclear data sets used for this model can be found in Cowan et al. (1991). The parameters used in the calculations include a postshock peak temperature of $T = 4x10^8$K and a density of $\rho = 10^4$g cm^{-3}, giving a number density of 10^{20} neutrons per second. The comparison of the calculated Theory 1 abundances to the observed abundances in CS22892-052 is shown in Figure 2.6. Again, this theory curve has been vertically shifted to compensate for the metallicity of CS22892-052.

Note that at Z = 56-67 there is good agreement between the theoretical and observed abundances, but at higher values, there are deviations. At the location of the largest deviations (Z≃80) there are no available observations as can be seen in the plot of the theoretical curve to the observed abundances in Figure 2.7. The deviations in Theory-1 may be due to using too low a neutron density.

Theory 2 used the same input nuclear data and code used for Theory 1. However, the neutron density was set to a higher value of 10^{21} for a duration time of 1 second. After 1 second the neutron flux was stopped and let decrease until freeze-out of neutron reactions. The additional neutron captures and beta decays were followed for a time of 2000 seconds. Again, this model is only mimicing conditions required to achieve the r-process signature, not suggesting a site for these conditions. The comparison of the calculated Theory-2 abundances are given in Figures 2.8 and 2.9. The abundances calculated from this model give a better fit to the elements Z = 67-76.

G. Thorium Ages From Radioactive Decay

The detection of n-capture elements in the heaviest solar system (osmium-platinum) r-process peak near mass number 200 is particularly important (SMPCBA, Cowan et al. 1996, Chapter IV). These observations strengthen the belief that the production of the elements found in these halo stars occurred in relative solar system proportions, and also confirms the operation of the r-process for the synthesis of the heaviest ($Z \geq 55$) r-process elements during the early history of the Galaxy (Cowan et al. 1996). This last point is particularly important since the important nuclear chronometers U and Th are formed exclusively by the r-process (Cowan et al. 1991). These nuclei are useful as chronometers since they have extremely long half-lives ($\simeq 10^9$ years). In the CTIO observations of SMPCBA, the element Thorium was detected. Th^{232}, which decays to Pb eventually, has a half-life of 14 billion years which makes it an excellent choice for a chronometer, since its decay time is on the order of the age of the Universe.

Figure 2.10 shows the scaled solar system r-process curve extrapolated (*dashed line*) to the thorium region, with the Th abundance being calculated for the time of formation (Anders & Grevesse 1989). From inspecting the figure, it is clear that the Th abundance in CS22892-052 is well below the solar formation value. If instead, the current value of the solar system Th abundance is used, it is still obvious that the value of Th in this star is still well below the curve (Figure 2.11). This indicates that this halo star's age is much older that the Sun's current age. If an attempt is made to force the current solar value curve to fit the abundance of Thorium, it becomes clear that none of the other elements are adequately fit by the new scaling of the curve. This confirms the conclusions of SMPCBA that the stable data fit the solar system r-process curve and that the abundance of Th in this star is significantly subsolar.

The abundance of Th can be used to find an age estimate for CS22892-052 by using a simple radioactive decay model. To calculate the age, the simple radioactive decay equation was used, along with the known half-life of Th (14.05 Gyr):

$$N_{Th}(t) = N_{Th}(t_o)\exp(-t/\tau_{Th}),$$

where

$$\tau_{Th} = (14.05/ln2)\text{Gyr}=20.27 \text{ Gyr}$$

Since it is independent of any specific chemical evolution model, this simple model actually provides the lowest age estimate for this star, with an age of 15.2±3.7Gyr. If any production of Th in this star is considered, the star must be even older. The uncertainty in the age is due primarily to the uncertainty of the Th abundance.

H. Other Dating Methods

The theoretical models of Cowan et al. (1991) described in section E. can be used to determine Th abundances from the fit of the r-process curve. These abundances can be used to determine an age for CS22892-052. Theory-1 predicts a Th abundance that is almost identical to the Th abundance at the time of the formation of the Galaxy, 4.6 Gyr ago. This model gives Th/Eu=0.470, which corresponds to an age of 15.9± ≃2.0. Theory-2 gives a ratio of Th/Eu=0.427 and an age of 13.5± ≃2.0. Both of these models give ages which agree with the simple model described in Section D.

The chemical evolution models of Andrew McWilliam (Cowan et al. (1997)) considered both on-going nucleosynthetic activity and a multiple burst scenario as opposed to the single burst scenario consider in the previous models. To make use of these models, an age for the Galactic disk must be adopted. Cowan et al. (1997) choose 10.5 Gyr as the disk age. Use of these models actually increases the age of CS22892-052. If one considers on-going nucleosynthesis, the age of CS22892-052 must be extremely large, since the Th abundance in the interstellar medium

would be increasing constantly due to constant production from the r-process site. Similarly, the multiple burst model has the Th abundance increased by the bursts of nucleosynthetic activity. In either case, the Th would have to have been decaying for even longer times to account for the observed abundance in CS22892-052. The age obtained for the various chemical evolution models is 17 ± 4 Gyr. These models are dependent on a number of assumptions, including the collapse time for the disk and the consideration of infall and outflow.

I. Conclusions

We have employed high-S/N, high-resolution spectra to derive abundances for 20 n-capture elements in CS22892-052. Highlighting our abundances are the detection of five elements never before observed in very metal poor stars, including the element osmium of the third r-process peak and the actinide chronometer thorium. The huge overabundances of the n-capture elements in this star compared to the Sun seem to indicate that the time scale for the formation of CS22892-052 was shorter than the timescale for the mixing of Galactic material. Evidently this star formed quite near a region of nucleosynthetic activity, whatever the source of that activity may have been.

Also, the abundance of these elements seem to confirm the operation of the r-process over the entire mass range for these elements. Although part of the detected elements (e.g. Ba) are formed primarily in the s-process in the solar system, at early times in the Galaxy they seem to be formed via the r-process. This discovery is useful in determining what sort of objects may have lived and died before the formation of CS22892-052, and thus help nail down the site of r-process nucleosynthesis.

The detection of the radioactive element Th provides an opportunity to estimate the age of this star, and make useful predictions about the age of the Galaxy by

various methods, including a simple radioactive-decay model. The predicted ages can then be used to put a lower limit on the age of the Universe. These ages are in good agreement with ages predicted independently by globular clusters (Pont et al. 1998) and Type Ia SNe (Branch et al. 1996, Riess et al. 1998).

TABLE 2.1. Observational Parameters of CS22892-052

Quantity	Value
R.A.(1950)	$22^h 14^m 18^s9$
Decl.(1950)	$-16°54'26''$
V	13.18
B-V	0.78
U-B	0.14
V-R	0.48
E(B-V)	0.02
M_v	-0.23
Distance(pc)	4700

TABLE 2.2. Model Atmosphere for CS22892-052

Quantity	Value
$T_{eff}(K)$......................	4725
$\log g$......................	1.00
$[M/H]$...........................	-3.00
$v_t(km\ s^{-1})$...............	2.00

TABLE 2.3. Line Data

λ Å	x eV	log(gf)	Ref.	EW mÅ	log ε
Sr I, Z=38					
4607.34	0.00	+0.28	1	syn	+0.5:
Sr II, Z=38					
4077.71	0.00	+0.17	1	syn	+0.50
4161.82	2.94	−0.60	1	syn	+0.80
4215.52	0.00	−0.17	1	syn	+0.30
Y II, Z=39					
3774.90	0.13	+0.21	2	87.0	−0.41
3788.70	0.10	−0.07	2	75.0	−0.48
3818.34	0.13	−0.98	2	38.0	−0.29
3950.36	0.10	−0.49	2	64.0	−0.38
4398.01	0.13	−1.00	2	51.0	−0.19
4883.69	1.08	+0.07	2	46.0	−0.27
5087.43	1.08	−0.17	2	19.0	−0.59
5123.22	0.32	−0.93	2	syn	−0.45
5200.42	0.99	−0.57	2	13.0	−0.51
5205.73	1.03	−0.34	2	21.0	−0.44
Zr II, Z=40					
3836.77	0.56	−0.06	3	65.0	+0.29
4161.21	0.71	−0.72	3	33.0	+0.43
4208.99	0.71	−0.46	3	37.0	+0.24
4317.32	0.71	−1.38	3	10.5	+0.45
4496.97	0.71	−0.59	3	26.5	+0.11
Ba II, Z=56					
3891.78	2.51	+0.28	4	syn	−0.2:
4130.65	2.72	+0.56	4	syn	+0.05
4554.03	0.00	+0.17	4	177.0	+0.13
4934.10	0.00	−0.15	4	180.0	+0.10
5853.69	0.60	−1.01	4	72.0	−0.06
6141.73	0.70	−0.07	4	119.0	−0.09
6496.91	0.60	−0.38	4	117.0	−0.02
La II, Z=57					
3988.52	0.40	+0.08	1	51.0	−0.75
3995.75	0.17	−0.02	1	syn	−0.90
4086.71	0.00	−0.16	1	syn	−0.85
4123.23	0.32	+0.12	1	syn	−0.95
4333.76	0.17	−0.16	1	syn	−0.80
5123.01	0.32	−0.05	1	syn	−0.70
6320.43	0.17	−1.52	1	6.5	−0.71
Ce II, Z=58					
4073.47	0.48	+0.32	5	15.5	−0.74
4083.23	0.70	+0.24	5	15.0	−0.41
4120.84	0.32	−0.24	5	syn	−0.15
4127.38	0.68	+0.24	5	16.0	−0.41
4222.60	0.12	−0.18	1	24.0	−0.47
4418.79	0.86	+0.31	5	10.0	−0.55
4486.91	0.30	−0.36	1	10.0	−0.57
4562.37	0.48	+0.33	1	25.0	−0.58
4628.16	0.52	+0.26	1	23.0	−0.52
Pr II, Z=59					
3964.26	0.22	−0.40	6	syn	−0.90
3964.81	0.05	+0.09	7	syn	−1.20
3965.26	0.20	−0.13	7	syn	−1.05
4062.80	0.42	+0.33	8	26.5	−0.84
5220.12	0.80	+0.17	7	9.0	−0.96
5259.74	0.63	−0.07	7	7.5	−1.02

TABLE 2.3 (continued)

λ Å	χ eV	log(gf)	Ref.	EW mÅ	log ε
		Nd II, Z=60			
3973.27	0.63	+0.43	9	35.0	−0.44
4018.81	0.06	−0.88	10	16.5	−0.27
4021.34	0.32	−0.17	11	25.0	−0.44
4061.09	0.47	+0.30	9	53.0	−0.20
4069.27	0.06	−0.40	11	27.0	−0.49
4109.46	0.32	+0.18	9	64.0	−0.07
4232.38	0.06	−0.35	11	27.0	−0.57
4446.39	0.20	−0.63	10	26.5	−0.18
4462.99	0.56	−0.07	9	32.0	−0.19
5130.59	1.30	+0.10	9	7.0	−0.34
5212.35	0.20	−0.70	11	13.0	−0.59
5234.21	0.55	−0.46	10	9.5	−0.56
5249.60	0.98	+0.08	12	13.5	−0.41
5293.17	0.82	−0.20	12	13.5	−0.33
5311.48	0.99	−0.56	12	4.5	−0.28
5319.82	0.55	−0.35	12	21.5	−0.27
5361.51	0.68	−0.40	11	12.5	−0.34
5442.29	0.68	−0.90	11	5.8	−0.21
		Sm II, Z=62			
3793.97	0.10	−0.50	13	17.0	−0.74
3896.97	0.04	−0.58	13	17.5	−0.74
4023.23	0.04	−0.83	13	18.0	−0.51
4068.32	0.43	−0.71	13	14.0	−0.29
4318.94	0.28	−0.27	13	28.0	−0.59
4499.47	0.25	−1.01	13	6.0	−0.69
4519.63	0.54	−0.43	13	10.5	−0.66
4537.95	0.48	−0.23	13	13.0	−0.84
4577.69	0.25	−0.77	13	12.5	−0.60
		Eu II, Z=63			
3724.95	0.00	−0.076	14	syn	−0.90
3930.51	0.21	+0.190	14	syn	−0.90
3971.96	0.21	+0.279	14	syn	−1.00
4129.70	0.00	+0.204	14	syn	−0.80
4205.05	0.00	+0.117	14	syn	−0.80
4435.56	0.21	−0.090	14	syn	−0.94
4522.57	0.21	−0.678	14	syn	−0.9:
6437.64	1.32	−0.276	14	9.0	−0.67
6645.13	1.38	+0.204	14	9.5	−1.06
		Gd II, Z=64			
3768.40	0.08	+0.250	15	50.0	−0.63
3796.39	0.03	+0.030	16	53.0	−0.41
3844.58	0.14	−0.510	15	20.0	−0.44
3916.51	0.60	+0.060	15	17.5	−0.55
4037.91	0.73	+0.070	16	11.5	−0.64
4085.57	0.56	−0.230	16	10.0	−0.62
4191.08	0.43	−0.680	15	13.5	−0.21
		Tb II, Z=65			
3658.89	0.13	+0.370	17	syn	−1.4:
3702.86	0.13	+0.050	17	syn	−1.00
3848.74	0.00	+0.060	17	syn	−1.15
3874.17	0.00	+0.280	17	syn	−1.2:
3899.20	0.37	+0.000	17	syn	−1.15
4002.57	0.64	+0.130	17	syn	−1.10
4005.47	0.13	+0.250	17	syn	−1.70

TABLE 2.3 (continue

λ Å	χ eV	log(gf)	Ref.	ε mÅ	log ϵ
Dy II, Z=66
3869.86	0.00	-0.940	18	23.0	-0.34
3996.69	0.59	-0.190	18	30.0	-0.26
4011.30	0.93	-0.630	18	4.0	-0.43
4042.05	0.93	-0.700	18	4.5	-0.31
4103.31	0.10	-0.370	18	58.0	-0.17
4468.14	0.10	-1.500	18	5.5	-0.49
5169.69	0.10	-1.660	18	3.5	-0.63
Ho II, Z=67
3796.75	0.00	+0.200	19	syn	-0.8:
3810.74	0.00	+0.140	19	syn	-0.95
4045.47	0.00	-0.180	19	syn	-0.90
4152.58	0.08	-0.890	19	syn	-1.0:
Er II, Z=68
3692.65	0.05	+0.130	20	syn	-0.6:
3786.84	0.00	-0.640	20	syn	-0.40
3830.48	0.00	-0.360	20	syn	-0.45
3896.23	0.05	-0.240	21	syn	-0.55
3938.63	0.00	-0.520	6	39.0	-0.58
Tm II, Z=69
3700.26	0.03	-0.290	6	syn	-1.25
3761.33	0.00	-0.250	6	syn	-1.30
3795.76	0.03	-0.170	6	syn	-1.40
3848.02	0.00	-0.130	6	syn	-1.50
Yb II, Z=70
3694.19	0.00	-0.230	22	syn	-0.80
Hf II, Z=72
3719.28	0.61	-0.870	22	syn	-0.8:
3793.38	0.38	-0.950	6	syn	-1.0:
Os I, Z=76
4135.77	0.52	-1.260	6	syn	+0.25:
4261.85	0.00	-1.440	6	syn	-0.50
4420.47	0.00	-1.530	23	syn	-0.05
Th II, Z=90
4019.12	0.00	-0.270	24	syn	-1.55

References:
(1) Gratton & Sneden (1994)
(2) Hannaford et al. (1982)
(3) Biémont et al. (1981)
(4) Gallagher (1967)
(5) KUR95, modified
(6) KUR95
(7) Goly et al. (1991)
(8) Goly et al.(1991), Lage & Whaling (1976)
(9) Maier & Whaling (1977)
(10) Ward et al. (1984,1985), modified
(11) Corliss & Bozman (1962), modified
(12) Maier & Whaling (1977), Ward et al. (1984,1985)
(13) Biémont et al. (1989)
(14) Biémont et al. (1982)
(15) Corliss & Bozman (1962)
(16) Bergström et al. (1988)
(17) Biémont et al. (1981b), Gorshkov et al.(1982)
(18) Kuss (1992), Biémont & Lowe (1993)
(19) Gorshkov & Komarovskii (1979)
(20) Musiol & Labuz (1983)
(21) Biémont & Youssef (1984)
(22) Andersen et al. (1975)
(23) Kwiatkowski et al. (1984)
(24) Lawler et al.(1990)

TABLE 2.4 Elemental Abundances

Species	Z	log ϵ ⊙	log ϵ CS 22892-052	σ^1	No. lines	[M/H]
Sr I,II	38	2.90	$+0.50 \pm 0.12$	0.25	4	−2.40
Y II	39	2.24	-0.40 ± 0.04	0.12	10	−2.65
Zr II	40	2.60	$+0.30 \pm 0.06$	0.14	5	−2.30
Ba II	56	2.13	-0.01 ± 0.04	0.11	7	−2.19
La II	57	1.22	-0.81 ± 0.04	0.10	7	−2.01
Ce II	58	1.55	-0.49 ± 0.05	0.16	9	−2.05
Pr II	59	0.71	-1.00 ± 0.05	0.13	6	−1.71
Nd II	60	1.50	-0.34 ± 0.04	0.15	18	−1.83
Sm II	62	1.00	-0.63 ± 0.05	0.16	9	−1.63
Eu II	63	0.51	-0.89 ± 0.04	0.12	9	−1.40
Gd II	64	1.12	-0.50 ± 0.06	0.16	7	−1.62
Tb II	65	0.33	-1.24 ± 0.09	0.24	7	−1.45
Dy II	66	1.10	-0.38 ± 0.06	0.15	7	−1.30
Ho II	67	0.50	-0.91 ± 0.05	0.09	4	−1.41
Er II	68	0.93	-0.52 ± 0.04	0.09	5	−1.45
Tm II	69	0.13	-1.36 ± 0.06	0.11	4	−1.49
Yb II	70	1.08	-0.80 ± 0.00	––	1	−1.88
Hf II	72	0.88	-0.90 ± 0.10	0.14	2	−1.78
Os I	76	1.45	-0.10 ± 0.22	0.38	3	−1.55
Th II	90	0.12	-1.55 ± 0.00	––	1	−1.67

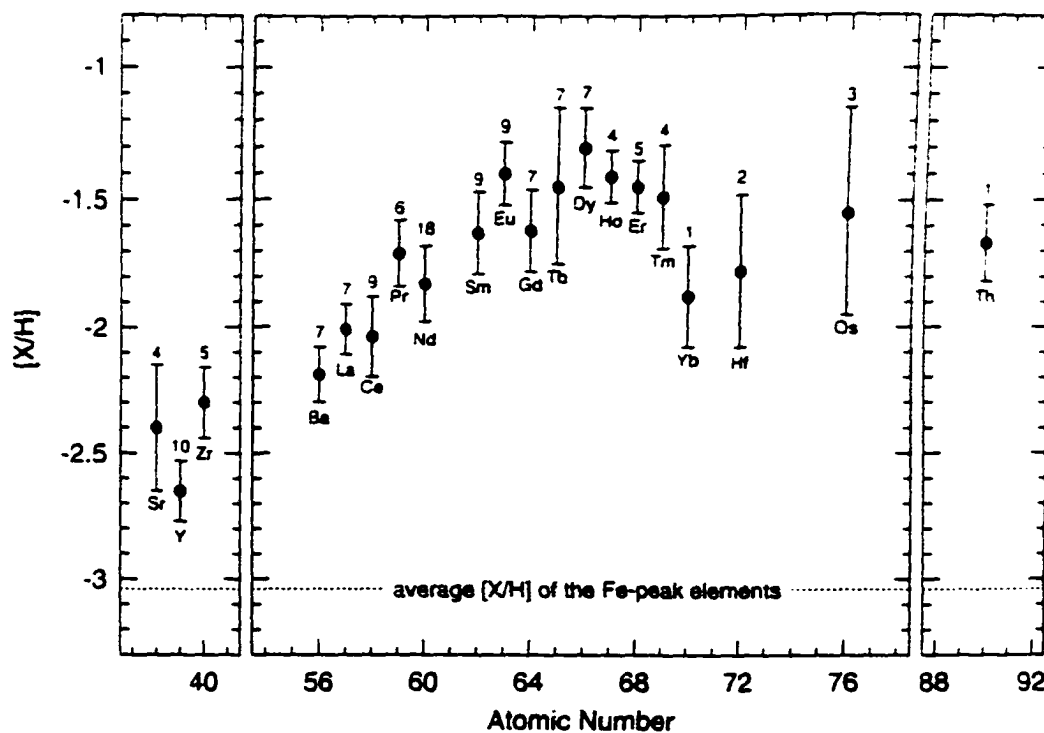Notes: (1) $\sigma \equiv$ the line-to-line scatter of an abundance.

Figure 2.1 Abundances of n-capture elements in CS22892-052. In order to emphasize the very large overabundances of all n-capture elements, for this figure only the abundances are given in the "bracket notations, that is, differentially with respect to solar abundances. The dashed horizontal line at [X/H] = -3.05 represents that average abundance level of the Fe-peak elements Sc, Cr, Mn, Fe, Co, and Ni in CS22892-052 (McWilliam et al. 1995b). For each element the atomic symbol is given below the point and the number of lines used for the abundance is given above the point. The error bars shown here are the σ (standard deviation of the sample) values.
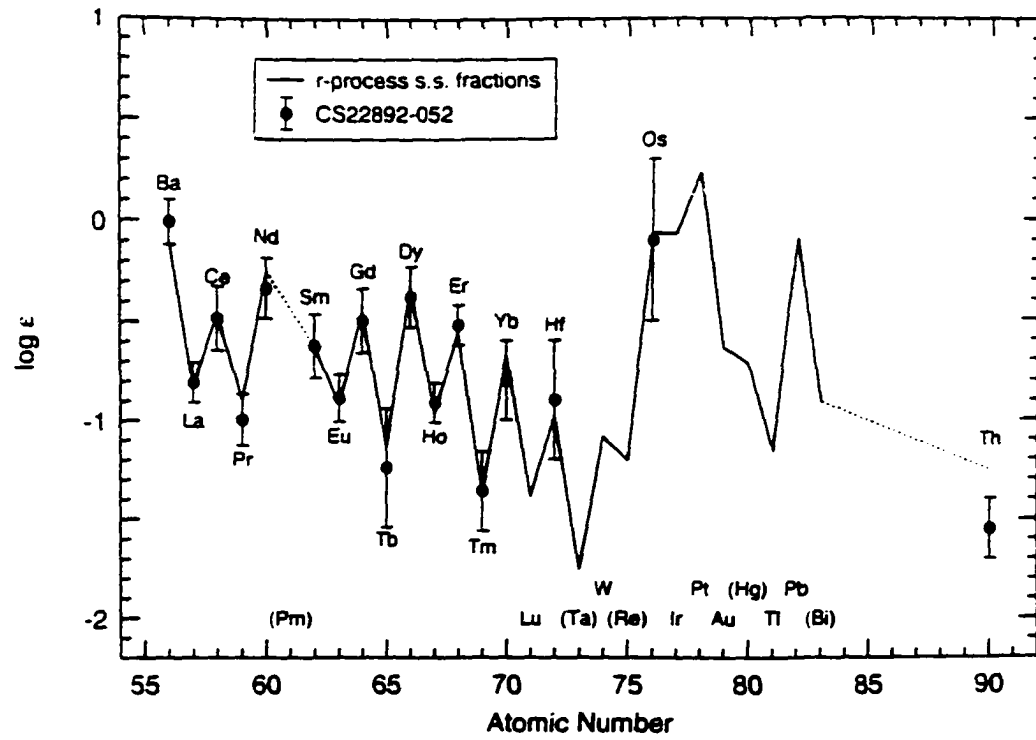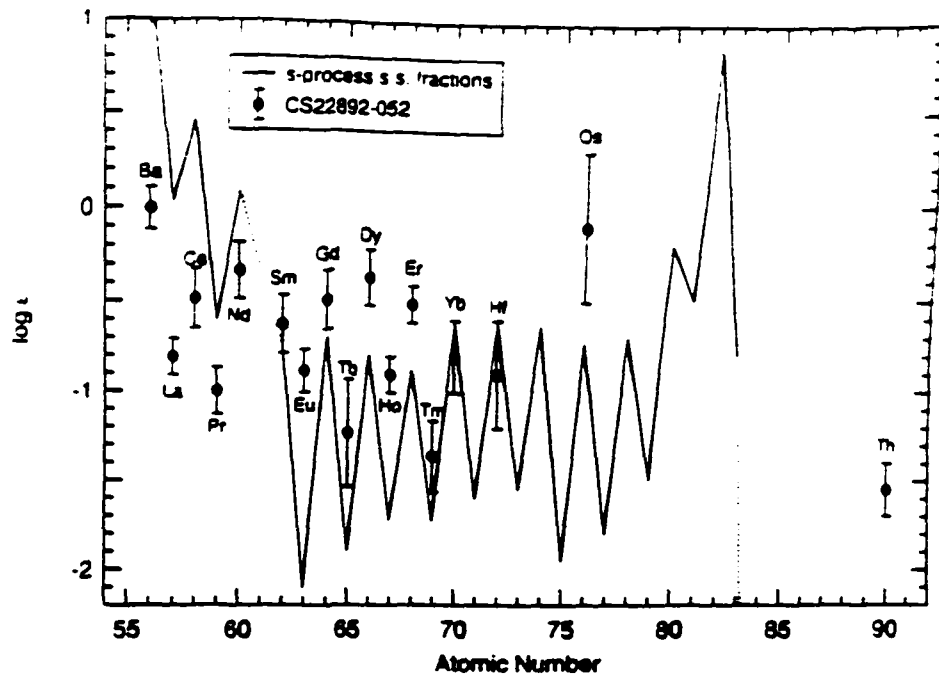
Figure 2.2 Mean abundances in CS22892-052 compared with a scaled set of solar system r-process abundance fractions. Error bars are σ values. The atomic symbols of elements are written near each observed point, or at the bottom of the graph for elements unobserved in CS22892-052. Parentheses surround the symbols of those elements that are totally unstable (Pm), or are unobserved in the Sun (Ta, Re, Hg, Bi). The vertical scaling applied to the solar abundance distribution is that which provided the best average match to the observed abundances in the $56 \leq Z \leq 76$ element range.

Figure 2.3 Mean abundances in CS22892-052 compared with a scaled set of solar system s-process abundance fractions. The symbols are as in Figure 2.2. The vertical scaling of the solar abundance distribution is approximate, and is meant for display purposes only.
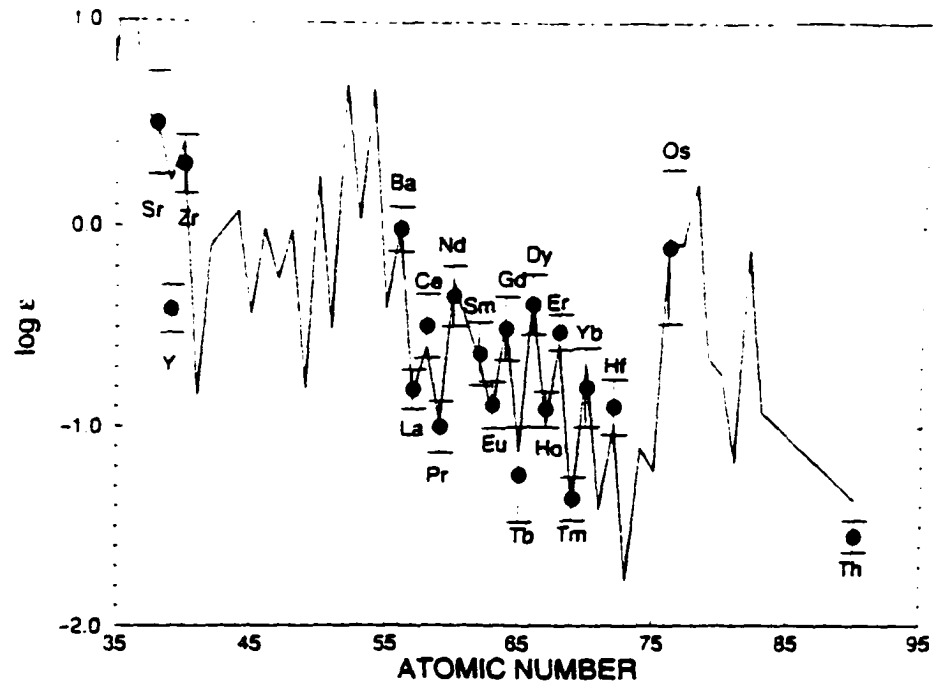
Figure 2.4 Attempt to duplicate the observed abundances in CS22892-052 of lighter
n-capture elements by fitting the scaled *r*-process distribution as recalculated in Wisshack
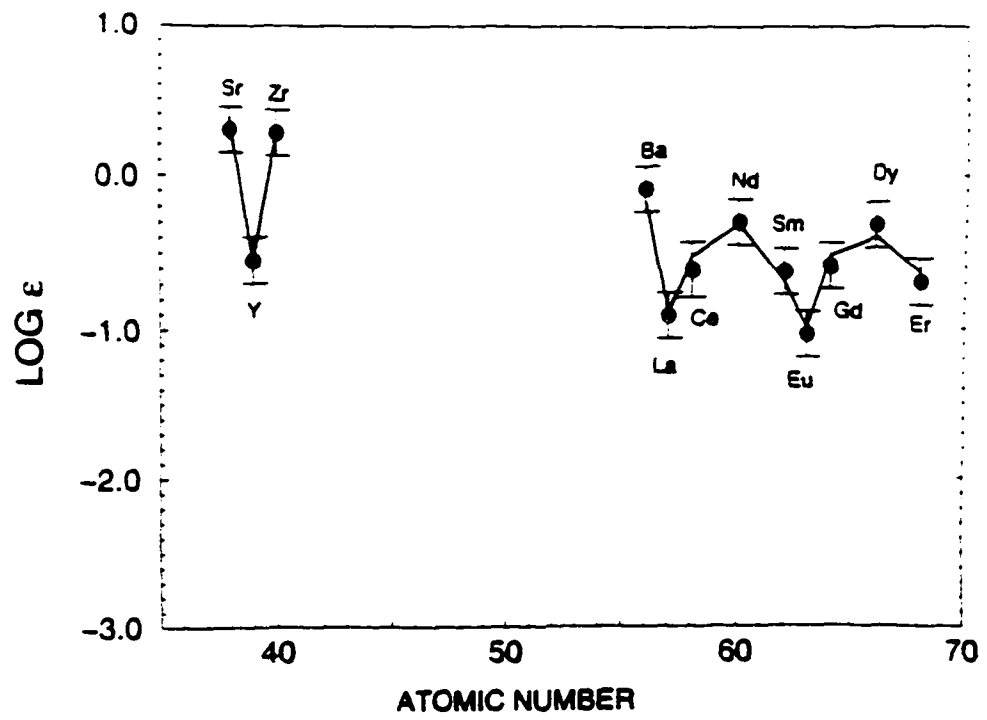et al. (1996).

Figure 2.5 Attempt to duplicate the observed abundances in CS22892-052 of lighter n-capture elements by fitting an admixture of the r-process and the weak s-process to Sr-Y-Zr.

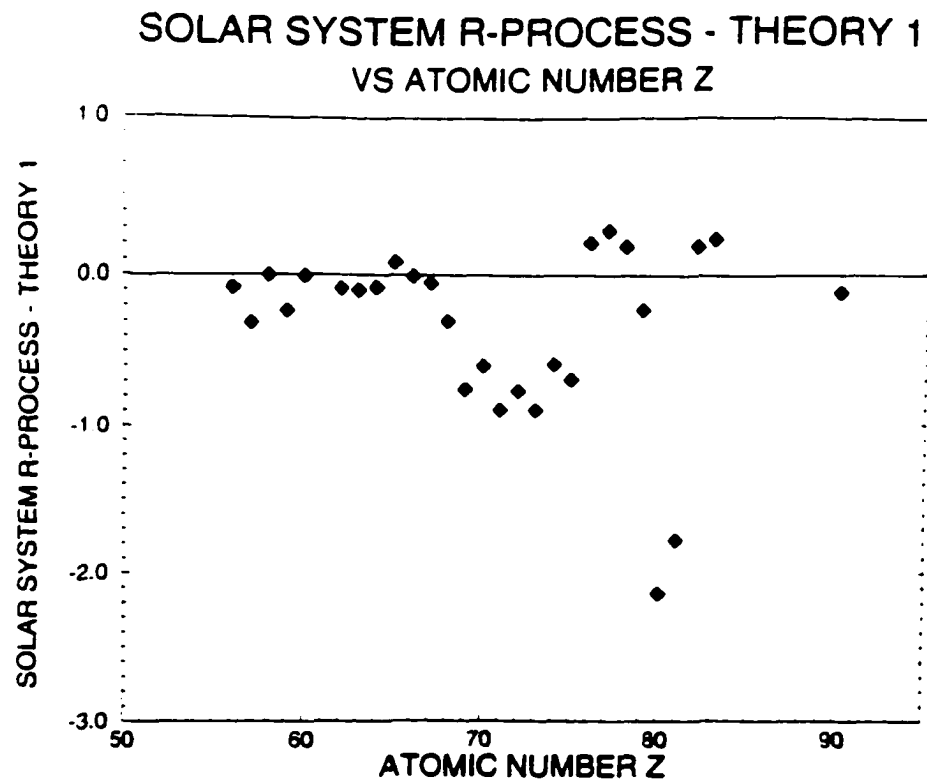**SOLAR SYSTEM R-PROCESS - THEORY 1**
VS ATOMIC NUMBER Z

Figure 2.6 Differential comparisons by element of the abundance determinations from the solar system r-process curve (Figure 2.2) and from theory-1 (Cowan et al. 1991).
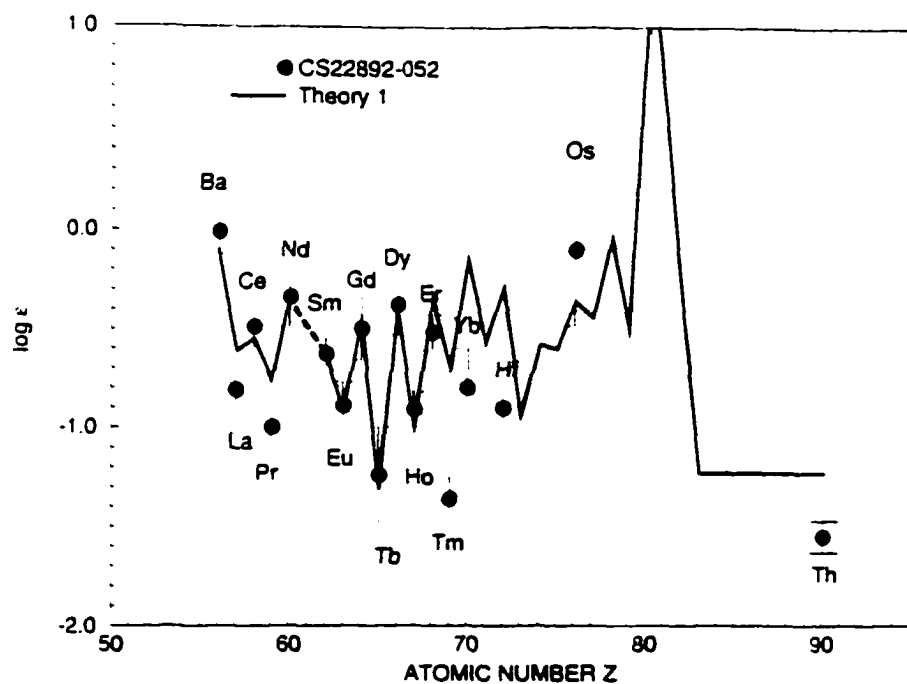
Figure 2.7 Comparison of observed abundances from CS22892-052 with elemental abundances calculated in theory-1. Error bars are as in Figure 2.1.
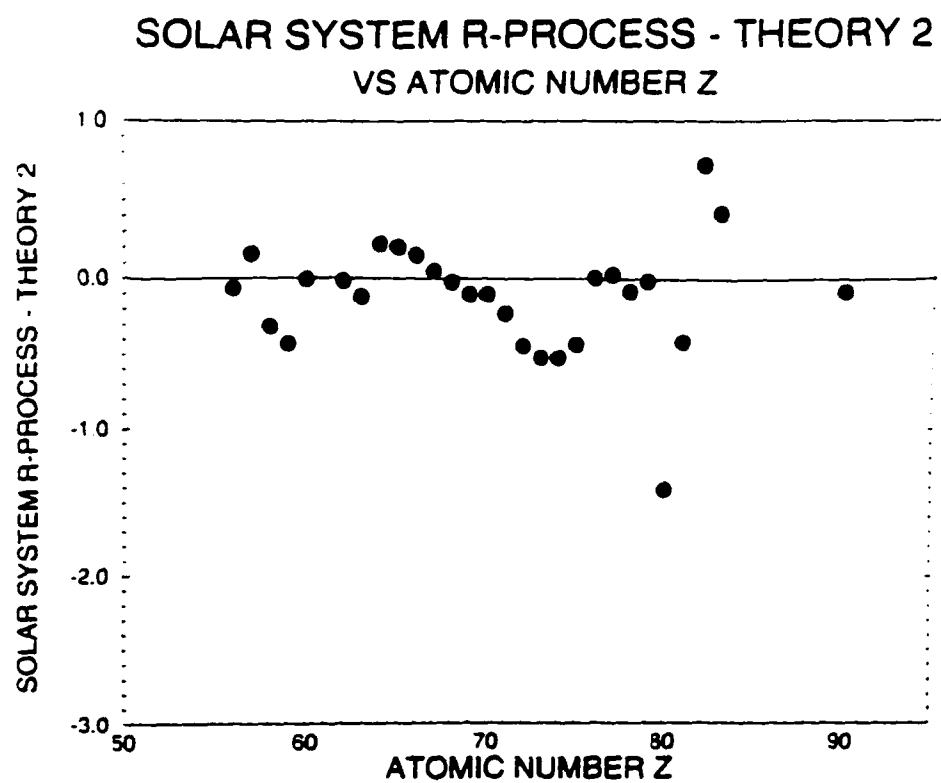
Figure 2.8 Differential comparisons by element of the abundance determinations from the solar system r-process curve (Figure 2.2) and from theory-2.
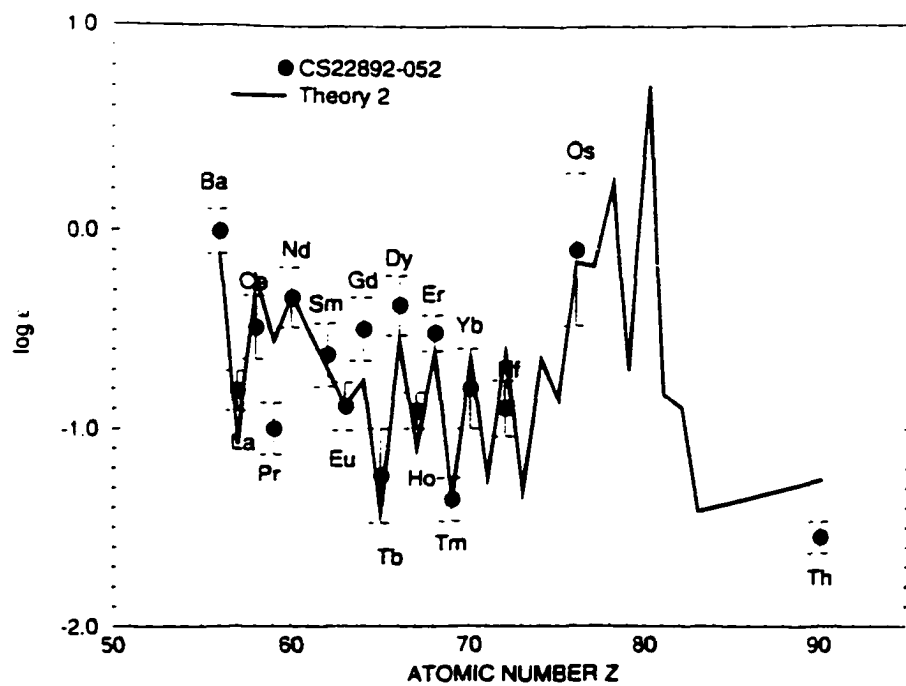
Figure 2.9 Comparison of observed abundances from CS22892-052 with elemental abundances calculated in theory-2. Error bars are as in Figure 2.1.
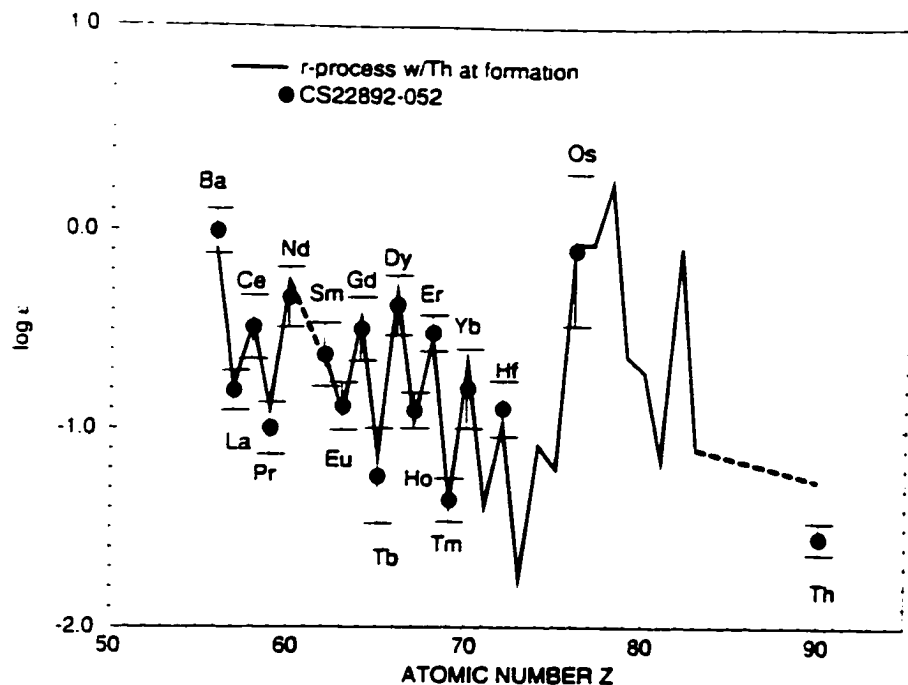
Figure 2.10 Comparison of observed abundances from CS22892-052 with a solar r-process elemental abundance curve with the thorium abundance at the time of solar system formation. The error bars are as in Figure 2.1 with the exception of Th, which has error bars based upon an analysis of the individual errors in lab transition probability, the continuum placement, and possible line contamination, as described in Sneden et al. (1996)
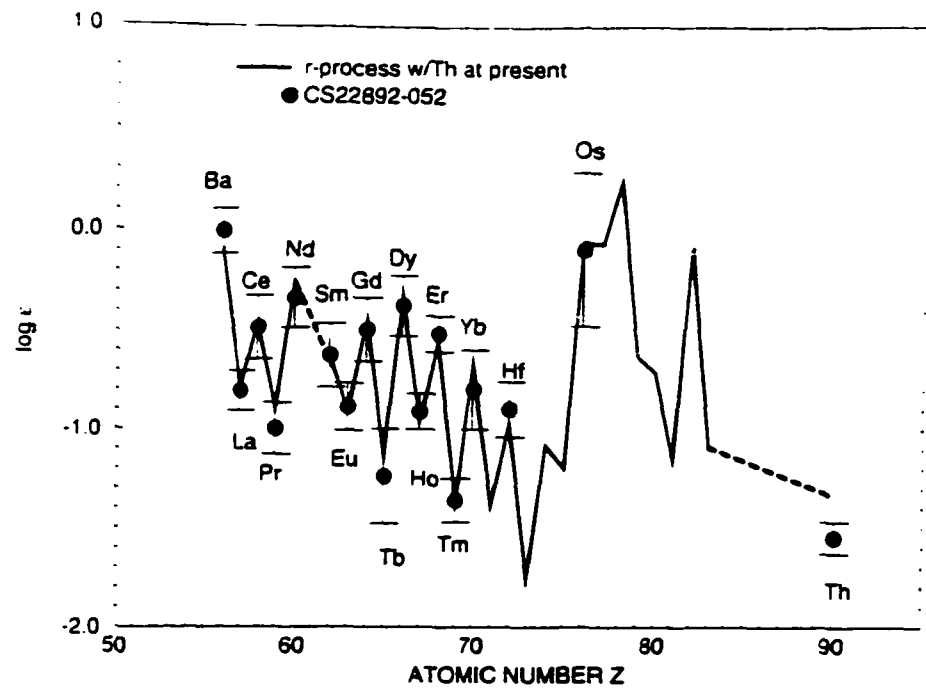
Figure 2.11 Comparison of observed abundances from CS22892-052 with a solar r-process elemental abundance curve with the thorium abundance at present. Error bars are as in Figure 2.10.

Chapter III: Burris et al. (1998):"Like Diamonds in the Sky...."

A. Introduction

The oldest metal-poor halo stars are Galactic "fossils" which provide clues to the conditions and populations of stars that existed early in the Galaxy's history. The chemical compositions of these halo stars presumably came from a few, perhaps only one, generations of stars. These metal-poor stars provide an opportunity to observe neutron-capture elements (Z >30) produced in the unseen precursors to Population II, and through their abundances, to deduce characteristics of the first Galactic stellar population.

These neutron capture (n-capture) elements are produced through slow (s-) and rapid (r-) neutron-capture processes. The s- and r-processes are believed to occur at different sites. The r-process requires a high neutron flux level (with many neutron captures over a timescale of a fraction of a second) thought to occur in supernova explosions, while the s-process, which requires a lower neutron flux (with a typical neutron capture taking many years to occur), is generally thought to occur during the double-shell burning phase of intermediate mass AGB stars. In the solar system, where the abundances of individual isotopes can be determined (Anders & Ebihara 1982, Anders & Grevesse 1989, Käppeler et al. 1989, Wisshak et al. 1996), it is possible to identify the relative fractions of elements produced by each process (see Sneden et al. 1996, and Appendix A). Many observational and theoretical studies (Spite & Spite 1978, Truran 1981, Sneden & Parthasarathy 1983, Sneden & Pilachowski 1985, Gilroy et al. 1988, Gratton & Sneden 1991, 1994; Sneden et al. 1994; McWilliam et al. 1995a, 1995b; Cowan et al. 1996, Sneden et al. 1996) have demonstrated that the observed abundances of n-capture elements in metal-poor

stars are consistent with production in the r-process, and at least for the heaviest such elements, correspond to the scaled solar system r-process signature (Gilroy et al. 1988, Cowan et al. 1995, Sneden et al. 1996, Sneden et al. 1998, Cowan et al. 1997, Cowan et al. 1998).

Gilroy et al. (1988) was one of the first large surveys of these metal-poor stars, and confirmed the operation of the r-process at low metallicity. Gilroy et al. also revealed significant star-to-star scatter in the overall abundance level of the n-capture elements with respect to iron for stars with [Fe/H]<-2.0. The surveys of Beers, Preston, & Shectman (1985, 1992) increased many-fold the number of observed ultra-metal-poor stars, extending the range of metallicity over which n-capture element abundance patterns can be investigated. Spectroscopy of a sample of 33 of ultra-metal-poor stars by McWilliam et al. (1995a,b) confirmed the large star-to-star scatter in the [n-capture/Fe] abundance ratios at low metallicity. An extreme example is the n-capture-rich, ultra-metal-poor ([Fe/H]$\simeq$-3.1) star CS22392-052 (McWilliam et al. 1995a,b; Sneden et al. 1994). Cowan et al. (1995) showed that the observed n-capture element abundances display the detailed signature of the scaled solar system r-process abundances. The case became even more compelling when abundances were determined for additional n-capture elements, including several elements (terbium, holmium, thulium, and hafnium) which had never before been detected in metal-poor halo stars (Sneden et al. 1996).

Even with the Gilroy et al. and McWilliam et al. surveys, the number of metal-poor stars with well-determined n-capture abundances remains small, particularly in the metallicity regime -2.5<[Fe/H]<-0.8 (Edvardsson et al. (1993) and Woolf et al. (1995) surveyed numerous stars with metallicities [Fe/H]>-0.8). The metallicity range -2.5<[Fe/H]<-1.5 covers a critical transition during which s-process elements begin to appear in the Galactic chemical mix. Fortunately, the

Bond (1980) survey of metal-poor giants provides a sample of relatively bright stars in the appropriate metallicity range to investigate this transition, and to delineate the galactic history of enrichment of n-capture elements.

In this chapter, we present n-capture element abundances for 46 metal-poor Bond giants. In §2 we present observational data and in §3 the analysis of the abundances. In §4 we discuss the observed abundances in the context of nucleosynthesis and Galactic chemical enrichment, and in §5 we summarize our conclusions.

B. Observations and Reductions

Observations of 46 Bond giants were obtained with the Kitt Peak National Observatory 4-m Mayall telescope during observing runs in November, 1988, and June, 1989. The spectrograph was configured with the 31.6 l mm^{-1} echelle grating, a 226 l mm^{-1} cross dispersing grating blazed at 8500 Å, and the UV fast camera (0.267 m focal length). A $CuSO_4$ filter isolated the second order of the cross disperser. The detectors, 800 x 800 pixel Texas Instruments CCD's designated "TI2" or "TI3," were binned two pixels in the spatial direction to reduce the readout noise. The spectra were aligned nearly parallel to the columns of the CCD to facilitate the extraction of one-dimensional spectra. The stars observed are sufficiently bright that sky subtraction was not needed. The gratings were oriented to provide complete spectral coverage from 4070 to 4710 Å in 18 overlapping orders. Exposure times ranged from 1800s for the brighter stars to 7200s for the fainter ones. Calibration data include 20 bias and 20 flatfield frames taken each night, as well as an overscan region on each CCD frame. Data reductions followed standard IRAF procedures. Each set of calibration frames was combined to remove cosmic ray events and to reduce the noise. For each data image, the bias level determined from the overscan region and the corrected, average bias frame were subtracted. The image was then divided by the bias-corrected, combined, normalized, flatfield frame. The IRAF task apscatter

was used to subtract scattered light in each echelle image, and the one-dimensional spectra were extracted. After the continua were normalized to unity, a list of stellar lines whose wavelengths are well determined in the solar spectrum was used to determine the wavelength calibration. Spectra of a ThAr comparison lamp were also obtained at the beginning and end of each night to provide a wavelength reference.

The resolution of the spectra, measured from the FWHM (0.23 Å) of the stellar lines, is 0.23 Å (R $\sim$ 20,000). The S/N ratio per pixel varies with wavelength from a few hundred (typically 200) at the red end of the spectrum to about 100 at the blue end.

The Bond giants were also observed using the coudé feed telescope and spectrograph to obtain spectra of the red λ6141 Ba II feature. Because the stars are red and the gratings and detectors have greater efficiency in the red, we were able to use the smaller (0.9-m) telescope for these observations. Spectra were obtained in November, 1988, and in May, 1989. The spectrograph was configured with the large collimator, the 632 l mm^{-1} "A" grating, camera 5 (1.08 m focal length), and the "TI3" detector. Exposure times ranged from a few minutes for the brightest stars to 2 hours for fainter stars. Calibration procedures were similar to those described for the 4-m echelle observations. The resolution is slightly lower, 0.28 Å FWHM, and the S/N ratio is typically between 100 and 200 per pixel.

C. Abundance Analysis

The abundance analyses were performed using the LTE spectral line analysis code MOOG, (Sneden 1973), using the same model atmospheres as PSK (Table 3.1) for most stars. New model atmospheres were generated for HD 029574 and HD 082590 in an attempt to improve the fit of the Ti and Fe spectral features from the models of PSK96. The McWilliam et al. (1995a,b) model atmosphere was adopted for HD 126587, which was not included by PSK96. The line lists for the various transitions

and log *gf* values were adopted from the extensive work of Sneden et al. (1996). The lines selected for the abundance analysis were restricted to the observed wavelength range from 4070-4710 Å , with one additional order near 6141 Å . No analysis was performed in the range from 4225-4280 Å due to the contamination from CH G-band features. Since the *n*-capture elements have transitions which are quite weak, only the strongest of these transitions could be analyzed. Thus, our choice of available elements was somewhat restricted. We did not include some elements which do appear in more metal-rich stars, such as Sm and Ce, because they become undetectable in lower metallicity stars at our resolution and S/N. Thus, we included elements that appear in our spectra over a wide range of [Fe/H].

Before deriving abundances of the neutron-capture elements, we determined abundances of Ti and Fe from up to 10 ionized species transitions in the 4450–4700 Å region of our blue echelle spectra, to establish whether the PSK96 model atmospheres employed with our echelle spectra here yield metallicities in reasonable agreement with the PSK96 results. In Figure 3.1 we correlate abundances derived from the newly-measured Fe II and Ti II lines (and PSK96's Ca I abundances) with [Fe/H]$_{PSK96}$. The "Fe-metallicities" compared in the top panel are in excellent accord: $< \delta[\text{Fe/H}]> = +0.06 \pm 0.02$ ($\sigma = 0.16$; 46 stars), in the sense Fe II *minus* Fe$_{PSK96}$. There is no anomalous trend with metallicity in this comparison (nor in the other two comparisons as well). Our derived [Ti II/H] abundances share with [Ca I/H]$_{PSK96}$ the overabundances of α-process elements commonly seen in metal-poor stars. However, our Ti II overabundances are somewhat larger: $<([\text{Ti II/H}]-[\text{Fe/H}]_{PSK96})> = +0.45 \pm 0.03$ ($\sigma = 0.20$), as compared with $<([\text{Ca I/H}]-[\text{Fe/H}]_{PSK96})> = +0.23 \pm 0.02$, ($\sigma = 0.12$). A discussion of whether this difference between Ti II and Ca I abundances is astrophysical or analytical is beyond the scope of this paper. We caution that the Fe II and Ti II lines in many of our

59

more metal-rich and cooler stars are quite strong. They lie on the flat part of the curve-of-growth and thus abundances derived from them are sensitive to choices of microturbulent velocity. We also note in Figure 3.1 that there appears to be an increase in the scatter of the [Ca I/H] value for the lowest metallicity stars. In this case, however, we are unable to discern whether this might be caused by an astrophysical effect or by observational uncertainties.

The majority of the transitions which we considered were plagued by blending from other features, therefore we chose to perform spectral syntheses rather than determining the abundances from fine analysis. The lines were fit by choosing an initial array of 4 abundances relative to solar values (typically ranging from one-tenth solar to three times solar), then allowing the code to calculate the synthetic line fit. After the initial pass, the abundances were then adjusted to focus in the best fit. The increments in the adjusted abundances were equipartitioned in order to reduce the human error in determining the abundance by eye. With two exceptions, we were able to derive the neutron-capture element abundances from at least two detected lines. In two stars (HD 232078 and BD+302611), spectra of the 4077 region were not available; in these stars, the Sr and Dy abundances are from single lines. Figure 3.2 shows examples of these syntheses for HD 063791. In the case of Nd 4446 Å and 4462 Å we were able to employ fine analysis, due to lack of blending. These lines were measured with the equivalent width subroutine of the SPECTRE code Fitzpatrick & Sneden (1987). Then the equivalent widths were put into MOOG for abundance determinations. These abundances were then coupled with the syntheses abundances obtained for the Nd 4358 Å and 4109 Å lines to obtain a final Nd abundance for all stars.

The elements Ba and Eu must be given special attention, since they are subject to isotopic hyperfine splitting which can affect the final abundances. Hyperfine

splitting is considered for both these elements in the same fashion that it is treated in Sneden et al. (1996). Sr and Ba abundances are also sensitive to changes in the microturbulent velocity because they are strong lines, with equivalent widths ≥ 60 mÅ. Several of the stars showed a difference between the Ba abundance derived from the 4554 Å line and the 6141 Å features. The abundance from the 6141 Å line was in better agreement with the value for Ba obtained from the scaled r-process solar curve than the abundance from the 4554 Å line. The 4554 Å line is much stronger and more sensitive to changes in the microturbulent velocity. These disparities were eliminated by raising slightly the microturbulent velocity (+0.2 km/s maximum) from an initial value taken from PSK96. The choice of a higher microturbulence also decreased the Sr abundance in these same stars by $\simeq 0.15$ dex, bringing the Sr results into better agreement with the scaled solar system r process curve, as well. Tables 3.2 and 3.3 present the n-capture elements abundances as log ϵ(M) and [M/H] where log ϵ(M)$\equiv$ log$_{10}$(N_M/N_H) + 12.0.

Many of the Bond Giants have been studied by previous authors. BD+58 1218, HD 002665, HD 006755, HD 063791, HD 110184, and HD 122563 were all included by Gilroy et al. (1988). Our analysis results agree with Gilroy's results, having a scatter of about 0.20 dex, with the exception of Sr, which has a scatter of about 0.33 dex. HD 122563, HD 122956, HD 165195, and HD 187111 are included by Gratton & Sneden 1994. Again, our results agree with the results of Gratton & Sneden with the scatter of also about 0.20 dex. Here again, the comparisons of Sr results have slightly higher scatter, with the average scatter in the results being about 0.45 dex.

D. Discussion

D.1 Star-to-Star Scatter

In this section we investigate the star-to-star scatter in the neutron capture elements relative to iron. Figure 3.3 compares the spectra of BD +09 2870 and HD

6268, two very similar stars with the same atmospheric parameters and metallicity ([Fe/H]=-2.4). The top panel shows that the Fe II, Cr II, and Ti II lines have similar strengths in the two stars. The second and third panels show that despite the similarity of the transition metal lines, lines of the neutron-capture elements Eu, La, Dy, and Nd show quite different strengths. It should be noted that all of the n-capture elements shown here vary together from star-to-star. In other words, the abundances of La, Eu, Dy and Nd are always larger in HD 6268 than in BD + 09 2870, and the relative ratios of those elements are approximately the same in both stars. We also compare the relative abundances of these elements in each star with a scaled solar system r-process elemental distribution, determined as described in Appendix A.1. It is clear from the figure that for the four elements observed, both stars have a relative abundance pattern that is consistent with the solar r-process distribution.

Global comparisons of the abundance strengths of a number of elements are shown in Figure 3.4. In the top panel of Figure 3.4 the [element/Fe] ratios of the sample stars are compared for α and Fe-peak elements. The stars have been divided into two classes based upon their metallicities, with the separation being made at [Fe/H] = -2. The star-to-star variations illustrated here are relatively modest and are indicative of the observational scatter in the data. It is also clear from the data that there is little difference in these elemental abundances as a function of metallicity.

A different pattern appears in the middle panel of Figure 3.4. The scatter is significantly larger than for the lighter elements in the upper panel, with the spread of [Eu/Fe] and [Dy/Fe] exceeding a factor of ten throughout our metallicity regime (see also Figure 3.5). The scatter of the n-capture elements abundances with respect to iron appears to be real and not the result of observational error. This follows from a comparison of the same n-capture elements with respect to Eu, as shown

in the bottom panel of Figure 3.4. This decreased scatter is seen in more detail in Figure 3.5 where we examine the abundance of Eu and Dy. The top two panels in ·his figure show the [Eu/Fe] and [Dy/Fe] variation by an order of magnitude from solar. This large scatter, however, is not seen in [Dy/Eu] (shown in the lowest panel), as it would if caused by observational error. The [Dy/Eu] ratios, in fact, are within approximately ± 0.25 of the solar value for the whole metallicity range studied. Most of the [Nd/Eu] ratios are within approximately ± 0.4 dex of the solar value, while the [La/Eu] values are tightly clumped within −0.1 to −0.5 dex below the [el/Eu] = 0 line. [Ba/Eu] shows more scatter, and we also note that for this ratio there is a clear distinction between the lower ([Fe/H] < −2) and higher ([Fe/H] > −2) metallicity stars. Both of these behaviors are consistent with Ba being synthesized primarily by the s-process in slowly evolving, low-mass stars. (See below for further discussion of Ba synthesis.)

Our data, as illustrated in Figures 3.4 and 3.5, demonstrate that the abundances of Dy, Nd, La, Eu and to a lesser extent Ba all appear to be correlated and all the other elements appear to correlate with the Eu abundance, in contrast to their behavior with iron. This strongly argues that the heaviest n-capture elements were produced in concert (i.e., in a common synthesis) with Eu, which is produced almost exclusively in the r-process (see Appendix A.1).

The lighter n-capture elements shown in Figure 3.4 do not show the same reduction in scatter seen for the heavier such elements, and this may reflect the influence of the s-process. It is also evident that for La, Nd and Dy there is little difference in the abundance ratios as a function of metallicity.

The overall star-to-scatter for all of the sample stars, as well as samples from other studies, as a function of metallicity is shown in Figure 3.6. The average abundance of the neutron-capture elements with respect to iron is plotted versus

[Fe/H]. The averages (actually geometric means) were computed simply by adding the abundances ([el/Fe]) together, then dividing by the number of elements involved. For stars included in this chapter this average includes Ba, La, Nd, Eu, and Dy. For the other literature stars, these elements were included where available. As metallicity increases in Figure 3.5, the scatter in the average, heavy n-capture element abundances declines. This apparent trend was noted previously by Gilroy et al. (1988), but is now seen much more convincingly with more extensive and better data. We would suggest (in agreement with Gilroy et al., see also McWilliam 1998) that this star-to-star scatter is most easily explainable as resulting from a local nucleosynthetic effect. In other words, some interstellar matter (participating in star formation) closer to a site for r-process nucleosynthesis, presumably a supernovae, would be enriched while other interstellar matter would not. This scatter is also seen in the low metallicity halo planetary nebulae (Howard 1998) We stress, however, that the observed star-to-star scatter appears in the total abundance level with respect to iron and not in the relative n-capture abundances. Our results, as well as other studies (see e.g., Cowan et al. 1997, Sneden et al. 1996, 1998), demonstrate that those relative abundances appear to be similar in all the metal-poor halo stars, and in solar system r-process proportions (see Table A.1.2).

Our data, as shown in Figure 3.6, demonstrate that the overall scatter seems to have dropped to zero by the time [Fe/H] = -1.2. This presumably marks the metallicity (and some associated Galactic time) when the stellar chemical abundances have become homogenized and when the Galaxy became more thoroughly chemically mixed (see also McWilliam 1998). This may also be related to the disk-halo transition.

Our results further suggest that iron production is not tied to the same astrophysical site as r-process nucleosynthesis. Instead, it may be that there is

only a narrow range of (perhaps low-mass) supernovae responsible for r-process nucleosynthesis (Mathews & Cowan 1990; Wheeler, Cowan, & Hillebrandt 1998). Alternatively, other possible r-process sites, might also participate in this early Galactic r-process nucleosynthesis, and would not be involved in iron synthesis. One such suggested site, for example, is neutron star-binaries (see Mathews et al. 1992; Thielemann & Benz 1998). Finally, it should be noted if the metallicity could be tied to an age relationship, the star-to-star scatter evidenced in the data could define the mixing timescale for the Galaxy to become homogeneous.

D.2 Abundance Trends

D.2.1 Heavier N-capture elements

In the previous section we saw how the heavier n-capture elements seem to vary together in concert. In this section we examine more closely the abundance trends of individual n-capture elements as a function of metallicity. Two elements that have been examined extensively in the past are Ba and Eu. Ba in the solar system is made predominantly in the s-process, while Eu is synthesized in the r-process (see Table A.1.2 in Appendix A.1). The behavior of the ratio of these two elements with metallicity is illustrated in Figure 3.7. In addition to our new sample stars, we have plotted the results of Gilroy et al. (1988), Gratton & Sneden (1994), McWilliam (1998), Woolf et al. (1995), Edvardsson et al. (1993), François et al. (1993) and François (1996). Our new data demonstrate, with the literature data sets in agreement, that for the lowest values of [Fe/H], Ba and Eu appear to be made in concert, with their ratio increasing linearly with metallicity. This is also illustrated clearly in Figure 3.8, where we examine the abundance behavior of Ba with respect to Eu. A least-square-fit to our new sample data is indicated by a straight line. This line has a slope of approximately 40^0, which is within reasonable oservational uncertainties and for the whole metallicity range, close to 45^0. (Omitting the most

metal-rich stars in our data will also tend to push the slope closer to 45^0.) Such a slope strongly suggests that for these lowest metallicity stars, the same process is responsible for producing both Ba and Eu.

Eu is only made by the r-process and Figures 3.7 and 3.8 clearly indicate that at low metallicities Ba is also made in the same process. This suggestion has been made previously (Spite & Spite 1978; Truran 1981) based upon data for a few individual, metal-poor stars. The well-studied ultra-metal-poor star CS 22892–052, for example, has a n-capture signature, including Ba and Eu, that is most likely explained as being produced solely by the r-process (Sneden et al. 1996,1998; Cowan et al. 1998). There have been suggestions in the past, however, that this was only a happy coincidence or the result of some random event, seen only in a few stars. Here we observe the same ratio of Ba to Eu in a number of stars at low metallicity, suggesting that Ba and Eu are made together in the r-process during the early history of the Galaxy, and making other suggestions (i.e., an early Galactic s-process origin for Ba) for the Ba/Eu ratio in these stars much less likely.

We have indicated the solar system "pure" r-process value as a dashed line in Figure 3.7. We see that at lowest metallicities, within the scatter, that our sample stars appear to have this ratio. Our results are also consistent with the recent results for the smaller sample of McWilliam (1998). We stress the need for additional data for stars with [Fe/H] between –3 and –4 to strengthen this conclusion on the nature of the early synthesis of these elements. The results presented here further suggest that the r-process sites (the progenitors to the halo stars) must have evolved rapidly during the early history of the Galaxy to synthesize the n-capture elements. (See Cowan, Thielemann, & Truran 1991, Mathews, Bazan, & Cowan 1992, and Meyer 1994 for a discussion of possible r-process sites.)

In Figure 3.7 we note a change in the slope of the [Ba/Eu] ratio at [Fe/H] = –2.2

± 0.1. At this metallicity the ratio seems to flatten with (presumably) increased production of Ba. Since Ba is predominantly an s-process element, the data seem to indicate the onset of Galactic s-processing at this particular metallicity, sometime after the earlier r-process synthesis. This delay in s-processing is consistent with a longer stellar evolutionary timescale typical of low-mass stars, thought to be the site for this type of n-capture synthesis (Gallino et al. 1998). Nevertheless, there may be a mass range in these s-process sites and the first slope change in our data at [Fe/H] = -2.2 may indicate the initial appearance of the s-process from the most massive of these low-mass stars. (This would tie the metallicity value of -2.2 to an age consistent with the lifetime of perhaps a 2-3 $M_\odot$ star.) Detailed analyses of the abundances of the metal-poor star HD 126238, [Fe/H] = -1.7 (Chapter IV and Cowan et al. 1996), have suggested the presence of some s-processing already at that metallicity, consistent with the global changes noted in our new data. Cowan et al., however, found that only a small percentage (20%) and not the total solar s-processing was in evidence for abundance data in that star. This led them to suggest that the s-process fraction was coming only from the most massive sites at a metallicity of -1.7. Based upon our data, we might speculate therefore that it might not be until the Galactic metallicity reaches approximately -0.6 that the major sites for the s-process have had to time to evolve, and where the [Ba/Eu] ratio turns upward again. We also see further evidence of the major change in the slope of the production of these elements in Figure 8 where a least-squares-fit to the abundances of Ba and Eu in the disk stars (Woolf et al. 1995; Edvardsson et al. 1993) shows a much shallower slope (25 ^{0}) than seen for the more metal-poor stars. This would again indicate the increasing production of Ba at higher Galactic metallicites and later times.

D.2.2 Lighter N-capture elements

67

.

The data indicate that the heavier ($Z \geq 56$) neutron-capture elements are likely explained as being produced solely by the r-process early in the history of the Galaxy, with s-process contributions (to at least Ba) occurring at higher metallicities and later times. The situation is not as easily explainable for the lighter n-capture elements. Unfortunately, the only elements below Ba that have so far been accessible are Sr, Y and Zr. In Figure 9 we illustrate the behavior of [Zr/Fe], [Y/Fe] and [Sr/Fe] as a function of metallicity. We again see the large scatter in the abundance ratios for the lowest metallicity ([Fe/H] <−2.5) stars. At higher metallicites, Sr and Zr, which are made predominantly in the s-process, appear to have essentially solar ratios. For Y, also primarily an s-process element, there seems to be some evidence of a correlation with increasing metallicity, something that is not expected. Naively it would be expected that the behavior of Sr, Y and Zr would all be similar due to their similar s-process origin and closeness in the nuclear chart. Thus, such a metallicity dependence is unexpected. This effect might be due to observational uncertainties in the Y abundance determinations.

Figure 3.10 illustrates the behavior of [Y/Zr] (top panel), [Sr/Ba] (middle panel) and [Sr/Zr] (lower panel) as a function of metallicity. We again see the apparent metallicity dependence on Y in the top panel of Figure 3.10. The abundance trend of [Sr/Ba] as a function of metallicity is indicated in the middle panel of Figure 10. Our new data, as well as the other studies included, demonstrate that this ratio appears to be essentially flat over a very wide metallicity range, indicating some (possible ?) correlation between these elements. There is, however, a very large scatter in the [Sr/Ba] ratios, particularly at low metallicities. (The scatter seems to decrease at higher metallicities, but that may be due to more limited metal-rich abundance data.) While some of this scatter may be due to observational error, an additional nucleosynthesis source may be required to explain the behavior of Sr. In

solar system material, a sizable contribution to the Sr abundance (and somewhat less for Y and Zr) comes from the weak s-process (in the helium cores of massive stars) (see Raiteri et al. 1993). However, at very low metallicities, this synthesis process would be lessened due to the lower initial iron abundances in the progenitor stars. Thus, at low metallicities only an r-process synthesis might be possible. An additional difficulty in understanding the source of the Sr abundance at low metallicities, already noted by McWilliam (1998), is the uncertainty in the solar system r-process abundance for this element.

Based upon solar system meteorite data, it has been suggested that there may be two separate r-process sites, with one for those elements above Ba and a different one for the lighter n-capture elements (Wasserburg, Busso, & Gallino 1996; Qian, Vogel, & Wasserburg 1998). In addition to massive stars (Woosley et al. 1994) and low-mass supernovae (Mathews et al. 1992; Wheeler et al. 1998), neutron-star binaries have also been suggested as possible r-process sites (Lattimer & Schramm 1977; Mathews et al. 1992; Thielemann & Benz 1998). We can speculate that the presence of r-process material early in the history of the Galaxy, at very low metallicity, might suggest supernovae as a likely source for the heaviest n-capture elements, with (perhaps) binaries contributing at later times and more infrequently to the lighter n-capture abundances. It is also interesting to note that some contribution to the scatter in the data at metallicities > -2 might be from the weak s-process.

Examination of the lower panel in Figure 3.4 indicates that Sr does not correlate with Eu, which might support the idea of two separate r-process sites, and/or a contribution from the weak s-process to the Sr abundance. On the other hand, Sr does seem to correlate with Zr as demonstrated in Figure 3.10, where we show the abundance trend for [Sr/Zr] as a function of [Fe/H]. We note, however, that there

is a great deal of scatter in the data, again suggesting additional contributions to the Sr abundances. We caution at this point, however, that the stellar data for the lighter n-capture elements are still not extensive enough to lead to an unambiguous explanation for the origin of these elements, and more abundance data and theoretical work will be required.

E. Conclusions

We have presented new neutron capture abundance results for 46 metal-poor Bond giants. By using the results from our new analyses in concert with the results of previous authors, several results have been shown which agree with results of previous authors. It has been shown that there exists real star-to star scatter in the abundances of the elements, indicating inhomogeneity of the Galactic material at early times in the Galaxy's history. As the metallicity increases, as does presumably the age of the Galaxy, the scatter decreases, indicating that mixing of the material must be taking place. Even though this dispersion exists in the absolute abundances, the correlation of the elements Ba (an s-process element) and Eu (an r-process element) at low metallicity indicate that the heavy neutron capture were formed via the r-process early on, again confirming the work of previous authors (Sneden et al. (1996) and others). This fact can help constrain the sorts of objects that were the progenitors of these metal poor halo stars. Further observations at very low metallicities ([Fe/H]$\leq$-2.5) would be useful to fill in the gap. There is a distinct turn-on of the contribution of the s-process to the abundance of elements such as Ba at a metallicity of [Fe/H]$\simeq$-2.0. The abundance results for the lighter neutron capture elements (Sr-Y-Zr) are less satisfying. The failure of the abundances of these elements to follow the same trends as the heavier neutron capture elements indicates that Sr-Y-Zr must not be formed via the same process as the elements such as Ba, Eu etc. at early times in the Galaxy's history. In order to resolve this problem, it

would be helpful if further observations of these elements could be obtained, as well as observations of other elements in the same mass region.

TABLE 3.1. Model Atmosphere Parameters

Star	Teff	log g	[M/H]	v$_t$
b−012916	4150	0.10	-1.80	2.30
b−060648	4500	1.10	-2.00	2.00
b−092870	4600	1.40	-2.20	1.70
b+093223	5350	2.00	-2.20	2.00
b+112998	5425	2.30	-1.20	2.00
b+173248	5250	2.30	-1.80	1.50
b+302611	4275	0.80	-1.40	2.10
b−541323	5300	2.50	-1.50	1.70
b−581218	5000	2.20	-3.00	1.00
c-241782	5300	2.80	-2.20	1.50
hd000020	5475	2.80	-1.20	2.00
hd002665	5000	2.20	-3.00	1.30
hd002796	4900	1.60	-3.00	1.60
hd006268	4700	1.60	-3.00	1.60
hd006755	5150	2.70	-1.25	1.40
hd008724	4500	1.20	-2.20	1.60
hd013979	5075	1.90	-3.00	1.30
hd025532	5300	1.90	-1.20	2.30
hd026297	4400	1.10	-1.70	2.00
hd029574	4250	0.00	-1.65	1.90
hd044007	4850	2.00	-1.50	1.50
hd063791	4725	1.70	-1.50	1.60
hd074462	4600	1.50	-1.40	1.80
hd082590	6150	2.70	-1.00	3.10
hd085773	4450	1.10	-2.00	2.10
hd105546	5300	2.50	-1.00	1.50
hd110184	4250	0.30	-2.20	2.10
hd122563	4625	1.40	-3.00	1.70
hd122956	4600	1.50	-1.70	1.80
hd126587	4910	1.85	-3.00	2.00
hd135148	4275	0.80	-1.70	2.10
hd165195	4450	1.10	-2.00	1.90
hd166161	5150	2.20	-1.00	2.00
hd171496	4700	1.60	-1.00	1.50
hd175305	5100	2.50	-1.50	1.40
hd184266	5600	1.70	-1.70	2.00
hd186478	4575	1.40	-2.20	2.00
hd187111	4250	0.70	-1.70	1.70
hd204543	4700	1.70	-1.50	2.00
hd206739	4675	1.70	-1.70	1.70
hd216143	4525	0.80	-2.00	1.80
hd218857	5125	2.40	-2.00	1.20
hd220838	4450	1.20	-1.70	1.90
hd221170	4425	1.00	-2.00	1.79
hd232078	4000	0.30	-1.50	2.60

TABLE 3.2. Abundances ([m/Fe]) for Program Stars

Star	[Fe/H]	[Sr/Fe]	[Y/Fe]	[Zr/Fe]	[Ba/Fe]	[La/Fe]	[Nd/Fe]	[Eu/Fe]	[Dy/Fe]
BD+01 2136	-1 39	1 39	-0 07	0 64	0 07	0 35	0 42	0 45	
BD+06 648	-2 10	0 35	-0 03	0 33	0 15	0 13	0 34	0 29	0 40
BD+09 2870	-2 37	-0 20	-0 25	0 05	-0 46	-0 53	-0 40	-0 25	-0 23
BD+09 3223	-2 26	0 16	0 00	0 44	0 41	0 20	0 17	0 42	0 35
BD+11 2998	-1 17	0 27	-0 23	0 17	0 41	-0 17	-0 10	0 06	0 05
BD+17 3248	-2 02	0 55	0 06	0 50	0 97	0 60	0 88	0 96	0 96
BD+30 2611	-1 49	0 50	-0 20	0 04	0 06	0 15	0 77	0 45	
BD+54 1323	-1 55	0 57	-0 14	0 20	0 37	0 11	0 29	0 47	0 55
BD+58 1218	-2 72	0 17	-0 10	0 06	-0 50	-0 30	0 03	0 21	0 37
CD-24 1782	-2 70	-0 10	0 24	0 50	-0 38	0 33	0 60	0 49	0 35
HD 20	-1 39	0 05	-0 05	0 46	0 58	0 39	0 58	0 77	0 92
HD 2665	-1 97	-0 45	-0 39	-0 20	-0 08	-0 19	0 22	0 23	0 26
HD 2796	-2 23	0 13	-0 39	-0 07	0 00	-0 22	-0 24	-0 06	0 03
HD 4306	-2 54				-1 09				
HD 4268	-2 36	0 04	-0 18	0 32	0 50	0 21	0 39	0 52	0 68
HD 6755	-1 57	-0 06	-0 26	0 07	0 15	0 09	0 42	0 50	0 52
HD 8724	-1 64	0 04	-0 25	-0 06	0 00	-0 07	0 07	0 20	0 47
HD 13979	-2 26	-0 07	-0 63	-0 34	-0 50	-0 10	-0 40	-0 38	-0 10
HD 25532	-1 46	0 14	-0 28	0 14	0.00	-0 07	0 00	0 10	0 26
HD 26297	-1 87	0 12	-0 12	0 06	-0 26	-0 21	0 14	0 11	0 37
HD 29574	-1 61	0 41	-0 24	0 59	0 39	0 38	0 18	0 76	
HD 44007	-1 70	0 20	0 36	0 22	0 05	-0 20	0 46	0 19	0 22
HD 63791	-1 68	0 06	-0 10	0 06	0 05	-0 21	0 15	0 12	0 23
HD 74462	-1 56	-0 09	-0 14	0 02	0 00	-0 06	0 41	0 32	0 49
HD 82590	-1 32	0 07	-0 17	0 25	0.70	0 12	-0 03	0 39	0 37
HD 85773	-2 36	-0 31	-0 31	0 07	-0 49	0 09	0 19	0 24	0 48
HD 105546	-1 27	0 45	0 13	0.48	0 42	0 05	0 30	0 32	0 19
HD 110184	-2 56	0 64	0 46	1 13	0 01	0 11	0 29	0 45	
HD 122563	-2 71	0 06	-0 14	0 31	-0.92	-0 71	-0 59	-0 30	-0 39
HD 122956	-1 76	0 16	-0 18	0 16	0 15	0 04	0 43	0 55	0 60
HD 126587	-2 65	-0 45	0 01	0 50	-0 06	0 30	0 75	0 75	0 65
HD 135148	-1 90	1 25	0 66	0.50	0 30	0.27	1 07	0 56	
HD 165195	-2 24	0 55	-0 16	0 42	0 23	0 19	0 35	0 54	0 57
HD 166161	-1 30	0 20	0 31	0 43	0 53	0 36	0 33	0 10	0 23
HD 171496	-0 91	0 06	-0.13	-0.26	-0.07	-0 47	0 15	-0 15	0 10
HD 175305	-1 40	0 13	-0 11	0.10	0.12	0 05	0 34	0 44	0 40
HD 184266	-1 73	-1 03	-0 41	0.10	0.90	-0.01	0 59	0 28	0 27
HD 186478	-2 56	0 36	-0 01	0.40	0 00	-0.04	0 30	0 57	0 68
HD 187111	-1 74	0 60	-0 28	0 52	0 10	0 06	0 09	0 36	
HD 204543	-1 64	0 00	-0 12	0 20	0.40	0 27	0 59	0 46	0 79
HD 206739	-1 56	0 10	0 00	0.00	0.00	-0.17	0 24	0 35	0 48
HD 216143	-2 16	0.33	-0 17	0 13	0.03	0 06	0 30	0 43	0 63
HD 216657	-1 66	0.01	-0 17	0.00	0 03	-0 36	-0 06	-0 23	-0 40
HD 220838	-1 65	0 15	-0 03	0.10	0 00	-0.20	0 41	0 30	0 50
HD 221170	-2 15	0 62	-0 14	0 28	0.50	0.50	0 75	0 40	0 65
HD 232078	-1 54	1 04	-0 10	0.34	0.06	0 12	0 69	0 40	

73

TABLE 3.3. Abundances (loge(m)) for Program Stars

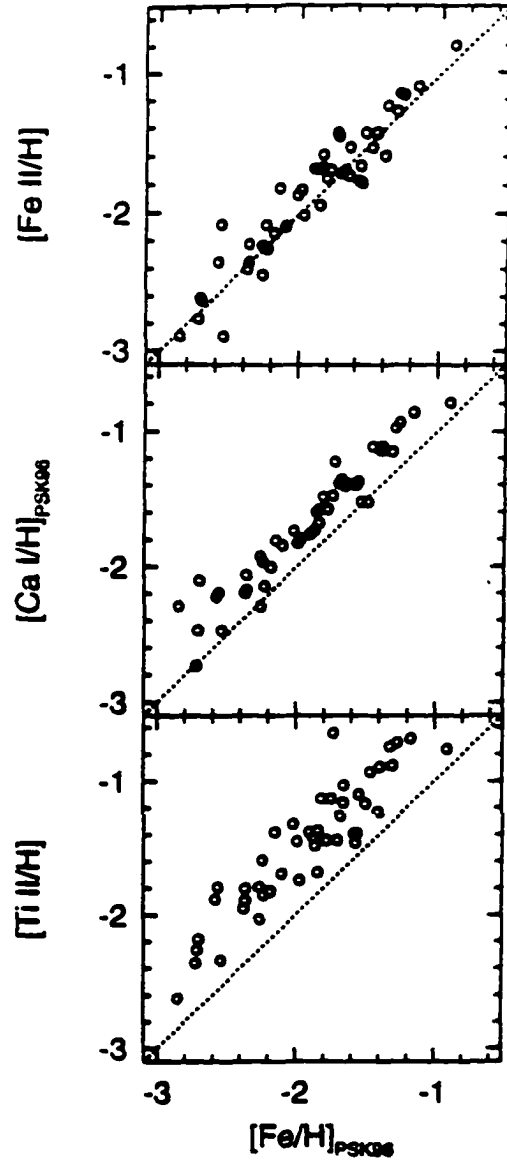| Star	loge(Sr)	loge(Y)	loge(Zr)	loge(Ba)	loge(La)	loge(Nd)	loge(Eu)	loge(Dy)
BD+01 2196	2.30	0.16	1.25	0.21	-0.42	-0.07	-0.63	
BD+06 648	1.15	0.11	0.63	0.16	-0.73	-0.26	-.10	-.40
BD+09 2670	0.33	-0.36	0.26	-0.70	-1.66	-1.27	. ..	-.50
BD+09 3223	1.90	-0.02	1.76	0.26	-0.64	-0.59	-1.33	1.51
BD+11 2998	2.30	0.64	1.60	1.37	-0.12	0.23	-0.60	-1.12
BD+17 3246	1.43	0.26	1.06	1.06	-0.20	0.36	-0.55	1.04
BD+30 2611	1.91	0.55	1.15	0.72	-0.12	1.76	-0.53	
BD+54 1323	1.62	0.45	1.15	0.65	-0.32	0.14	-0.67	1.10
BD+56 1216	0.35	-0.56	-0.06	-1.09	-1.60	-1.19	-2.00	-1.25
CD-24 1762	0.10	-0.22	0.40	-0.95	-1.15	-0.60	-1.70	-1.25
HD 20	1.56	0.60	1.67	1.32	0.22	0.69	-0.11	1.63
HD 2665	0.46	-0.12	0.43	0.11	-0.94	-0.25	-1.23	-0.59
HD 2796	0.60	-0.36	0.30	-0.10	-1.23	-0.97	-1.76	-1.10
HD 4306				-1.50				
HD 6268	0.62	-0.30	0.56	0.27	-0.93	-0.47	-1.33	-0.56
HD 6755	1.25	0.41	1.10	0.71	-0.26	0.35	-0.56	1.05
HD 6724	1.10	0.15	0.70	0.29	-0.69	-0.27	-1.13	-0.27
HD 13979	0.57	-0.65	0.00	-0.63	-1.14	-1.16	-2.13	-1.26
HD 25532	1.56	0.50	1.28	0.67	-0.31	0.04	-0.65	-0.10
HD 26297	1.15	0.25	0.79	0.00	-0.66	-0.23	-1.25	1.40
HD 29574	1.50	0.19	1.38	0.60	-0.21	-0.15	-0.54	
HD 44007	1.40	0.90	1.12	0.46	-0.66	0.26	-1.30	0.36
HD 63791	1.26	0.46	0.96	0.50	-0.67	-0.03	-1.05	-.35
HD 74462	1.25	0.54	1.06	0.57	-0.40	0.35	-0.73	1.03
HD 62590	1.65	0.75	1.53	1.54	0.02	0.15	-0.42	1.15
HD 65773	0.23	-0.43	0.31	-0.72	-1.05	-0.67	-1.61	-0.76
HD 105546	2.06	1.10	1.76	1.26	0.00	0.53	-0.44	0.02
HD 110184	0.96	0.14	1.17	-0.42	-1.23	-0.77	-1.60	
HD 122563	0.25	-0.60	0.20	-1.50	-2.20	-1.60	-2.50	-2.00
HD 122956	1.30	0.26	0.96	0.50	-0.52	0.15	-0.72	-0.06
HD 126587	-0.40	-0.60	0.25	-0.78	-1.33	-0.60	-1.59	-1.10
HD 135146	2.25	1.22	1.20	0.53	-0.41	0.67	-0.61	
HD 165195	1.21	-0.16	0.76	0.12	-0.63	-0.39	-1.15	-0.57
HD 166161	1.60	1.25	1.73	1.36	0.26	0.53	-0.69	0.03
HD 171496	2.05	1.20	1.43	1.15	-0.16	0.74	-0.55	0.29
HD 175305	1.63	0.73	1.30	0.65	-0.13	0.44	-0.45	0.10
HD 184266	2.20	0.10	0.97	1.30	-0.62	0.36	-0.94	-0.36
HD 186478	0.70	-0.35	0.42	-0.45	-1.40	-0.78	-1.50	-0.60
HD 187111	1.96	0.25	1.36	0.49	-0.46	-0.15	-0.87	
HD 204543	1.06	0.26	0.96	0.69	-0.37	0.26	-0.67	0.05
HD 206739	1.42	0.66	1.02	0.55	-0.53	0.16	-0.72	0.00
HD 216143	1.05	-0.11	0.55	-0.02	-0.90	-0.36	-1.24	-0.45
HD 216467	1.06	0.21	0.74	0.30	-1.00	-0.42	0.16	
HD 220838	1.40	0.56	1.06	0.46	-0.63	0.26	-0.44	-0.05
HD 221170	1.37	-0.05	0.60	0.46	-0.43	0.10	-0.44	-0.20
HD 232078	2.40	0.60	1.40	0.65	-0.20	0.65	-0.63	

74

Figure 3.1 Top panel: Comparison of iron abundance from this work with PSK. Middle panel: Comparison of [Ca/H] as a function of metallicity, lower panel: comparison of [Ti/H] as a function of metallicity.
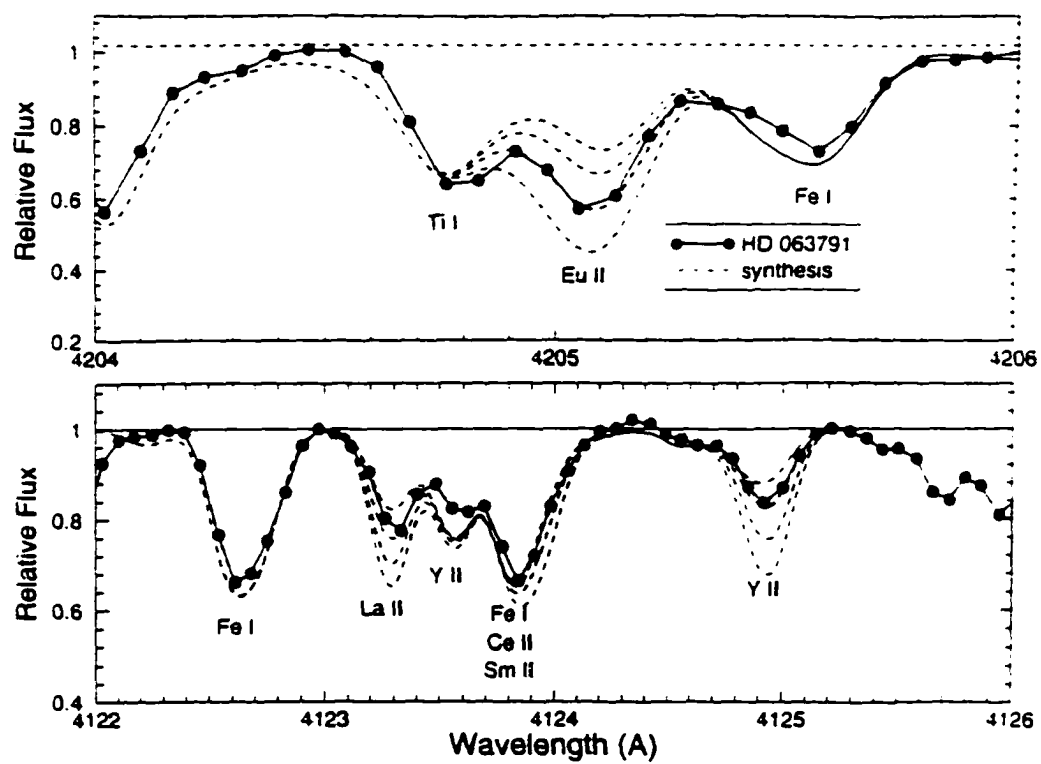
Figure 3.2 Spectrum synthesis for (a) (lower panel) the La 4123 Åand (b) (upper panel) Eu 4205 Ålines for HD 063791.
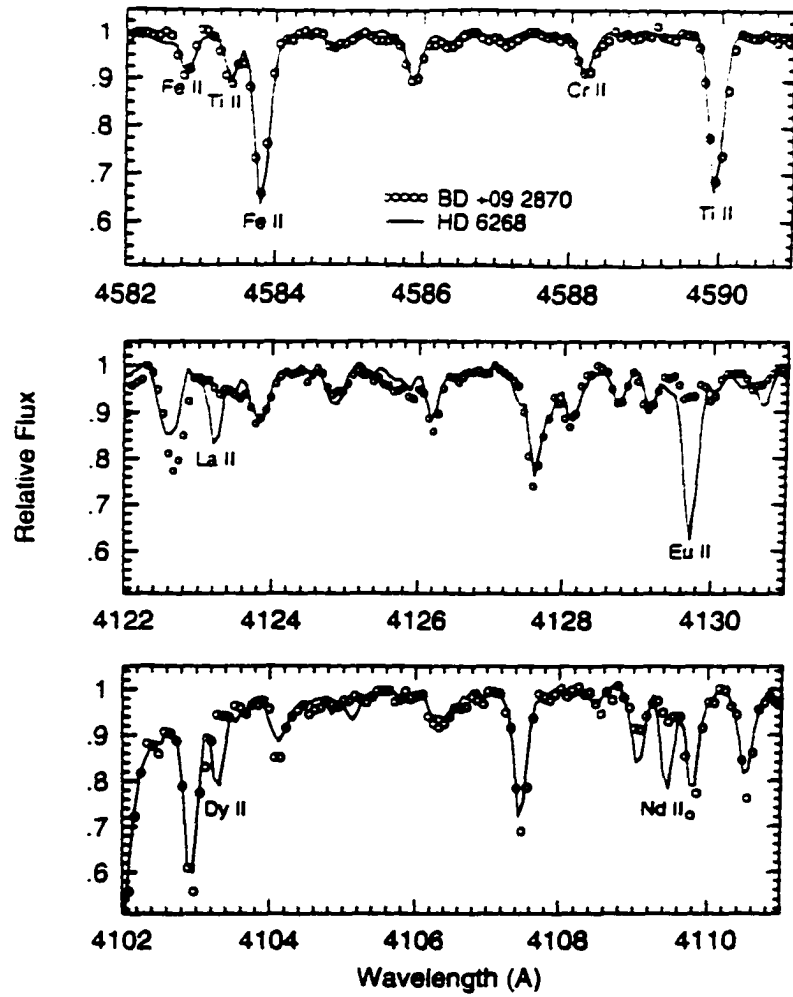
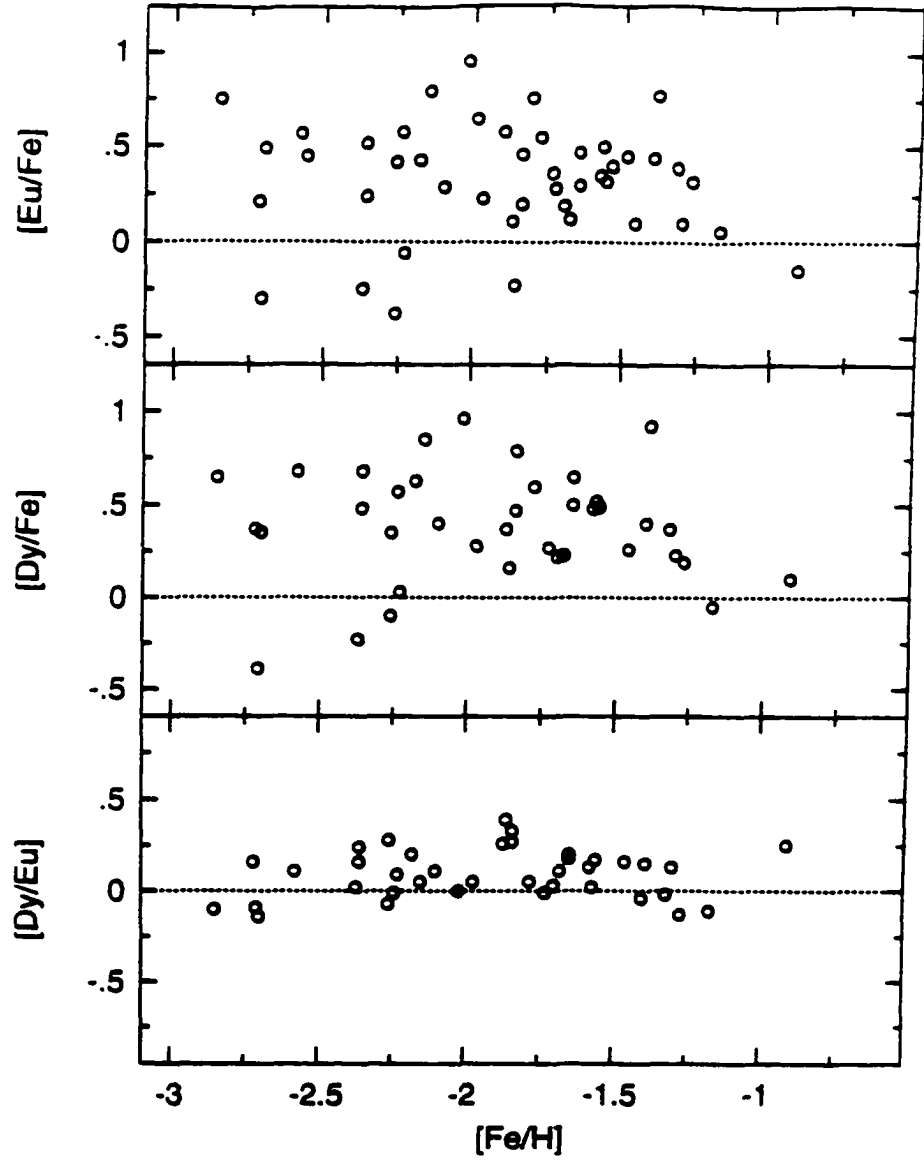Figure 3.3 Spectral comparison between the two similarly metal-poor stars BD +09 2870 and HD 6268.

Figure 3.4 Abundance comparisons of (a, top panel) [el/Fe] for alpha elements in metal-poor stars, (b, middle panel) [el/Fe] for n-capture elements in metal-poor stars and (c, bottom panel) [el/Eu] for n-capture elements in metal-poor stars.
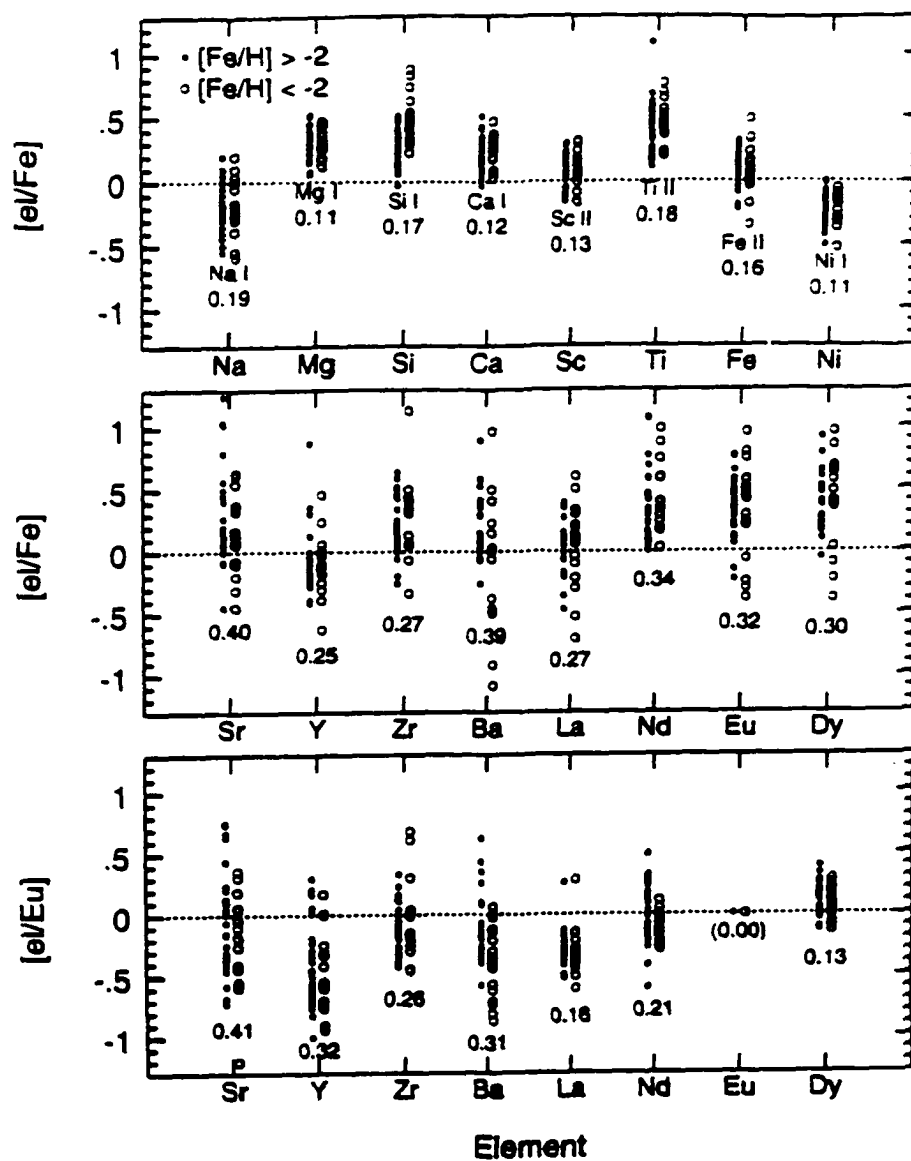
Figure 3.5 Abundance comparisons of (a, top panel) [Eu/Fe] in metal-poor stars, (b, middle panel) [Dy/Fe] in metal-poor stars and (c, bottom panel) [Dy/Eu] in metal-poor stars.
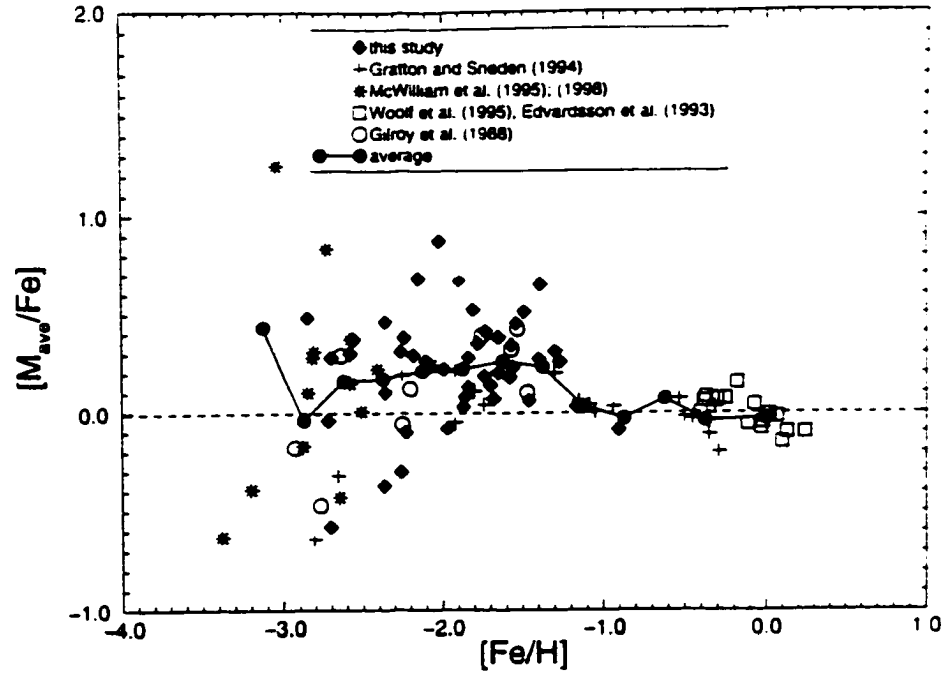
Figure 3.6 Average abundances of n-capture elements/Fe versus metallicity for Galactic stars. The solid line represents the average of individual stars over bins of 0.25 dex in [Fe/H].
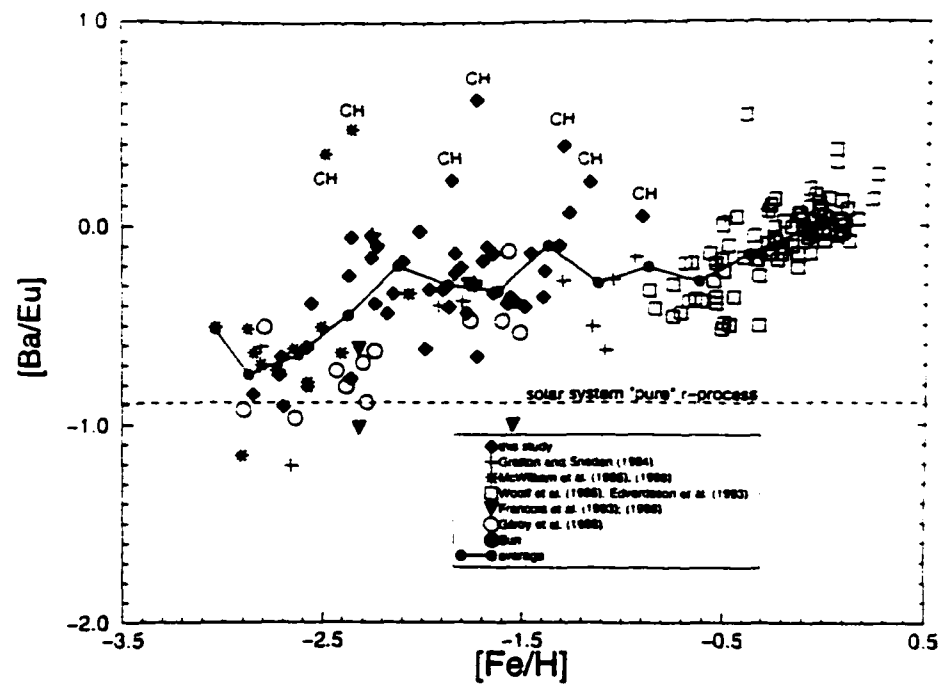
Figure 3.7 [Ba/Eu] versus metallicity for Galactic stars. The solid line represents averages of individual stars in bins of 0.25 dex in [Fe/H].
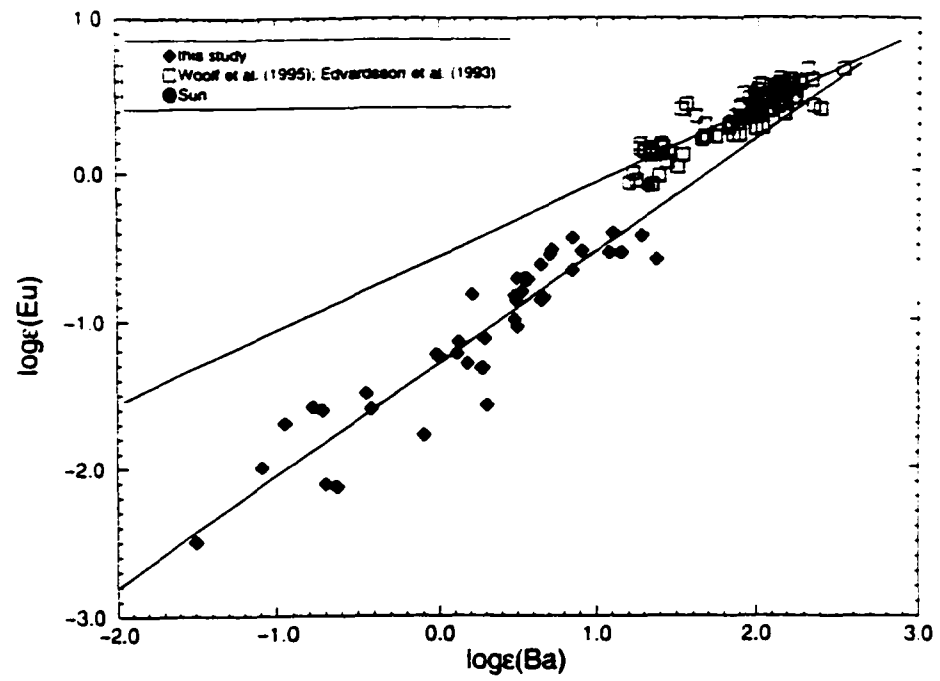
Figure 3.8 Log ϵ(Eu) versus log ϵ(Ba) for Galactic stars. The two solid lines are least-square fits to the data in this paper for the metal-poor stars and the more metal-rich star surveys of Woolf et al. (1995) and Edvardsson et al. (1993).
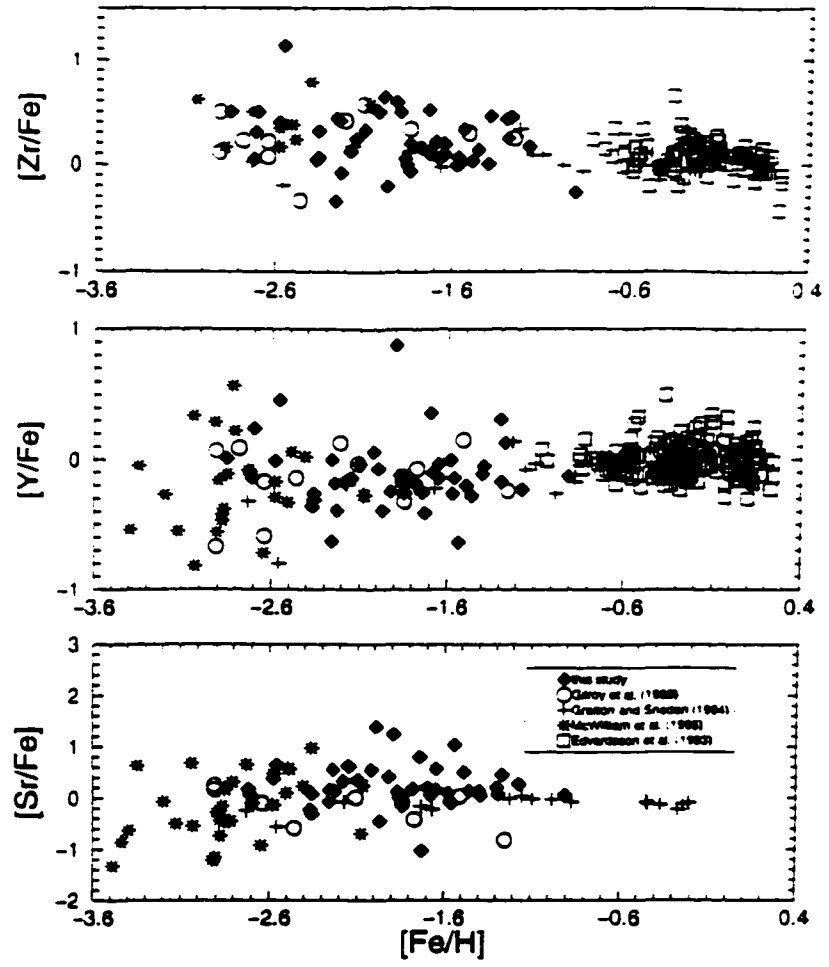
Figure 3.9 [Zr/Fe] (top panel), [Y/Fe] (middle panel) and [Sr/Fe] (lower panel) as a function of metallicity for Galactic stars.
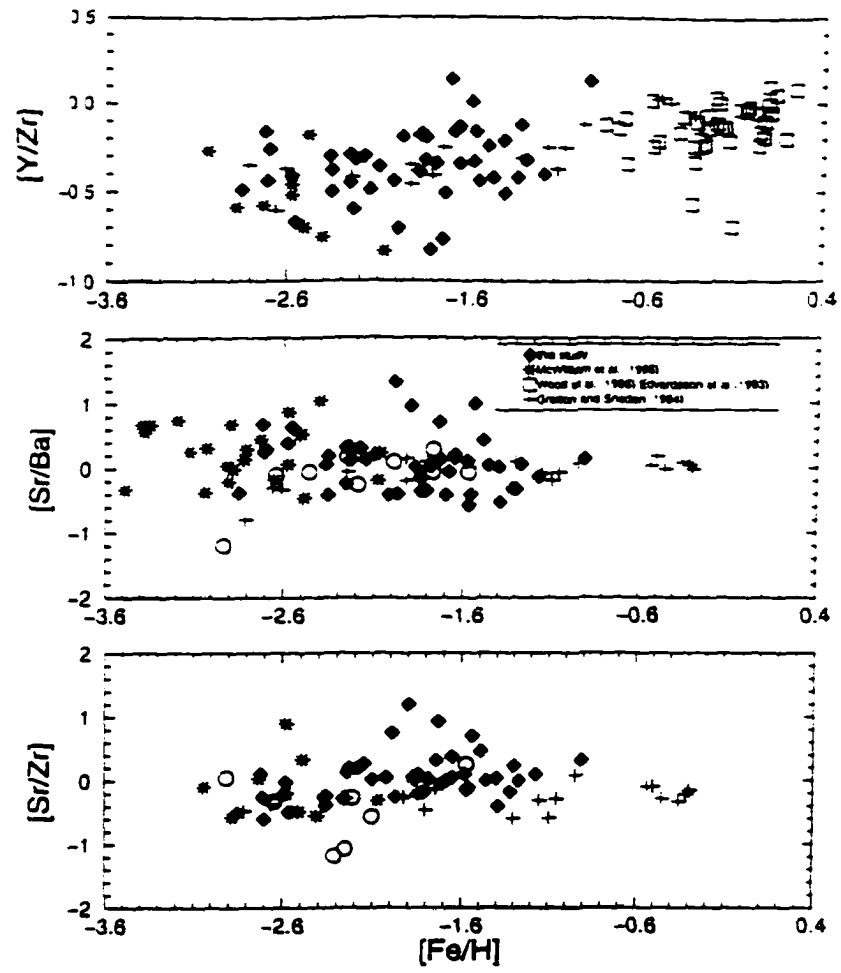
Figure 3.10 [Y/Zr] (top panel), [Sr/Ba] (middle panel) and [Sr/Zr] (lower panel) as a function of metallicity for Galactic stars.

84

Chapter IV: Hubble Time:"Up Above the World So High"

A. Introduction

The elements osmium, iridium, and platinum (Z=76-78) are produced predominantly in r-process nucleosynthesis (see Appendix I). This nuclear mass region defines one of the three major r-process peaks. In solar material, the total abundance in this r-process peak is approximately 10 times larger than the abundance of the r-process element Eu, which as seen in the previous chapters, has been measured in metal-poor stars numerous times. Also, both the r- and s-process contribute to the abundances of most of the heavy elements (Ba-Dy) that are accessible in the the visual spectral range. In contrast, Os, Ir, and Pt are nearly pure r-process in origin. Therefore, the detection of the Os-Ir-Pt r-process peak in halo stars would demonstrate unambiguously that r-process nucleosynthesis contributed to the entire very heavy element mass range in the early history of the Galaxy. In addition, the occurrence of the r-process elements all the way through platinum in the oldest (most metal-deficient) stars in our Galaxy has consequences for the Galactic age determinations based upon nucleosynthesis, as discussed in Chapter II. Since the r-process is responsible for the production of the long-lived nuclear chronometers, near the Os-Ir-Pt peak, it will be important to establish that their production occurred at time zero of the Galaxy.

Recall that in the introduction it was shown that the origin of the r-process elements had to be associated with short-lived objects (possibly SN) and that the s-process site was likely lower mass stars in late stages of stellar evolution. Lead (Z=82) is primarily an s-process element. Therefore, there should be depletions in the abundance of Pb with respect to the r-process elements in these old stars. The

dominant atomic transitions for the elements Os, Ir, and Pt are not accessible to ground-based telescopes. A couple of Pb I transitions ($\lambda\lambda4058$, 3683) exist in the near-UV, but they are weak and blended in the Sun and have never been detected in metal-poor stars. But each of these elements has several strong transitions in the 2600-3100 Å spectral region. In HST cycles 4,5, and 6 we used the Goddard High Resolution Spectrometer (GHRS) to search for strong UV transitions of third-peak elements in three very metal poor giant stars: HD 122563, HD 126238, and HD115444. The first report of the detections of osmium, platinum, and lead in HD126238 appeared in Cowan et al. (1996), with a more extensive discussion of results and comparisons of the three stars appearing in Sneden et al. (1998).

B. Observations and Reductions

We observed three very metal-poor giant stars for this program. Preliminary predictions of the UV spectra for a variety of metal-poor stars suggested that the strengths of the third n-capture peak transitions would be too weak for detection in main-sequence and subgiant stars. Our attention was then focused on choosing the best metal-poor giants to observe.

We gathered data in four near-UV spectral regions of HD 122563 and three regions for the other two stars. The spectral regions were selected to contain low-excitation transitions of third-peak species Os I, Pt I, Ir I, and Pb I. HD 122563 was chosen for HST cycle 4 observations because it is by far the brightest very metal-poor star in the sky. Recall from the introduction that this star has been observed numerous times by many authors. This star has relative underabundances of the rare earth elements (e.g., [Eu/Fe]$\simeq$-0.4; Sneden & Parthasarathy 1983; Gratton & Sneden 1994, and others.) Thus we expected very weak UV lines of the n-capture elements in this star.

During HST cycle 5, we obtained GHRS spectra in three wavelength regions of

HD 126238. This star is a magnitude fainter than HD 122563, but is more metal rich ([Fe/H]$\simeq$-1.7; Gratton & Sneden 1994). Both of these stars have been well studied with ground-based high-resolution spectra (Gilroy et al. 1988; Gratton & Sneden 1994). This star was expected to have strong UV lines for the third-peak elements. These expectations were confirmed by the GHRS spectra.

Finally, we observed three wavelength regions of HD 115444 during cycle 6. The comparisons between HD 122563 and HD 115444 were particularly insightful, since they have very similar atmospheric parameters and similar metallicity ([Fe/H]$\simeq$-2.8) but HD 115444 is much more abundant in the n-capture elements (e.g., [Eu/Fe]$\simeq$+0.4; Griffin et al. 1982; Gilroy et al. 1988). Therefore, HD 115444 is of special interest, even though it is nearly three magnitudes fainter that HD 122563, thus requiring either longer exposure time or a sacrifice of S/N in the spectra.

The spectra each spanned wavelength ranges of approximately 45 Å, and had central wavelengths near $\lambda\lambda$2830, 2915, 3060, and (only for HD 122563) 3010. The resolving power of each reduced spectrum was R$\simeq$32,000 and the S/N was between 50 and 70. We employed IRAF software for the first parts of the spectrum reductions. Using the FITS images obtained from IRAF we made final reductions using the SPECTRE spectrum analysis package (Fitzpatrick & Sneden 1987).

C. The Neutron-Capture Elements: Solar Studies and Transitions in GHRS Spectra

The UV spectra of even very metal-poor stars are complex, and line identification requires careful consideration of atomic and molecular (mainly OH) contaminants to the feature of interest. We selected n-capture species features to be observed with the aid of a variety of published line lists. General sources included: (1) the solar spectrum identifications of Moore, Minnaert, & Houtgast (1962) and Moore, Tousey, & Brown (1982); (2) the atomic and molecular line lists of Kurucz (1995a, 1995b);

(3) the ongoing NIST compilation of reliable *gf*-values. A more comprehensive list of sources is included in Sneden et al. (1998).

For baseline abundances we adopted the solar photospheric and solar system meterortic abundances recommended by Grevesse, Noels, & Sauval (1996). For the elements considered in this chapter, the Grevesse et al. (1996) abundances do not differ substantially from those found in earlier solar abundance summaries (Anders & Ebihara 1982 and others).

The search for the n-capture transitions was limited to the near-UV spectral region, defined here to be approximately the wavelength range 2700 Å$\leq \lambda \leq$ 3300 Å. The long wavelength limit was set by assuming that ground-based facilities could be used to observe longward of this wavelength. The short wavelength limit was imposed by the rapidly decreasing fluxes of cool giant stars toward smaller wavelengths. The search for the third-peak elements became limited to neutral-species transitions that both arise from low-excitation potential (E.P.) states and have large transition probabilities (log *gf*). The third-peak elements have large first ionization potential (<I.P.>$\simeq$8.5 eV, compared to <6.0 eV for the second peak elements), and therefore have substantial neutral-species populations even in giant stars. Ultimately, we identified transitions of third-peak species Os I (Z=76), Pt I (Z=78), and Pb I (Z=82); first-peak species Zr II (Z=40); and Ge I (Z=32), which is a transition elements in between the Fe group and first- peak elements. The detections of Os, Pt, and Pb in HD 126238 were the first reported detections of these elements in a Galactic halo star (Cowan et al. 1996).

C.1 *Platinum*

There are several Pt I lines in the near-UV that have favorable (E.P., log *gf*) combinations: λ2929.79 (E.P.=0.00 eV, log *gf*=0.80); λ2997.97 (0.10 eV, -0.57); λ3064.71 (0.00 eV, -0.34); and λ3301.90 (0.81 eV, -0.89). Burger & Aller (1975)

originally determined the solar platinum abundance from the latter three lines. Youssef & Khalil (1987) used updated atomic data to reconsider just the $\lambda 3301$ line. Their derived value of log ϵ(Pt)=1.74 is close to the photospheric and meteoritic values recommended by Grevesse et al. (1996) (1.8±0.3 and 1.69±0.04, respectively).

The $\lambda 3301$ Pt I line is severely blended in the Sun. Also, since it has the highest E.P. and lowest log gf among the four possible Pt I lines, it will definitely be the weakest of them in cool giant star spectra. We discarded the $\lambda 3301$ line and observed the other three lines in HD 122563. Initial attempts to match synthetic spectra with the observed $\lambda 2997.97$ line in this star showed that the blending from an OH line at $\lambda 2998.01$ was too severe to yield a useful abundance or upper limit, so this line was also discarded. We did not repeat observations of the λ 2997 line in HD 126238 and HD 115444, even though the Pt I contribution would probably have been detectable over the OH contamination in these stars.

The observed spectra of the remaining two candidate Pt I lines are shown in Figure 4.1. We emphasize that for these four figures, small downward vertical shifts have been introduced to the spectra of HD 115444 and HD 126238, in order to separate them from each other and from HD 122563 near the spectrum continuum level. Therefore, although most absorption features in HD 115444 seem to have similar depths to those of HD 122563 in these figures, they are actually weaker when the continua are normalized consistently. This is understandable since these two stars have similar but not identical atmospheric parameters: HD 115444 is somewhat hotter, has a larger gravity, and may be slightly more metal-poor than HD 122563. All of these parameter differences lead to a somewhat weaker line spectrum on average for HD 115444 compared to HD 122563.

The $\lambda 2929.79$ Pt I line (Fig. 4.1, left-hand panel) cannot be detected with any certainty in HD 122563. This statement holds in general for all third-peak

89

neutron-capture species lines in HD 122563 that will be discussed in the following sections. On the other hand, the λ2929 line is quite strong in HD 115444. The contrast in the Pt I lines strengths is made sharper by the slight weakness of most HD 115444 lines compared to those of HD122563 that we noted above. The λ2929 line also is strong in HD 126238, but so are all other feature in this stars, since it is about 10 times less metal-poor than the other two stars.

The λ3064 lines are displayed in the right-hand panel of Figure 4.1. This line should be the strongest of all Pt I lines, but unfortunately it lies in a clump of very strong atomic and OH lines. It suffers most contamination from a deep Ni I line at λ3064.62. However, the situation is not hopeless, as close inspection of the reduced spectra shows that the total Ni + Pt blend is not the same in HD 122563 and HD 115444: the latter star's feature has a redder central wavelength caused by an obvious extra absorption component in the red wing of the feature. Pt I contributes substantially to the feature strength in HD 115444 but cannot be identified with certainty in HD 122563. The extra line breadth due to two component contributions to the feature is even more obvious in HD 126238. For this blend, we applied the Gilliland et al. (1992) deconvolution algorithm to recover higher resolution spectra for the three stars, and the deconvolved spectra are the ones chosen for the right-hand panel of Figure 4.1.

C.2 Osmium

Many Os I transitions are scattered throughout the UV and visible spectral regions, allowing a reliable solar photospheric osmium abundance to be determined. The first such study was by Jacoby & Aller (1976). More recent analysis by Kwiatkowski et al. (1984) yielded $\log \epsilon = 1.45 \pm 0.10$. This has been adopted as the standard by Grevesse et al. (1996), and is in good agreement with their recommended meteoritic abundance of 1.37 ± 0.02.

Unfortunately, the (E.P., log gf) combinations of all Os I transitions longward of
$\lambda 3400$ render all solar and stellar lines of this species very weak. The only other
Os detection in a metal-poor star was the detection of Sneden et al. (1996) for
CS22892-052 which was discussed in the Chapter II. The predicted strengths of the
"long wavelength" Os I lines were vanishingly small for our program stars, so we
turned attention to the near-UV transitions.

Accurate transition probabilities of some of these lines have been determined
by Kwiatkowski et al. (1984). For other lines, the values of Corliss & Bozman
(1962) can be reliably scaled to the system defined by the lifetime measurements of
Kwiatkowski et al. (1984). Candidate Os I lines intially considered for observations
were : $\lambda 2838.63$ (E.P.=0.64 eV, log gf =+0.11); $\lambda 2909.06$ (0.00eV, -0.32); $\lambda 3058.66$
(0.00 eV, -0.43); and $\lambda 3301.58$ (0.00eV, -0.75). The $\lambda 2909$ line is unusable, since it
is masked by a strong Cr I line at $\lambda 2909.04$. The $\lambda 3301$ line is more promising, even
though it lies close to a fairly strong Ti I line at $\lambda 3301.68$. This line was used in
the solar abundance study of Kwiatkowski et al. (1984), but we did not consider
it highest priority for GHRS observations. It could be better observed in our
stars using large ground-based telescopes and good near-UV spectrograph-detector
combinations.

We obtained GHRS spectra of the remaining two Os I lines; these are shown in
Figure 4.2. For HD 115444, the S/N is highest for the "3060 Å" spectrum because
by happy accident the total GHRS exposure for this spectrum was 3 times longer
than requested. However, the lower S/N of the HD 115444 "2830 Å" spectrum
does not obscure the contrast with HD 122563: Os I lines, just like Pt I lines, are
weak-to-absent in HD 122563, but easily detectable in HD 115444. Note that the
$\lambda 3058$ line suffers some blending with an Fe I line that lies 0.05 Å redward of it.
The blending agent is undetectably weak in HD 122563 and HD 115444, but does

influence the strength of the Os I feature in HD 126238. The derived Os abundance from this line in HD 126238 should be viewed with caution.

C.3 *Zirconium*

This element lies near the first neutron-capture peak, and Zr II presents a rich spectrum of strong lines in cool stars. Biémont et al. (1981) performed an extensive laboratory study of Zr II transition probabilities, and their comparison solar abundance analysis yielded $\log\epsilon(Zr)$=2.60±0.02, which is almost exactly the meteoritic value of 2.61±0.02 from Grevesse et al. (1996). Zirconium is of special interest here because the previously cited analyses of our program stars have all reported abundances of this element. Thus, similar analyses of Zr II lines appearing on our GHRS spectra should provide reliability checks on our procedures for elements that are being studied here for the first time.

Of the possible Zr II near-UV transitions, the two most useful features proved to be those displayed in Figure 4.3; λ3054.84 (E.P.=1.01 eV, log gf =+0.18) and λ3060.11 (0.04eV, -1.37). Unlike the sharp differences in the Pt I and the Os I lines between HD 122563 and HD115444, the Zr II lines of these two stars have nearly identical strengths, suggesting that their zirconium abundances are very similar.

C.4 *Lead*

Lead is one of the heaviest stable elements and is the decay product of heavier unstable elements such as thorium and uranium. The solar photospheric lead abundance has been determined in several investigations, most recently by Youssef & Khalil (1989); see that paper for references to early studies. Their photospheric abundance, log ϵ(Pb) =2.00±0.05, is in reasonable agreement with the meteoritic value of 2.06±0.04 recommended by Grevesse et al. (1996).

The largest challenge for solar and stellar lead abundance analyses is that the

four accessible Pb I lines in the visible spectral region are weak and lie in crowded spectral regions; line-blending problems are severe. None of these Pb I lines has a favorable enough (E.P., log gf) combination to ensure detectability in metal-poor stars. Our analysis of CS22892-052 from Chapter II searched without success for the $\lambda3683.48$ (0.97 eV, -0.60) and $\lambda4057.82$ (1.32 eV, -0.20) lines in the spectrum.

Pb I has only one transition in the near-UV that predicts reasonable absorption strength from its atomic parameters: $\lambda2833.05$ (0.00 eV, -0.68). Happily, this lines lies close enough to the $\lambda2838$ Os I line that one GHRS integration could capture them both. The left panel of Figure 4.4 shows the nondetection in HD122563 and a very strong feature in HD122563. The low S/N of the HD 115444 "2830" spectrum creates some difficulty here. We believe that the absorption feature slightly redward of the expected Pb I line position is indeed that line, but we recognize that this feature is quite narrow for a stellar absorption line, and is probably afflicted by some noise spike in the blue wing. Caution is recommended in interpreting the lead abundance derived for HD 115444.

C.5 *Germanium*

An unexpected bonus was the detection of a strong Ge I line at $\lambda3039.07$ in our spectra. This feature is shown in the right panel of Figure 4.4. Note the similarity of Ge I absorption strength in HD 115444 and HD 122563. Germanium, with an atomic number Z=32, is just beyond the iron-peak element group, thus occurring well below the first neutron-capture peak. With no strong transitions in the visible spectral range, this element has been neglected in stellar abundance studies and thus in nucleosynthesis discussions.

Transitions probabilities for low-excitation Ge I lines have been determined several times (e.g., Andersen, Petkow, & Sorenson 1975; Lotrian et al. 1978 ; Tint, Kono, & Goto 1990, and others), and the gf uncertainties are small. Unfortunately,

good atomic data have not led to satisfactory photospheric/meteoritic solar abundance agreement. Grevesse et al.(1996) recommend $\log\epsilon(Ge)=3.41\pm0.14$ for the photospheric abundance and 3.63 ± 0.04 for the meteoritic value. They suspect that the 0.22 dex difference in these values is mostly the fault in the photospheric abundance. There are only two detectable Ge I lines in the visible region of the solar spectrum:$\lambda\lambda4226.57$, 4685.85. Both of these lines arise from higher excitation states (2.0eV), and suffer from intrinsically weak absorption strengths compounded by severe contamination problems from other species.

The $\lambda3039$ iine has a well-determined gf (Fuhr & Wiese 1996), and it has been included in solar abundance studies (Ross & Aller 1974). It appears to be fairly clean in our metal-poor star spectra (Fig. 4.4). Therefore, the absolute $\log\epsilon(Ge)$ abundances deduced from this line should be as reliable as those determined for other species in this study. However, relative [Ge/Fe] abundances will have larger uncertainties due to questions about the solar germanium abundance.

C.6 *Nonobserved Third-Peak Elements*

Iridium, gold, mercury, and thallium complete the third neutron-capture peak element population ($76\leq Z\leq82$). No Tl I lines in our spectral region are identified in the solar spectrum (Moore et al. 1982); they should be very weak, as the ionization potential of this species is only 6.1 eV. The resonance lines of Hg I ($\lambda2536.52$) and Au I ($\lambda\lambda2427.95$, 2675.95) might be detectable in our stars, but they lie too far in the UV to be practical possibilities for this search. Higher excitation lines of these species are predicted to be undetectable. Several Ir I lines have allowed determination of a reliable solar photospheric abundance (Youssef & Khalil 1988), which is excellent agreement with the meteoritic values recommended by Grevesse et al. (1996). Neglecting the weak higher excitation lines, there are two promising transitions of this species; $\lambda\lambda3220.78$, 2924.79. Unfortunately, the $\lambda3220$ lines at our

spectral resolution would be too blended with an Fe II line at λ3220.84 to be of use in this study. The λ2924 line was searched for on our spectra, but trial syntheses convinced us that this feature would be just a very small extra absorption in the red wing of a strong blend of Fe I and V II lines.

D. Abundance Analysis

We determined abundances of the neutron-capture elements through matching synthetic and observed spectra for the program stars. In Table 4.1 we list the stellar model atmosphere parameters and derived abundances.

The current version of the LTE lines analysis program MOOG (Sneden 1973), the same program used in Chapters II and III, was employed for the spectrum computations. Model stellar atmospheres were generated with the MARCS code (Gustafsson et al. 1975). For HD 122563 and HD115444 we used a model effective temperature T_{eff}, gravitation acceleration log g, model metallicity [M/H], and microturbulent velocity v_t from PSK96, and for HD 126238 we adopted the parameters of Gratton & Sneden (1991,1994). These are listed in the top section of Table 4.1, along with the [Fe/H] values derived in the cited studies. The atmospheric parameters served as input data for the MARCS code.

We then created an input line list for each synthetic spectrum computation. First we assembled an initial list of atomic and OH molecular lines from the Kurucz (1995a,b) compilation for a wavelength range of several angstroms centered on a n-capture feature of interest. To increase computation speed, we discarded lines from this list that contribute essentially nothing to the total line opacity in cool stars, such as multiply ionized species lines, or ones that have excitation potential in excess of 6 eV. We added a few lines that were identified in the Moore et al. (1962, 1982) solar spectrum atlases but are missing from the Kurucz compilation.

Initial synthetic spectra generated with the line lists and the model atmospheres

for our stars gave only fair matches with observed spectra. However, as previously noted (1) many n-capture species lines (and all of the third-peak ones) cannot be detected on the GHRS spectra of HD 122563 but are quite strong in HD 115444, and (2) in all other respects the spectra of HD 122563 and HD 115444 are quite similar. Taking advantage of this situation, we empirically iterated on the transition probabilities of lines in the synthetic spectrum lists until a reasonable match was made to the observed HD 122563 spectrum, and then applied those line lists to the other stars. However, a few constraints must be considered. First, the gf-values for the n-capture transitions under consideration were frozen. Second, the gf-values of individual OH lines were not altered except in rare cases in which OH lines were predicted to exist at locations where little absorption is present in the observed spectra. Instead, the strengths of all OH lines were changed together by altering the assumed oxygen abundance (assumed to be a free parameter here) in the synthetic spectrum computations. Third, for HD 122563 the intially assumed abundances of third-peak elements osmium, platinum, and lead were extrapolated from the low levels of its previously determined (see Chapter I) rare earth n-capture abundances. This assumption essentially guaranteed that the line opacities of these species would be quite small in HD 122563, and that any residual absorption observed at their wavelengths in HD 122563 could be used to set upper limits to the feature contamination from other species.

For all three program stars, synthetic spectra with the final line lists were generated for several different assumed abundances of the n-capture species, holding all other abundances constant at the values derived in previous ground-based studies. The absolute log ϵ abundance derived from each synthetic/observed spectrum match is given in the second section of Table 4.1. The upper limits quoted in the table for HD 122563 were estimated through experimental synthetic spectrum computations

in which we muted the blending agents to the n-capture species lines, leaving any observed absorption to be blamed on the n-capture lines alone. Figures 4.5 and 4.6 display samples of the synthetic/observed spectrum matches. Notice the "goodness of fit" for features other than the n-capture species features is about the same for HD 122563 and HD 115444. There are sections of observed spectra in which there are shortcomings in the synthetic spectra; for example, in Figure 4.5, there is an unidentified absorption near $\lambda 2929.2$. However, this feature appears in all three spectra, so there is some confidence in using the HD 122563 iterated line list on HD 115444. The extrapolation to HD 125238, a factor of 10 higher in metallicity, is not quite as good. For example, the synthetic spectra predict deeper features near $\lambda 2929.4$ than are actually observed and an absorption due to Co I $\lambda 3050.05$ is too strong in the synthetic spectra of HD 126238 (Fig 4.6), making it very hard to derive a zirconium abundance from the Zr II $\lambda 3060.11$ line in this star. Fortunately, such cases are rare in the features considered in this study.

Uncertainties in derived abundances due to stellar atmospheric parameters cause an error of about ± 0.10 dex. Uncertainties in the synthetic/observed spectrum matches contribute another ± 0.15 dex. The solar abundances of all but germanium appear to be well determined, and so are the transition probabilities of all lines analyzed here, and we estimate that these uncertainties add another ± 0.10 dex to the derived abundances. We estimate that, if all these error sources are taken into account, the total uncertainty in the n-capture abundances is ± 0.25 dex.

E. Discussion and Conclusions

The primary goal of this study has been to determine the abundances for some of the heaviest stable elements in very metal-poor stars. The giant star HD 126238 was reported by Cowan et al. (1996) as the first detection of the very heavy elements osmium, platinum, and lead in a metal-poor star. Further HST observations of

HD 115444 ([Fe/H]$\simeq$-2.8) indicate the presence of these same very heavy elements (Sneden et al. 1998). Observations have also been made of HD 122563, which has a metallicity similar to HD 115444. However, in contrast to HD 115444, HD 122563 has a depressed level of heavy n-capture elements (Z$\geq$ 56) and our HST observations failed to detect any of these elements in this star. The differences in third-peak abundances between these two stars were demonstrated qualitatively through the observed spectra and quantitatively by synthetic spectrum abundance computations. We further noted the strong near-UV spectral lines of HD126238, and the larger third-peak abundances consistent with that star's higher metallicity.

In this section we combine the available abundance data for n-capture elements for each star, compare these data to scaled solar system abundance distributions, and relate this information to early Galactic nucleosynthesis. The basic abundance results are given in the third section of Table 4.1. In the final section of the table, the abundances have been translated into [X/Fe] ratios, rounding the entries to the nearest 0.05 dex.

E.1. *Stellar Abundances: Comparison to Solar Element Distributions*

We consider first the very metal poor star HD 115444. We have added ground-based data (open circles) to our HST abundances (filled circles) for this star (Fig 4.7). The ground-based abundances are straight means of those reported in the two published abundance studies of this star (Griffin et al. 1982, Gilroy et al. 1988). The error bars for the ground-based abundance results were estimated from the scatter in the individual abundance estimates of these two studies. Abundances for only nine n-capture elements have been reported for HD 115444. There is pleasing agreement between the ground-based and GHRS near-UV abundances for zirconium; this suggests that our abundance scale is in reasonable accord with ground-based studies of the star.

98

We have added to Figure 4.7 scaled solar system abundance distributions for the total elemental abundances $\log\epsilon_{\odot}$ and r-process fractional abundances $\log\epsilon_{\odot}F_{\odot}[r]$. The total solar system elemental abundances are from the compilations of Anders & Ebihara (1982) and Anders & Grevesse (1989), and are indicated in this figure by a dashed line. We deconvolved the elemental abundances into r- and s-process contributions, computing the r-process fraction $F_{\odot}[r]$ for each element using the work of Käppeler et al. (1989), with the recent update of Wisshak et al. (1996). This deconvolution process is the same as used in chapters II and III. The scaled r-process curve is illustrated in Figure 4.7 by a solid line. Both of these solar curves have been displaced downward by a singe-valued additive constant, to compensate for the lower metallicites of these stars. The vertical normalization of the solar curves in Figure 4.7 was chosen to match the observed samarium (76% r-process) and europium (97% r-process) abundances. This normalization simultaneously also yields good fits to the r-process solar fractional curve of the third-peak elements osmium and platinum, and the much lighter elements yttrium and zirconium. Outliers are cerium, germanium , and zirconium. There is apparent good agreement with lead, but the stellar value is quite uncertain. While it is possible to quibble about the individual elements, the overall agreement between the solar system r-process curve and the elemental abundances of HD 115444 is very compelling. With the new HST observations of this star we have a wider range of elemental abundances (from Ge to Pt) than ever before possible.

We have made a similar abundance comparison for the well-studied halo star HD 122563. In figure 4.8 we plot (open circles) the abundances for 14 n- capture elements determined from ground-based spectra. So many abundance analyses have been published for this star that we have chosen to plot abundances that are means of those deduced by Wolffram (1972), Spite & Spite (1978), Sneden & Pilachowski

(1983), Gilroy et al. (1988), Peterson Kurucz, & Carney (1990), Gratton & Sneden (1994), and Ryan et al. (1996). Double weight was assigned to the abundances of Gratton & Sneden, since their observational data were probably the best, and they reconsidered solar abundances as well as stellar ones in their analysis.

In Figure 4.8 we also plot (filled circles) abundances or upper limits for the five n-capture elements considered in the present study. The zirconium abundance determined from GHRS near-UV data [$\log\epsilon(Zr)\simeq+0.22$] is somewhat larger than the mean of the ground-based abundances [$\log\epsilon(Zr)\simeq+0.01$], but the agreement is within the error bars. This suggests that our abundance might not have significant scale errors, at least for HD 122563. The vertical normalization was set to produce the best average agreement between the solar distributions and that of the elemental abundances of europium, gadolinium, and dysprosium in HD 122563, since these elements are nearly pure r-process in solar system material.

As has been pointed out in several of the cited papers, nearly all HD 122563 abundances in the range $56 \leq Z \leq 70$ are well fit by the scaled r- process solar system distribution. Contributions of the s-process to the observed abundances must have been quite small from the progenitor to this star. Our osmium, platinum, and lead upper limits are not inconsistent with either the scaled solar r-process or the solar total distribution. But these upper limits yield little useful information on the third n-capture peak abundances in HD 122563. A comparison of Figures 4.7 and 4.8 reemphasizes that the absolute abundance levels of elements throughout the range $56 \leq Z \leq 82$ in HD 115444 are nearly an order of magnitude greater than those in HD 122563, even though both stars have the same iron abundance.

The final abundance comparison, this time for the less metal-poor HD 126238, is shown in Figure 4.9. The ground-based data of Gratton & Sneden (1994) have been added to our HST abundances for this star. The stellar n-capture abundances in the

range $60 \leq Z \leq 82$ match well the scaled solar r-process distribution, while many of the lighter n-capture elements show evidence for some s-process contribution. In order to achieve the optimal fit to the data, a mixture of 100% r-process plus a 20% contribution of the s-process is used to match the abundance for the observed elements. The total abundance level of the n-capture elements in this star is somewhat higher than in HD 115444. However, the ratio of the third-peak element abundances to that of the pure r-process element europium is the same in both stars: $\log\epsilon = 1.35 \pm 0.1$. These new abundances, along with the ground-based data of CS22892-052 from Chapter II are quite consistent. The abundances of most n-capture elements, beginning with the rare earths and all the way out to the third-peak elements, have relative solar r-process ratios. This agreement is now seen in stars of different metallicites, with a wide range of elements running through the most massive stable elements, and with stars of very different absolute abundance levels of n-capture elements. The total n- capture element distributions for $Z \geq 55$ in these stars (and others) strongly suggest that the basic mechanism of r-process nucleosynthesis for second- and third-peak elements has not changed significantly over the history of the Galaxy, and thus, that the solar system r-process abundances for these elements could not be the average of r-process products from a number of different environments.

E.2. A Second r-Process?

The behavior of the lighter n-capture elements depicted in Figures 4.7 and 4.8 does not seem to follow the solar r-process curve as clearly as the heavier elements. We see for example that strontium and yttrium lie close to the solar r-process curve for HD 115444, but zirconium is significantly above it. In HD 122563 all three of these elements lie appreciably above the r-process solar curve, with zirconium well above the scaled total solar abundance curve. Thus, these two stars with the same

overall metallicity have very different abundance levels for both the light and heavy
n-capture elements. The critical difference is that the lighter n-capture elements
in both stars do not follow the solar r-process ratios, in contrast to those elements
above $Z = 55$. The same apparent disjunction between the light and heavy n-capture
elements is seen in the more metal-rich HD 126238, where yttrium lies on the scaled
solar r-process curve but strontium and zirconium are overabundant. These three
elements are near each other in nuclear mass, and the observed relative abundance
pattern is similar in all three stars. This would suggest that Sr-Y-Zr are produced
together in a similar environment, but the situation is unclear at this point.

We also note that newly detected germanium does not follow the scaled solar
curves in any of the three stars. This element is produced in approximately equal
amounts by the r- and s-process in solar material (See Appendix I). Thus, naively
it would be expected that the abundance of germanium in the old, metal-poor stars
would be less than total solar (with little or no s-process contribution), but would
scale with the solar r-process curve similarly to the heavier n-capture elements.
But in all three program stars, germanium has a significantly subsolar abundance.
However, germanium, like zirconium, does seem to scale with metallicity in the three
observed stars—it is identical in HD 115444 and HD126238, but significantly greater
in the higher metallicity HD 126238.

Our results appear to lend support to the suggestion that lighter n-capture
elements may be produced in a different, or second r-process (Wasserburg, Busso,
& Gallino 1996). Caution should be used however, because there are too few data
for these elements in the metal-poor stars, and other effects such as the weak
component of the s-process, expected to occur during core helium burning in massive
stars (see Chapter I for a full discussion of sites), may complicate the abundance
interpretation for the elements of germanium and the Sr-Y-Zr group. To determine

whether there are at least two different r-processes will require further examination of the abundance trends of the lighter n-capture elements, particularly those near mass number 100, just above the first r-process peak. Such observations, including those of the element Ag ($A \simeq 108$), are currently in progress (Crawford et al. 1998), but the target stars in that investigation do not include any with as low metallicites as HD 122563 or HD 115444.

E.3. *Galactic Chemical History*

Our new HST observations and abundance comparisons provide insight into the early nucleosynthetic history of the Galaxy and the nature of the first stellar generations. The three metal-poor halo stars studied here, along with the ultra-metal-poor star CS22892-052, must have been formed shortly after the beginning wave of Galactic element generation. Even though many of the n-capture elements are synthesized by a combination of the r- and s-processes in solar material, these metal-poor halo stars show mainly a scaled-down version of the solar system r-process only (for most elements $Z \geq 56$), confirming that contributions from the r-process dominated at the earliest stages of Galactic history. This result strengthens the use of chronometers, e.g., the long-lived r-process element thorium, in estimating the age of the Galactic halo (e.g., François, Spite, & Spite 1993; Sneden et al. 1996, Cowan et al. 1997).

In addition, the presence of the r-process elements in the halo stars demonstrates the existence of previous stellar generations of r-process progenitors. This follows since the r-process elements are not likely produced during quiescent stellar evolution (see Chapter I for a discussion of sites), and thus their presence in these halo stars cannot be the result of self-contamination. Supernovae are considered likely sites for the r-process although neutron-star binaries may also contribute or be a significant source. If the time lag between the formation of the Galaxy and the birth of the

present halo stars was relatively short, the halo star progenitors and sites for the r-process must have evolved quickly. These results therefore suggest the presence of a generation (or generations) of massive stars, the progenitors of Type II supernovae, early in the history of the Galaxy.

With only three stars studied here it is not possible to determine any definitive trends between halo metallicity and age. We note however that in the less metal-poor star HD 126238 there is some divergence from the r-process curve for the elements near barium (synthesized primarily via the s- process in solar system material). We suggest (Cowan et al. 1996) that this might indicate the onset of some Galactic s-processing. Figure 4.9 with the admixture of r-process and s-process seems to fit quite well. Perhaps only the more massive stellar sites for the s- process sites had time to evolve prior to the birth of HD126238. These comparisons suggest a (somewhat) longer timescale between the birth of the Galaxy and the birth of HD 126238 and the other two stars studies here; Hd 126238 might be (somewhat) younger. However, the data to support this conclusion are quite meager at this point. We further point out the well-known (and much discussed) problems associated with using the element barium in making these comparisons. Although it has been know for some time (Truran 1981) that the r-process contribution to barium could be used to study the early synthesis history of the Galaxy, this element is overwhelmingly produced in the s-process. Nevertheless, since the elements $(Z = 52)$ and xenon $(Z = 54)$, which form the second r-process peak, are not detectable at this point in halo stars, barium must be used as a tracer of both r- and s-process production for elements near the second n-capture peak. Additional calculations exploring different synthesis environments, will be needed to determine if there are multiple conditions required for the solar system r-process distribution.

TABLE 4.1. Models and Abundances

| Quantity	HD 122563	HD 115444	HD 126238
Stellar Model Atmosphere Parameters			
T_{eff} (K)	4625	4750	4975
log g	1.40	1.70	2.50
[M/H]	-3.00	-3.00	-1.65
v_t (km s^{-1})	2.0	1.6	1.5
[Fe/H]	-2.71	-2.77	-1.67
log ϵ Abundances from Individual Lines			
Ge I λ3039 Å	-0.10	-0.10	+1.15
Zr II λ3054 Å	+0.25	+0.05	...
Zr II λ3060 Å	+0.20	+0.25	...
Os I λ2838 Å	<-1.30	-0.40	+0.10
Os I λ3058 Å	<-1.30	-0.70	+0.05
Pt I λ2929 Å	<-1.30	-0.20	+0.50
Pt I λ3064 Å	<-1.20	-0.20	+0.60
Pb I λ2833 Å	<-0.80	-0.4:	0.00
log ϵ Mean Abundances			
Ge	-0.10	-0.10	+1.15
Zr	+0.22	+0.15	...
Os	<-1.30	-0.55	+0.08
Pt	<-1.20	-0.20	+0.55
Pb	<-0.80	-0.4:	0.00
[el/Fe] Mean Relative Abundances			
Ge	-0.80	-0.75	-0.60
Zr	+0.35	+0.25	...
Os	<-0.05	+0.75	+0.35
Pt	<-0.30	+0.75	+0.40
Pb	<-0.15	+0.30	-0.40
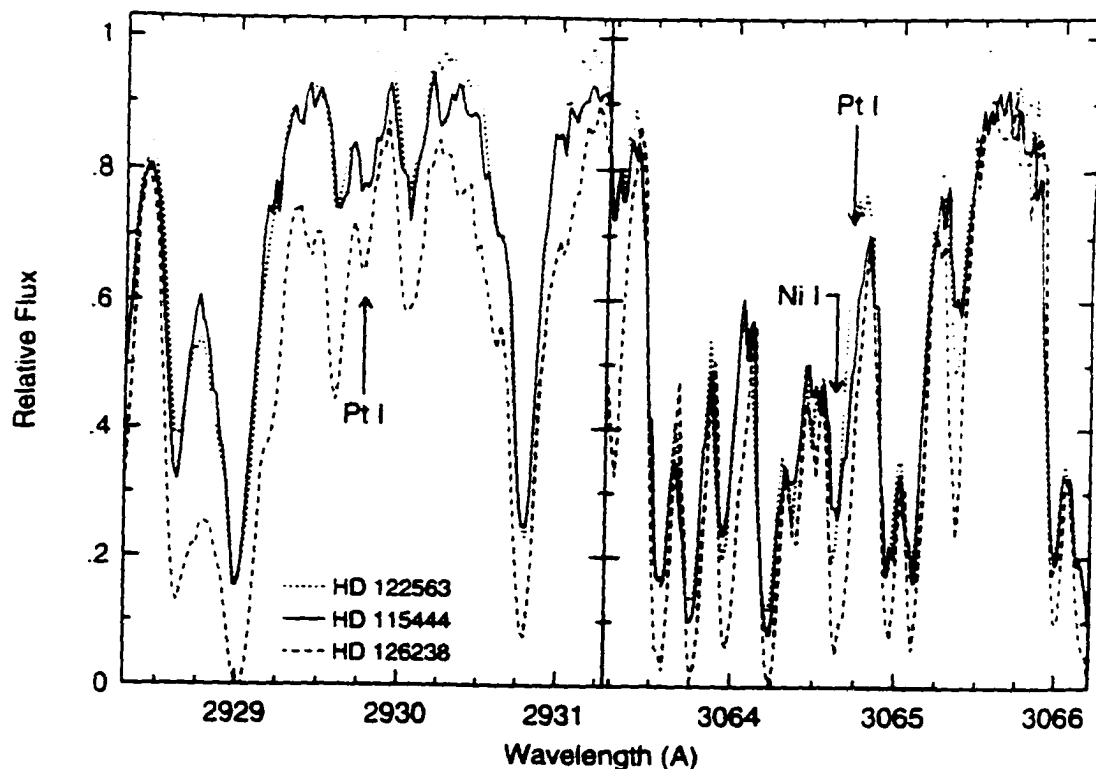
Figure 4.1 GHRS spectra of the $\lambda\lambda 2929.79,3064.71$ Å Pt I lines in HD 122563 ($[Fe/H] = -2.7$), HD 115444 ($[Fe/H] = -2.7$) and HD 126238 ($[Fe/H] = -1.7$). In Figures 4.1–4.4 the dotted lines always are used for HD 122563, solid lines for HD 115444, and dashed lines for HD 126238. All the spectra of these figures have been shifted in wavelength to align them in the rest-frame velocities of the stars. Also for display purposes, in these four figures we have shifted the spectra of HD 115444 and HD 126238 vertically downward in order to clearly separate the spectra of the three stars near their continuum regions. *In the right-hand panel of this figure only*, we show spectra that have been "de-convolved" according to the precepts of Gilliland et al. (1992) in order to increase spectra resolution and thus better uncover the $\lambda 3064.71$ Å Pt I that is heavily blended with a $\lambda 3064.62$ Å line of Ni I.

106
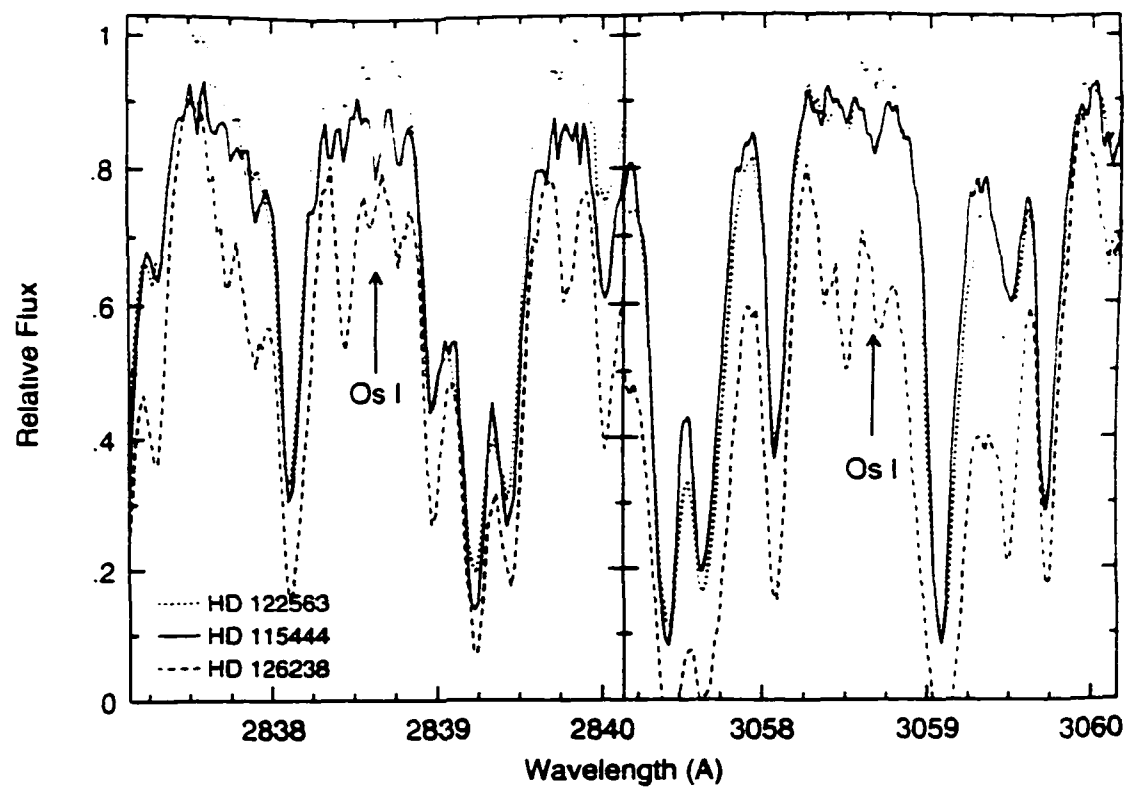
Figure 4.2 GHRS spectra of the $\lambda\lambda 2838.63, 3058.66$ Å OsI lines in the program stars. The plotting conventions are as in Figure 4.1.
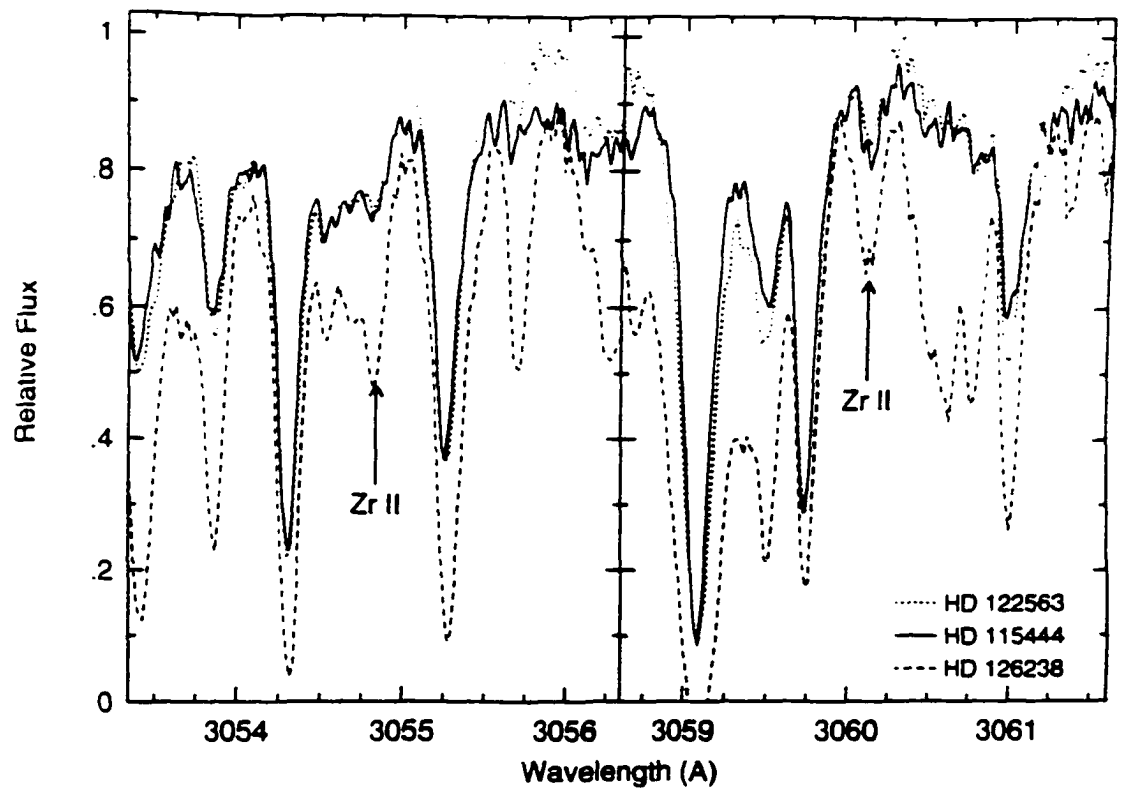
Figure 4.3 GHRS spectra of the λλ3054.84,3060.11 Å Zr II lines in the program stars. The plotting conventions are as in Figure 4.1.
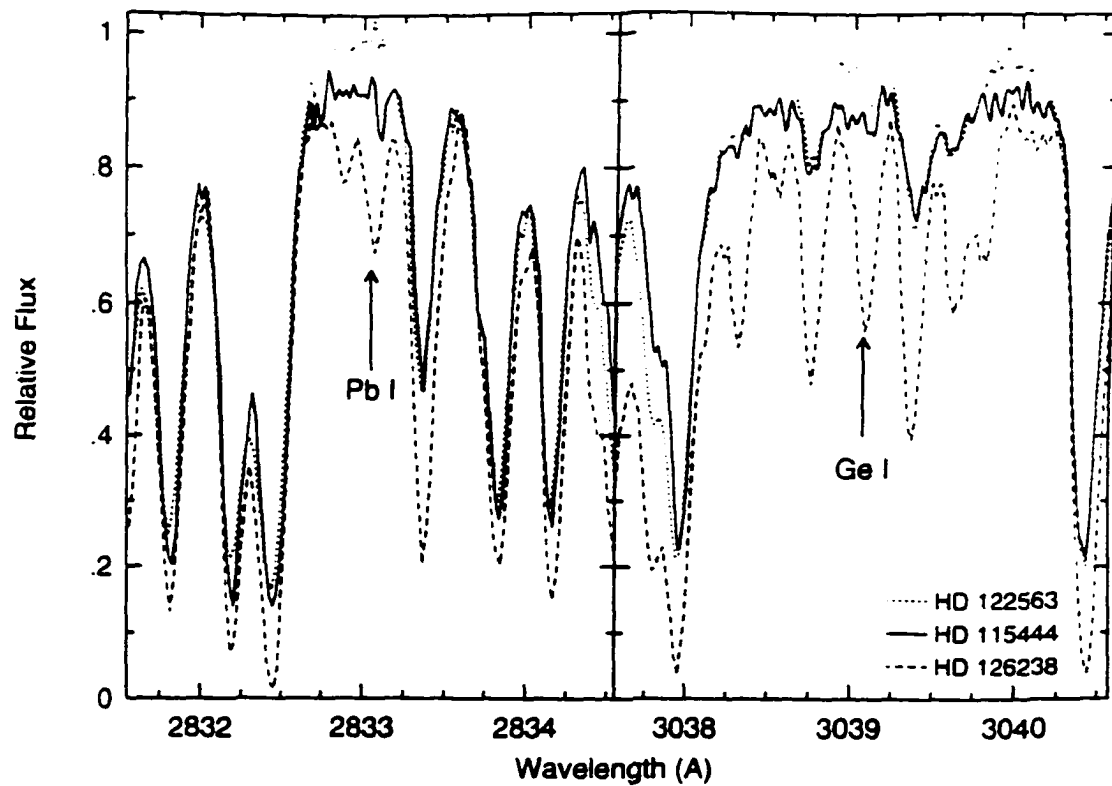
Figure 4.4 GHRS spectra of the λ2833.05 Å Pb I and λ3039.07 Å Ge I lines in the program stars. The plotting conventions are as in Figure 4.1.
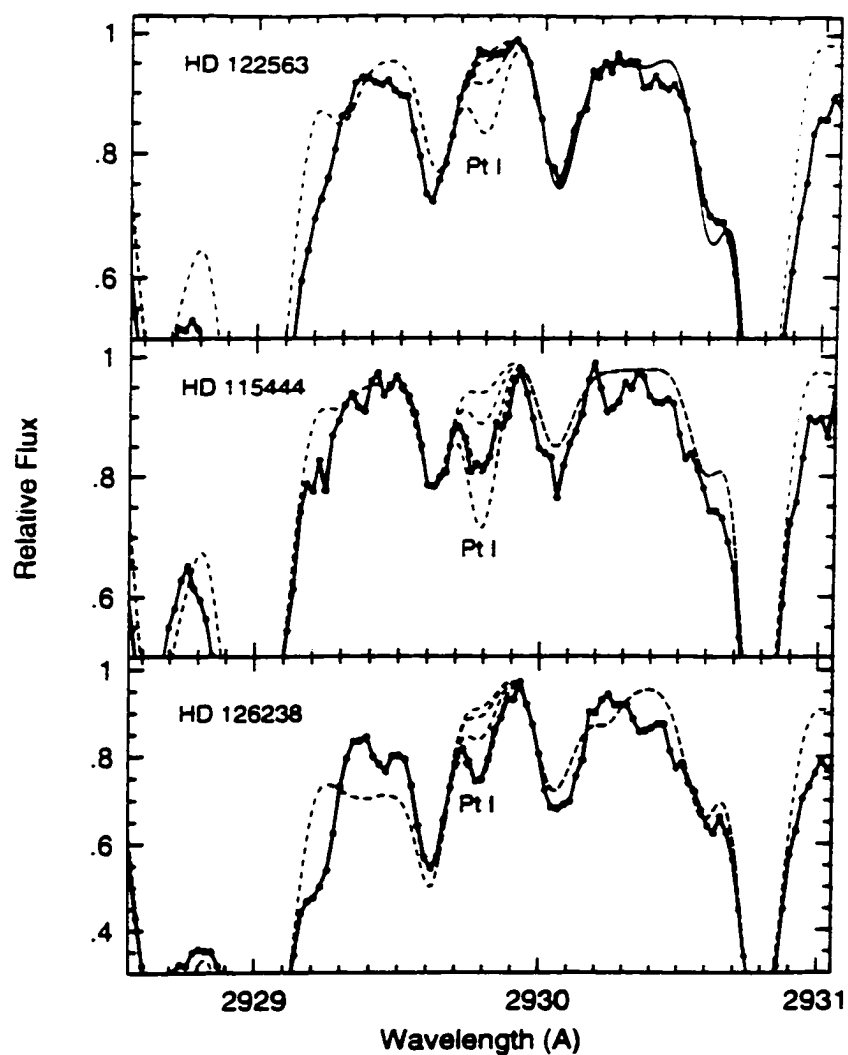
Figure 4.5 Observed spectra of the program stars (solid lines with points) compared with synthetic spectra (dashed lines) in the spectral region surrounding Pt I λ2929.8 Å. For HD 122563 (top panel), synthetic spectra have been generated for abundances log ϵ(Pt) = -1.90, -1.40, -0.90, -0.40; for HD 115444 (middle panel), log ϵ(Pt) = -1.00, -0.60 -0.20, +0.20; and for HD 126238 (bottom panel), log ϵ(Pt) = -0.85, -0.35, +0.15, +0.65.
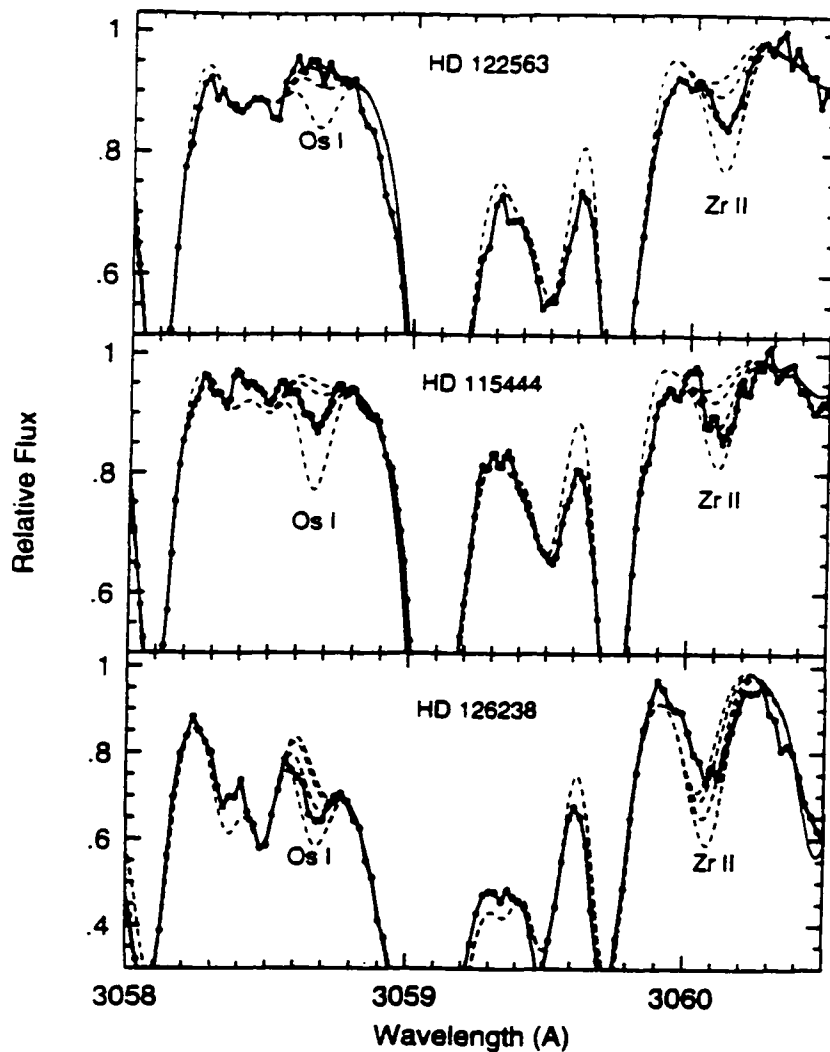
Figure 4.6 Observed spectra of the program stars (solid lines with points) compared with synthetic spectra (dashed lines) in the spectral region surrounding Os I λ3058.7Å and Zr II λ3060.1Å. For HD 122563 (top panel), synthetic spectra have been generated for abundances log ε(Os) = -2.25, -1.75, -1.25, -0.75, and log ε(Zr) = -0.40, -0.10, +0.20, +0.50; for HD 115444 (middle panel), log ε(Os) = -1.80, -1.30, -0.80, -0.30, and log ε(Zr) = -0.45, -0.15, +0.15, +0.45; for HD 126238 (bottom panel), log ε(Os) = -1.20, -0.70, -0.20, +0.30, and log ε(Zr) = +0.65, +0.95, +1.25, +1.55.
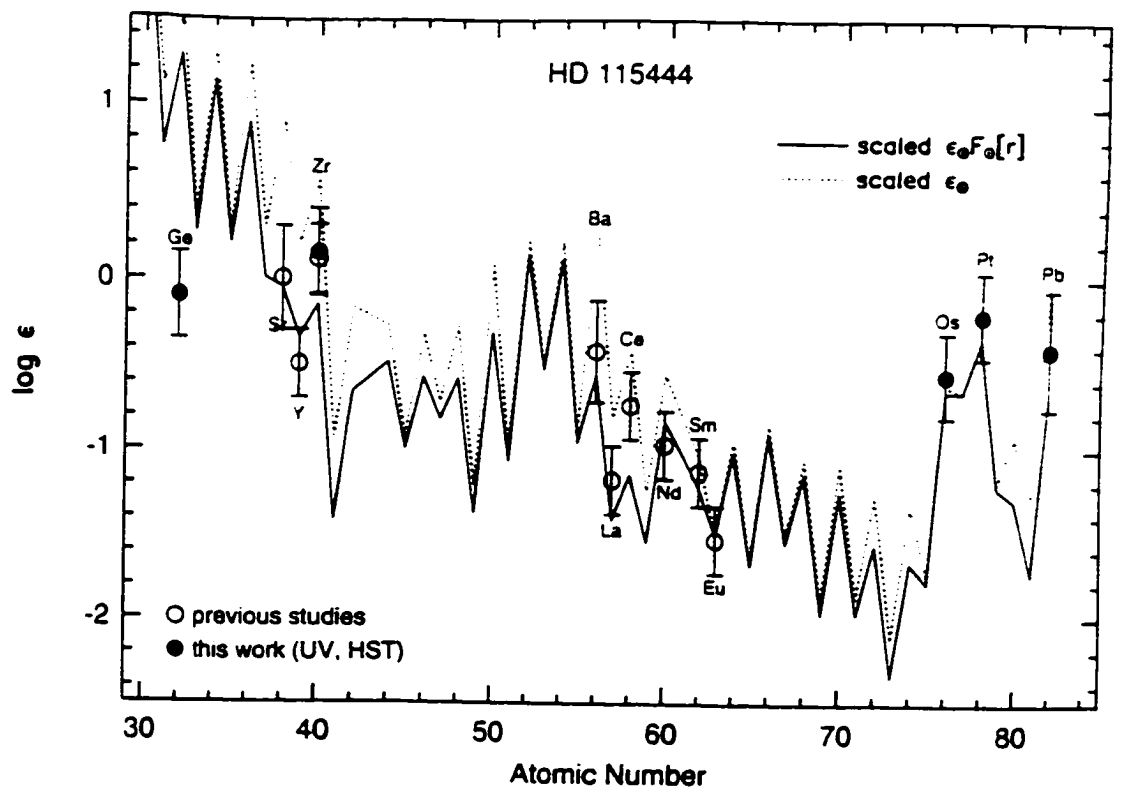
111

Figure 4.7 An abundance comparison between the neutron-capture elements in HD 115444 and a scaled total solar system (dashed line) and solar system r-process (solid line) abundance distribution. Ground-based data (from various sources, see text for discussion) is indicated by open circles, while HST data is indicated by solid circles.
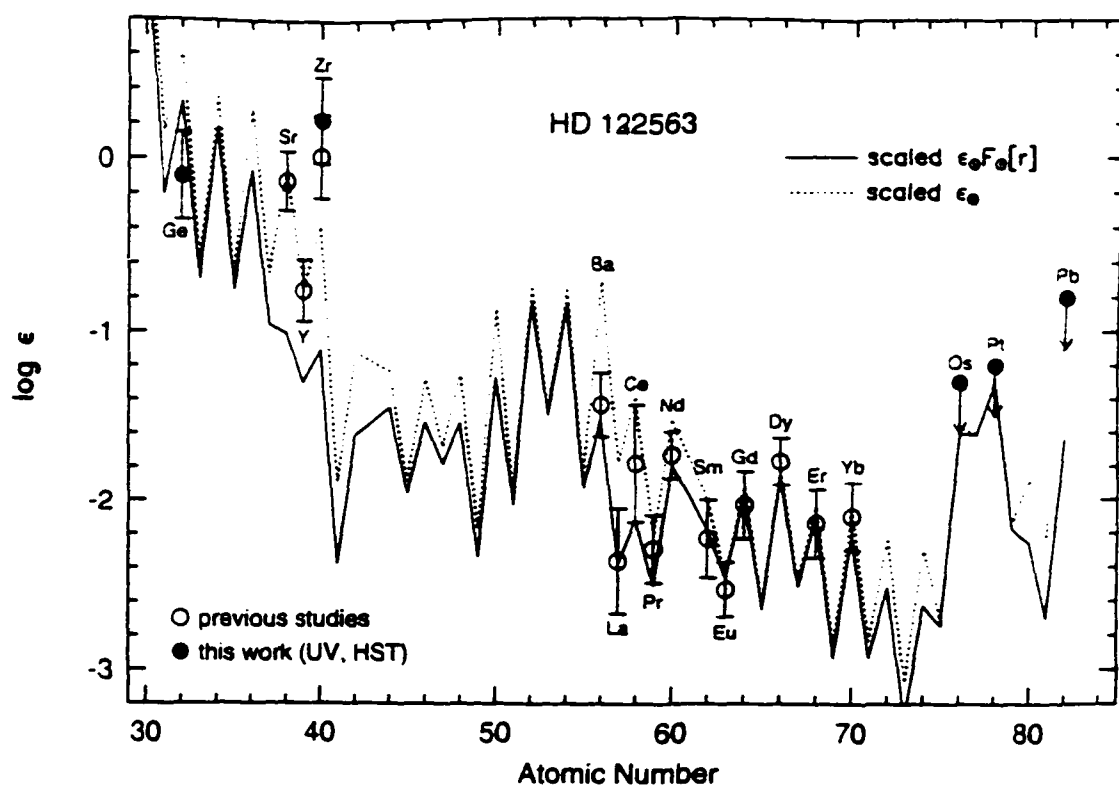
Figure 4.8 An abundance comparison for HD 122563 in the same style as that of Figure 4.7.
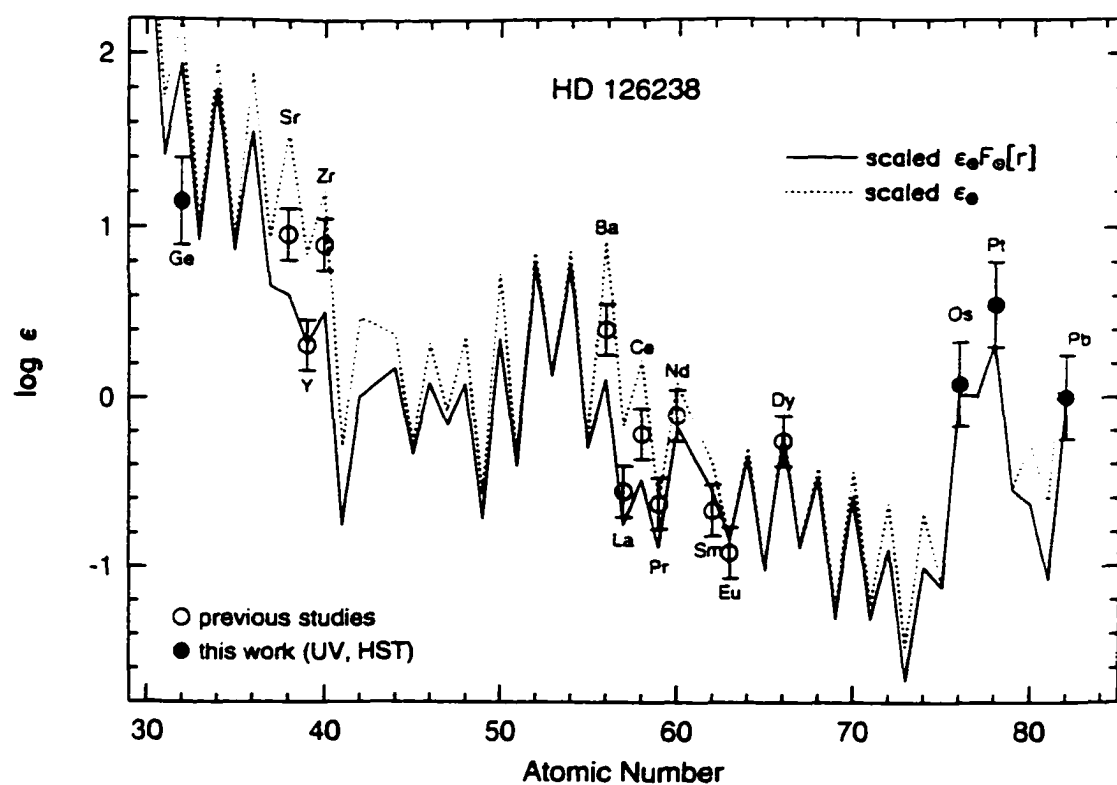
Figure 4.9 An abundance comparison for HD 126238 in the same style as that of Figure 4.7.

Chapter V: "In the End..."

"And following its path, we took no care

To rest, but climbed: he first, then I—so far,

Through a round aperture I saw appear

Some of the beautiful things that Heaven bears

Where we came forth, and once more saw the stars."

The Inferno of Dante

A. General Summary

This dissertation contains the study of a large sample of metal-poor halo stars, which are Galactic "fossils" that provide clues to the conditions and populations of stars that existed early in the Galaxy's lifetime. The chemical compositions of these halo stars come from a few, perhaps even only one, prior generations of stars. These halo stars provide an opportunity to observe n-capture elements that were synthesized in these early generations of stars. The halo stars are also an advantageous choice for observing since they are metal-poor, and therefore do not suffer as severely from contamination of the n-capture features from iron lines as more metal-rich stars do. Chapter by chapter results follow.

1. Chapter II

Chapter II demonstrated that the scaled solar-system r-process distribution could successfully match the observed n-capture abundances of the ultra-metal-poor halo star CS22892-052.

- CS22892-052 is quite old, and may contain material processed by only one previous generation of stars.

- CS22892-052 has 40 times the solar abundance of n-capture elements

- The detection of five species (Tb, Ho, Tm, Hf, and Os) never before seen in low-metallicity stars. Confirmation of the operation of the r-process over the largest number (20) of elements to date

- Scaled solar-system curve fits the n-capture elements for $Z \geq 56$.

- Presence of unmistakable signature of r-process confirms the operation of this process close to time zero in the Galaxy.

- The s-process elements (e.g., Ba) have abundances which match the r-process curve, lending support to Truran (1981) that these elements are also formed via the r-process early on in the Galaxy.

- The lighter n-capture elements' abundance distribution cannot be successfully duplicated by the s-process or the r-process distribution.

- A reasonable fit to Sr, Y, and Zr was obtained using an admixture of the r-process and the weak s-process. This implies a seemingly unphysical turnoff/turnon of the weak s/r-process at $Z = 40$.

- The detection of the actinide chronometer Th allowed age estimates for CS22892-052 to be made. Several methods were used, from a simple radioactive decay model to more complicated dynamic r-process calculations and chemical evolution models. The average age obtained via these methods is 15.2 ± 3.7 Gyr.

- This age, averaged with the age obtained by Cowan et al. (1998) for HD 115444, gives a age for the Galaxy of 13 ± 3.8 Gyr.

- The ages obtained by using the Th chronometer is in good agreement with independent age determinations from supernovae and globular clusters.

116

2. Chapter III

The trends in the abundance ratios of the n-capture elements that have been demonstrated by other authors (e.g., Gilroy et al. 1988) are confirmed with a large (46 stars) sample of metal-poor Bond giants.

- By observing the correlation of [Ba/Eu] at low metallicity, the r-process origin of both barium and europium early in the Galaxy is confirmed (Truran 1981).

- Since the relative abundances present the unmistakable signature of the solar system r-process, and the relative abundances are constant from star to star, there must be only one site for the production of the r-process. Multiple sites would present a varying superposition of abundances.

- The r-process origin of both barium and europium constrains the type of objects that were progenitors of these metal-poor halo stars. The low-mass stars that are the site of the s-process have not had time to evolve to the AGB phase before the halo stars were formed. The progenitors (massive stars?) must have short evolutionary timescales

- As metallicity increases, the trend in the [Ba/Eu] changes slope, indicating the onset of the s-process contribution to barium.

- The trend in the [r-process/Fe] ratio clearly shows the onset of iron production from Type Ia SNe. This rules out the SN Ia's as potential sites for the r-process. The Ia's are believed to come from low mass stars with long evolutionary timescales. Therefore the r-process site must have a shorter evolution time (massive stars?)

- The star-to-star scatter in the absolute abundances first pointed out by Gilroy et al. (1988) is confirmed in a larger sample.

- This scatter at low metallicity indicates that the Galactic material was not well mixed at the time of the formation of these halo stars.

- The stars with enhanced levels of n-capture elements likely formed near a region of prior nucleosynthetic activity.

- As metallicity increases, the scatter disappears, indicating the homogenization of the Galactic material.

- The abundance trends of the lighter n-capture elements indicate that they do not behave in the same manner as the r-process or s-process elements at low metallicity.

- The abundance trends of [Sr/Zr] shows that these elements do seems to come from the same source, although what that source may be is still uncertain.

- The weak s-process may be responsible for the production of these lighter elements, or their abundances trends may be evidence of a second r-process.

3. Chapter IV

The operation of the r-process over the entire n-capture mass range was demonstrate with data collected from the Hubble Space Telescope

- Three metal-poor halo stars (HD 122563, HD 126238, and HD 115444) were observed in the UV by the HST.

- Osmium, platinum, and lead were observed for the first time in these stars. These elements were previously undetected, since optimal transitions for observation lie in the UV, which is inaccessible to ground-based telescopes.

- Observations of zirconium provided a "sanity check" for abundances determined via ground-based observations.

- The abundance of lead in HD 126238 is best fit by mixture of 100% r-process and 20% s-process, indicating the more massive s-process sites have had an opportunity to evolve before the formation of HD 126238.

- Osmium and platinum are in the third r-process abundance peak. Confirming the presence of the r-process peak is important, since the nuclear chronometers uranium and thorium (both formed via the r-process) lie beyond this peak.

- Observational proof of the operation of the r-process demonstrated that uranium and thorium were formed early in the Galaxy's history. This strengthens the use of these elements in radioactive decay age estimates (as in Chapter II).

B. Where do we go now....

The n-capture elements have been studied in only a small portion of the metal-poor halo stars available for observation. Although several important trends seemed to be apparent in the surveys available, results for many more stars are needed to confirm these trends with certainty. Observations of more stars with [Fe/H]<-1.5 will provide more insight into the timescale for both the onset of the s-process and the timescale for the mixing of Galactic material.

The ultra-metal-poor regime ([Fe/H]<-3.0) has very sparse data, and there are some potentially interesting effects that could occur at very low metallicity. These stars could be some of the oldest objects in the Galaxy, perhaps part of the second generation of objects formed. Detecting the r-process in these stars would confirm, almost without a doubt, that the r-process operated at time zero in the Galaxy. These results could also constrain the type of objects that "inhabited" the young Galaxy, and provide a definite identification of the r-process site.

The problems with fitting the lighter r-process element also requires more extensive data, as well as improved nuclear data to reduce the error in abundance analysis. Ideally, observations of elements in the void between zirconium and barium should be done. Such information could test the validity of extending the r-process signature into the lighter mass region. Also, understanding the process (or processes) which are responsible for the formation of the strontium, yttrium, and zirconium could lead to the confirmation of a second r-process.

Lastly, the age of the Universe is still a hotly debated question. Using the radioactive actinide chronometer thorium, a star's age can be determined, and thus put constraints on the age of the Galaxy. This technique of age determination is independent of the methods of determining ages from the Hubble constant, thus providing a "check" for these methods. Obtaining further detections of thorium in metal-poor stars could, albeit indirectly, provide a lower limit to the age of the Universe.

REFERENCES

Anders. E.. & Ebihara, M. 1982. Geochim. Cosmochim. Acta. 46. 2363

Anders. E.. & Grevesse. N. 1989. Geochim. Cosmochim. Acta. 53. 197

Andersen. T.. Petkov. A. P.. and Sorensen, G. 1975. Phys. Scr. 12. 283

Beers. T.C.. Preston. G.W.. and Shectman .S.A.. 1985. AJ. 90. 2089

Beers. T.C.. Preston. G.W., and Shectman .S.A., 1985. AJ. 90. 2089 1992. AJ. 103
1987

Bevington. P., 1969, Data Reduction and Error Analysis for the Physical Sciences
(New York: McGraw Hill).

Biémont, E., Grevesse, N., Hannaford, P., & Lowe, R. M. 1981, ApJ. 248. 867.

Biémont, E., Roland. G.. & Delbouille, L., 1981, Sol. Phys., 71. 223.

Biémont. E.. & Lowe, R. M.. 1993 A&A, 273, 665.

Bond. H.E. 1980, Ap.J.Suppl., 44, 517

Branch, D., Fisher, A., Baron, E., &Nugent, P. 1996, ApJ, 470, L7

Burbidge, E.M., Burbidge, G.R., Fowler W.A., & Hoyle, F. 1957, *Reviews of Modern
Physics*, 29, 547.

Burger. H., & Aller, L. H. 1975, Proc. Nat. Acad. Sci. USA, 72, 4193

Burris, D. L., Pilachowski, C. A., Armandroff, T., Sneden, C., & Cowan. J. J. 1998.
in preparation

Cameron, A. G. W., 1957. Chalk River Rep. CRL-41, Atomic Energy Can. Ltd.

Cameron. A. G. W.. & Truran. J. W.. 1977. Icarus. 30. 447.

Cameron. A. G. W. 1973. Space Sci. Rev. 15. 121.

Cameron. A. G. W. 1982. Astrophysics Space Sci. 82. 123.

Corliss. C. H.. & Bozman. W. R. 1962. Experimental Transition Probabilitie s for
    Spectral Lines of Seventy Elements. NBS Monograph 32. U. S. Government.
    Washington

Cowan. J. J.. Cameron. A. G. W., & Truran. J. W.. 1982. ApJ. 252. 348.

Cowan. J. J.. Cameron. A. G. W.. & Truran, J. W., 1983. ApJ. 265. 429.

Cowan. J. J., Cameron. A. G. W., & Truran, J. W., 1985 ApJ, 294. 656.

Cowan. J.J.. Thielemann, F.-K., & Truran. J.W. 1991, Phys. Rep.. 208, 267

Cowan. J. J.. Burris. D. L., Sneden, C., McWilliam, A.. & Preston, G. W. 1995.
    ApJ. 439. L51

Cowan, J.J.. Sneden, C., Truran, J. W., & Burris, D. L. 1996, ApJ. 460, L115

Cowan, J.J.. McWilliam, A.. Sneden, C., & Burris, D. L. 1997, ApJ, 480, 246

Cowan, J. J., et al. 1998, ApJ, submitted

Crawford, J., Sneden, C.. King, J. R., Boesgaard, A. M., and Deliyannis. C. 1998. in
    preparation

Edvardsson. B., Andersen, J., Gustafsson, B., Lambert, D.L., Nissen. P.E.. &
    Tomkin.J. 1993, A&A, 274, 821

Eriksson, K., Edvardsson, B., Sneden. C., Burles, S., & Tytler, D. 1998. in
    preparation

122

Fitzpatrick. M. J.. & Sneden. C. 1987. BAAS. 19. 1129

François. P. & Gacquer. W. 1998. Nature. submitted

François. P.. Spite. M.. & Spite. F. 1993. A&A. 274. 821

François. P. & Gacquer. W. 1998. Nature. submitted

Fuhr. J. R.. & Wiese. W. L. 1996. NIST Atomic Transition Probability Tables. in CRC Handbook of Chemistry and Physics. ed. D. R. Lide. CRC Press. Boca Raton FL. 10-128

Gallino. R. et al. 1998. ApJ, 497, 388

Gilliland. R. L.. Morris. S. L., Weymann, R. J., Ebbets. D. C., & Linder. D. J. 1992. PASP. 104, 367

Gilroy. K. K.. Sneden. C.. Pilachowski. C. A.. & Cowan, J. J. 1988, ApJ, 327. 298

Gratton. R.. & Sneden. C. 1991. A&A, 241, 501

Gratton. R.. & Sneden. C. 1994, A&A, 287, 927

Grevesse. N. Noels, A.. & Sauval, A. J. 1996, in Cosmic Abundances, PASP Conf. Ser. 99. ed. S. S. Holt and G. Sonneborn, 117

Griffin, R., Griffin, R., Gustafsson, B., & Vieira, T. 1982, MNRAS, 198. 637

Gustafsson, B., Bell, R. A.. Ericksson, K., and Nordlund, A. 1975. A&A, 42. 407

Howard. J. 1998. private communication

Jacoby, G.. & Aller, L. H. 1976, Proc. Nat. Acad. Sci. USA, 73, 1382

Käppeler. F., Beer. H., & Wisshak, K. 1989, Rep. Prog. Phys.. 52, 945

Kurucz. R. L. 1995a. in Astrophysical Applications of Powerful New Databases. PASP Conf. Ser. 78. eds Adelman. S. J. & Wiese. W. L. (San Francisco. ASP). 205

Kurucz. R. L. 1995b. in Laboratory and Astronomical High Resolution Spectra. PASP Conf. Ser. 81, eds Sauval. A. J.. Blomme. R.. & Grevesse. N.. (San Francisco. ASP). 583

Kwiatkowski. M.. Zimmermann. P.. Biémont. E.. and Grevesse. N. 1984. A&A. 135. 59

Lamb. S. A.. Howard. W. M.. Truran, J. W.. & Iben. I.. 1977. ApJ. 217. 213.

Lattimer, J. M.. & Schramm, D. N., 1974, ApJ, 192, L145.

Lattimer. J. M.. & Schramm, D. N., 1976, ApJ. 210, 549.

Lotrian, J., Cariou, J., Guern, Y., and Johannin-Gilles, A. 1978. J. Phys. B: Atom. Molec. Phys., 11, 2273

Magain. P. 1995 A&A. 297, 686.

Mathews, G. J. & Cowan, J. J. 1990, Nature, 345, 491

Mathews, G. J., Bazan, G. & Cowan, J. J. 1992, ApJ, 391, 719

McWilliam, A. 1997, ARAA, 35, 503

McWilliam. A. 1998, AJ, 115, 1640

McWilliam. A.. Preston. G. W., Sneden. C., & Searle, L. 1995a. AJ. 109. 2736.

McWilliam. A., Preston, G. W., Sneden, C.. & Searle, L. 1995b. AJ. 109. 2757.

Merrill. P. W., 1952, Science, 115, 484.

Meyer. B. S. 1994. ARA&A. 32. 153

Moore. C. E.. Minnaert. M. G. J.. & Houtgast. J. 1962. "The Solar Spectrum 2935Å to 8770Å". NBS Mono. 61

Moore. C. E.. Tousey. R.. and Brown, C. R. 1982, "The Solar Spectrum 3069Å to 2095Å". NRL Rep. 8653

Morell. O.. Källader. D.. & Butcher. H. R. 1992 A&A. 259. 543.

Norris. J. E.. Peterson. R. C.. & Beers, T. C. 1993. ApJ. 415. 797.

Pagel. B. E. J. 1993. in Origin and Evolution of the Elements. ef. N. Prantzox. E. Vangioni-Flam. & M. Casse Cambridge: Cambridge University Press. 496.

Peterson, R. D.. Kurucz. R. L., and Carney, B. W. 1990, ApJ, 350, 173

Pilachowski. C. A.. Sneden, C., & Kraft. R. P. 1996. AJ, 111, 1689

Pont. F.. Mayor. M.. Turon. C.. & Vandenberg, D. A. 1998, A&A, 329. 87

Prantozos. N.. Hashimonoto, M., & Nomoto. K. 1990, A&A, 234, 211.

Pryzybylski. A. 1961. Nature, 189, 739.

Qian. Y.-Z.. Vogel. P., & Wasserburg, G. J. 1998, ApJ, 494, 285

Rateri, C. M.. Busso, M., Gallino, R., & Picchio. G. 1991 ApJ, 371, 665.

Raiteri, C. M., Gallino, R., Busso, M., Neuberger. D. & Käppeler, F. 1993. ApJ. 419. 207

Riess, A. et al. 1998, AJ, in press

Rosswog, S.. Thielemann, F.-K., Davies, M.B., Benz, W., & Piran, T., 1998. A&A. submitted

125

Ross. J. E.. & Aller, L. H. 1974. Sol. Phys.. 35. 281

Ryan. S. G.. Norris. J. E.. & Beers. T. C. 1996 ApJ. 471. 254.

Schramm. D. N. 1973. ApJ. 185. 293.

Seeger. P. A.. Fowler. W. A.. & Clayton. D. D. 1965 ApJS. 11. 121.

Sneden. C. 1973. ApJ. 184. 839

Sneden. C.. & Parthasarathy. M. 1983. ApJ. 267. 757

Sneden. C.. Preston. G. W.. McWilliam, A., & Searle. L. 1994. ApJ. 431. L27

Sneden. C.. McWilliam. A., Preston, G. W., Cowan. J. J.. Burris. D. L.. & Armosky.
B. J. 1996. ApJ. 467, 819

Sneden. C.. Cowan. J. J.. Burris, D. L., & Truran. J. W. 1998. ApJ. 496. 235.

Spite. M.. & Spite, F. 1978, A&A, 67. 23.

Symbalisty. E. M. D., & Schramm, D. N. 1982 ApJ, 22, 143.

Thielemann, F.-K., & Benz, W. 1998 to appear in Proceedings of Ringberg Castle
Conference.

Tint, K., Kono, A., and Goto, T. 1990, J. Quant. Spec. Rad. Trans.. 43. 427

Truran, J. W. 1981, A&A, 97, 391

Truran. J. W., & Iben, I., Jr. 1977 ApJ216, 797.

Truan. J. W., Cowan, J. J., & Cameron, A. G. W. 1978, ApJ, 222. 63.

Wasserburg, G.J., Busso, M. & Gallino, R. 1996, ApJ, 466, L109

Wisshak. K.. Voss. F.. & Käppeler. F. 1996. in Proceedings of the 8th Workshop on
    Nuclear Astrophysics. ed. W. Hillebrandt. & E. Müller (Munich: MPI). 16

Wolffram. W. 1972. A&A. 17. 17

Woolf. V.M.. Tomkin. J.. & Lambert D.L. 1995. ApJ. 453. 660

Woosley. S. E.. Wilson. J. R.. Mathews. G. J.. Hoffman. R. D.. & Meyer. B. S. 1994.
    ApJ. 433. 229

Youssef. N. H. & Khalil. N. M. 1987. A&A. 186, 333

Youssef. N. H. & Khalil. N. M. 1988, A&A. 203, 378

Youssef. N. H. & Khalil. N. M. 1989, A&A, 208, 271

Appendix I Generating the Solar System Curves

A. Introduction

The s- and r-process fractions for each element were recalculated, beginning with the solar system isotopic abundances adopted by Kappeler et al. (1989) and their neutron capture cross section measurement for each isotope, then separating out the individual s- and r-process contributions to each isotope, and finally summing over all the isotopes for each process. It is worth noting that only stable (or quasi-stable in the case of Th and U) isotopes are consider for these processes. The isotopes which contribute to the final abundance are given in Table A.1.1. The numbers in italics are the updated abundances from Wisshak et al. (1996). In table A.1.2, the r- and s-process elemental abundances are listed in columns (3) and (4). Column (5) lists the total solar system abundance which is simply a sum of (3) and (4). Columns (6) and (7) indicate the percentages for the two processes. The new work of Wisshak et al. (1996) is included where appropriate. These numbers appear under the relevent elements in italics. The plots of the total solar system abundances and the r-process and s-process fractions are presented in Figures 1.1 and 1.2 of Chapter I.

B. Error Analysis

The r-process abundances are actually residual fractions that remain after calculated s-process abundance distributions are subtracted from the solar elemental abundances. There are multiple uncertainty sources exist for the solar abundances employed in calculating the curves. To determine the uncertainty in the calculted solar system r-process fractions, the following procedure was used. I adopted the quoted errors in the meteoritic data for the elemental abundances from Anders

& Grevesse (1989). Next, I used the errors for individual isotopic s-process cross section measurements from Table 4 of Kappeler et al. (1989). Then, for each stable isotope that contributes to the elemental abundance, the totla isotopic abundance uncertainty, resulting from uncertainties in both individual cross sections and meteoritic abundances, was calculated using standard error techniques for uncorrelated errors as found in Bevington (1969). The total elemental abundance uncertainty (as a percentage) was arrived at by weighting the isotopic uncertainties according to their contribution to the total elemental makeup. Finally, this percentage was translated for each element into an uncertainty in log ϵ. These solar r-process abundance uncertainties for elements $56 \leq Z \leq 90$ are fairly uniform: $\delta(\log \epsilon) = 0.04 \pm 0.02$. Table A.1.3 contains calculated uncertainties for each element. They are certainly smaller than the CS22892-052 abundance uncertainties but should not be totally neglected in the solar-stellar comparison.

Table A.1.1
Isotopic Contributions to Elemental Abundances

Element	Isotope No.	Pct of Total	Ns	Nr
Zn				
	64	48.60	36.75	0.00
	66	27.90	37.62	265.00
	67	4.10	17.62	34.00
	68	18.80	39.09	145.00
	70	0.60	0.0	7.31
Ga				
	69	60.108	11.14	11.60
	71	39.89	10.40	4.70
Ge				
	70	21.23	15.00	0.0
	72	27.66	18.30	14.00
	73	7.73	3.53	5.67
	74	35.94	15.7	27.3
	76	7.44	0.0	9.20
As				
	75	100.00	1.46	5.33
Se				
	76	9.36	4.66	0.00
	77	7.63	1.68	3.04
	78	23.78	7.40	7.21
	80	49.61	7.45	24.30
	82	8.73	0.00	5.71
Br				
	79	50.69	0.45	0.00
	81	49.31	0.48	4.64
Kr				
	80	2.25	1.02	0.00
	82	11.6	6.21	0.00
	83	11.5	1.99	3.75
	84	57.0	10.58	18.00
	86	17.3	9.48	0.93
Rb				
	85	72.165	0.69	2.79
	87	27.835	2.21	0.10
Sr				
	86	9.86	2.11	0.00
	87	7.00	1.44	0.00
	88	82.58	16.99	2.55
Y				
	89	100.00	3.34	1.31
Zr				
	90	51.45	4.53	0.99
	91	11.22	1.16	0.04
	92	17.15	1.29	0.54
	94	17.38	1.68	0.17
	96	2.80	0.00	0.30
Nb				
	93	100.00	0.23	0.11

130

NOTE TO USERS

Page(s) not included in the original manuscript are unavailable from the author or university. The manuscript was microfilmed as received.

UMI

Element	Isotope No.	Pct of Total	N_s	N_r
Sb				
	121	57.36	0.047	0.155
				0.113
	123	42.64	0.00	0.150
				0.132
Te				
	122	2.603	0.117	0.00
			0.133	
	123	0.908	0.042	0.00
			0.047	
	124	4.816	0.208	0.00
			0.248	
	125	7.139	0.075	0.269
			0.088	0.267
	126	18.95	0.400	0.518
			0.45	0.525
	128	31.69	0.00	1.560
				1.526
	130	33.80	0.00	1.690
				1.634
I				
	127	100.00	0.050	0.850
				0.851
Xe				
	128	1.91	0.126	0.00
	129	26.4	0.066	1.314
				1.240
	130	4.1	0.199	0.00
	131	21.2	0.087	0.995
				0.954
	132	26.9	0.498	0.829
				0.800
	134	10.4	0.00	0.482
				0.449
	136	8.9	0.00	0.0391
				0.373
Cs				
	133	100.00	0.056	0.316
				0.315
Ba				
	134	2.417	0.125	0.00
			0.178	
	135	6.592	0.385	0.242
			0.068	0.298
	136	7.854	0.465	0.00
			0.500	
	137	11.23	0.439	0.074
			0.373	0.283
	138	71.70	3.545	0.29
				0.225
La				
	139	99.9098	0.336	0.111
				0.110

132

Element	Isotope No.	Pct of Total	N_g	N_r
Ce				
	140	88.48	0.894	0.131
				0.039
	142	11.08	0.00	0.129
				0.115
Pr				
	141	100.00	0.079	0.095
				0.082
Nd				
	142	27.13	0.193	0.00
			0.300	
	143	12.18	0.036	0.0647
			0.041	*0.065*
	144	23.80	0.078	0.121
			0.122	*0.089*
	145	8.30	0.017	0.0521
			0.023	*0.049*
	146	17.19	0.0523	0.092
			0.104	*0.052*
	148	5.76	0.00	0.0477
				0.044
	150	5.64	0.00	0.0468
				0.047
Sm				
	147	15.00	0.0024	0.0331
			0.0029	*0.031*
	148	11.3	0.031	0.00
			0.038	
	149	13.8	0.0056	0.0316
			0.0056	*0.031*
	150	7.4	0.018	0.00
			0.023	
	152	26.7	0.018	0.0523
			0.018	*0.053*
	154	22.7	0.00	0.0605
				0.059
Eu				
	151	47.8	0.0001	0.0426
	153	52.2	0.0024	0.0481
Gd				
	152	0.20	0.0005	0.00
			0.00049	
	154	2.18	0.006	0.00
			0.0087	
	155	14.80	0.003	0.0462
			0.0034	*0.045*
	156	20.47	0.012	0.0559
			0.015	*0.055*
	157	15.65	0.005	0.0469
			0.0065	*0.046*
	158	24.84	0.036	0.046
			0.027	*0.058*
	160	21.86	0.00	0.0722
				0.072

Element	Isotope No.	Pct of Total	Ns	Nr
Tb				
	159	100.00	0.004	0.0546
				0.060
Dy				
	160	2.34	0.0093	0.00
	161	18.9	0.0036	0.0746
				0.075
	162	25.5	0.016	0.0888
				0.101
	163	24.9	0.0023	0.0982
				0.093
	164	28.2	0.0182	0.0977
				0.091
Ho				
	165	100.00	0.006	0.0818
				0.083
Er				
	164	1.61	0.018	0.00
	166	33.6	0.0123	0.0722
				0.072
	167	22.95	0.0048	0.0530
				0.053
	168	26.80	0.0203	0.0483
				0.047
	170	14.90	0.007	0.0376
				0.037
Tm				
	169	100.00	0.006	0.0320
				0.031
Yb				
	170	3.05	0.006	0.00
	171	14.3	0.004	0.0292
	172	21.9	0.018	0.0356
	173	16.12	0.008	0.0311
	174	31.80	0.040	0.0367
	176	12.70	0.00	0.0300
Lu				
	175	97.41	0.006	0.0309
	176	2.59	0.002	0.00
Hf				
	176	5.206	0.008	0.00
	177	18.60	0.005	0.0241
	178	27.30	0.021	0.0215
	179	13.63	0.007	0.0146
	180	35.10	0.035	0.0197
Ta				
	181	99.998	0.009	0.0133
W				
	182	26.30	0.024	0.0116
	183	14.30	0.013	0.0067
	184	30.67	0.029	0.0128
	186	28.60	0.008	0.0314
	193	62.7	0.00	0.4084

Element	Isotope No.	Pct of Total	Ns	Nr
Re		.	.	.
	185	37.40	0.004	0.0141
	187	62.60	0.00	0.0333
Os		.	.	.
	186	1.58	0.012	0.00
	187	1.6	0.006	0.00
	188	13.3	0.016	0.0793
	189	16.1	0.004	0.1108
	190	26.4	0.021	0.1676
	192	41.0	0.00	0.2929
Ir		.	.	.
	191	37.3	0.005	0.2413
	193	62.7	0.00	0.4084
Pt		.	.	.
	192	0.79	0.009	0.00
	194	32.9	0.020	0.4312
	195	33.8	0.006	0.4572
	196	25.3	0.035	0.3123
	198	7.2	0.00	0.0986
Au		.	.	.
	197	100.00	0.010	0.1756
Hg		.	.	.
	198	9.97	0.035	0.00
	199	16.87	0.016	0.0434
	200	23.10	0.051	0.0298
	201	13.18	0.020	0.0265
	202	29.86	0.079	0.0256
	204	6.87	0.00	0.0204
Tl		.	.	.
	203	29.524	0.042	0.0115
	205	70.476	0.060	0.0412
Pb		.	.	.
	204	1.4	0.057	0.00
	206	24.1	0.0326	0.2233
	207	22.1	0.313	0.2800
	208	52.4	1.587	0.1184
Bi		.	.	.
	209	100.0	0.051	0.093
Th		.	.	.
	232	100.0	0.00	0.045
U		.	.	.
	235	0.7200	0.00	0.0064
	238	99.2745	0.00	0.0203

TABLE A.1.2. Solar System Abundance Fractions

Element	Z	V_s	V_r	V_{total}	s-fraction	r-fraction
Zn	30	451.81	231.08	682.89	6616	3384
Ga	31	16.3	21.5	37.8	4312	5688
Ge	32	56.17	52.53	108.7	5167	4833
As	33	5.33	1.46	6.79	7850	2150
Se	34	40.26	21.19	61.45	6552	3448
Br	35	4.64	0.929	5.569	8300	1700
Kr	36	22.68	29.27	51.95	4365	5635
Rb	37	2.89	2.903	5.793	4989	5011
Sr	38	2.55	20.54	23.09	1104	8896
Y	39	1.31	3.34	4.65	2820	7180
Zr	40	2.04	8.66	10.7	1906	8094
Nb	41	0.11	0.229	0.339	3245	6755
Mo	42	0.635	1.334	1.969	3225	6775
Ru	44	0.941	0.602	1.543	6099	3901
Rh	45	0.289	0.055	0.344	8401	1599
Pd	46	0.771	0.617	1.388	5555	4445
Ag	47	0.435	0.116	0.551	7895	2105
Cd	48	0.769	0.765	1.534	5013	4987
In	49	0.119	0.057	0.176	6761	3239
Sn	50	1.414	2.182	3.596	3932	6068
Sb	51	0.245	0.047	0.292	7154	2846
Te	52	3.952	0.976	4.919	8033	1966
I	53	0.85	0.05	0.9	9444	0556
Xe	54	3.816	0.976	4.792	7963	2037
Cs	55	0.315	0.056	0.371	8490	1509
Ba	56	0.806	4.6637	5.469	1474	8526
La	57	0.111	0.336	0.447	2483	7517
Ce	58	0.204	0.894	1.098	1858	8142
Pr	59	0.082	0.078	0.160	5125	4875
Nd	60	0.4243	0.37758	0.8019	5291	4709
Sm	62	0.1740	0.0899	0.2639	6593	3407
Eu	63	0.0907	0.0025	0.0932	9732	0268
Gd	64	0.276	0.0612	0.3302	8184	1815
Tb	65	0.060	0.004	0.0640	9375	0625
Dy	66	0.360	0.0495	0.4095	8791	1209
Ho	67	0.0813	0.008	0.0890	9325	0674
Er	68	0.2090	0.0412	0.2502	8353	1647
Tm	69	0.0310	0.006	0.0370	8378	1621
Yb	70	0.1626	0.076	0.2386	6815	3185
Lu	71	0.0309	0.008	0.0389	7943	2057
Hf	72	0.0799	0.076	0.1559	5125	4875
Ta	73	0.0133	0.009	0.0223	5964	4036
W	74	0.625	0.074	0.1365	4579	5421
Re	75	0.0474	0.00454	0.05194	9126	0874
Os	76	0.6506	0.059	0.7096	9169	0831
Ir	77	0.6497	0.005	0.6547	9924	0076
Pt	78	1.2993	0.06389	1.3693	9489	0511
Au	79	0.1756	0.0102	0.1858	9461	0539
Hg	80	0.1457	0.201	0.3467	4202	5798
Tl	81	0.0527	0.102	0.1547	3407	6593
Pb	82	0.6217	2.316	2.9381	2110	7880
Bi	83	0.093	0.051	0.144	6458	3542
Th	90	0.042	0.0	0.042	1.000	0.000
U	92	0.02383	0.0	0.02383	1.000	0.00

136

TABLE A.1.3. Error in Solar System r-process Abundances

Element	Z	σ
Ba	56	15
La	57	13
Ce	58	02
Pr	59	5
Nd	60	5
Sm	62	03
Eu	63	03
Gd	64	04
Tb	65	03
Dy	66	03
Ho	67	02
Er	68	04
Tm	69	02
Yb	70	03
Lu	71	02
Hf	72	02
Ta	73	03
W	74	03
Re	75	06
Os	76	04
Ir	77	03
Pt	78	05
Au	79	06
Hg	80	06
Tl	81	05
Pb	82	05
Th	90	03

Appendix II: Examples of Spectral Syntheses

The following figures contain examples of spectral syntheses produced by the MOOG code for the lines $\lambda4123$ (La II), $\lambda4161$ (Zr II), $\lambda4205$ (Eu II), and $\lambda4215$ (Sr II). The observations are represented by the dots, while the synthetic spectra are represented by the lines. The figure caption includes the star name, effective temperature, surface gravity, metallicity, and microturbulent velocity, respectively.
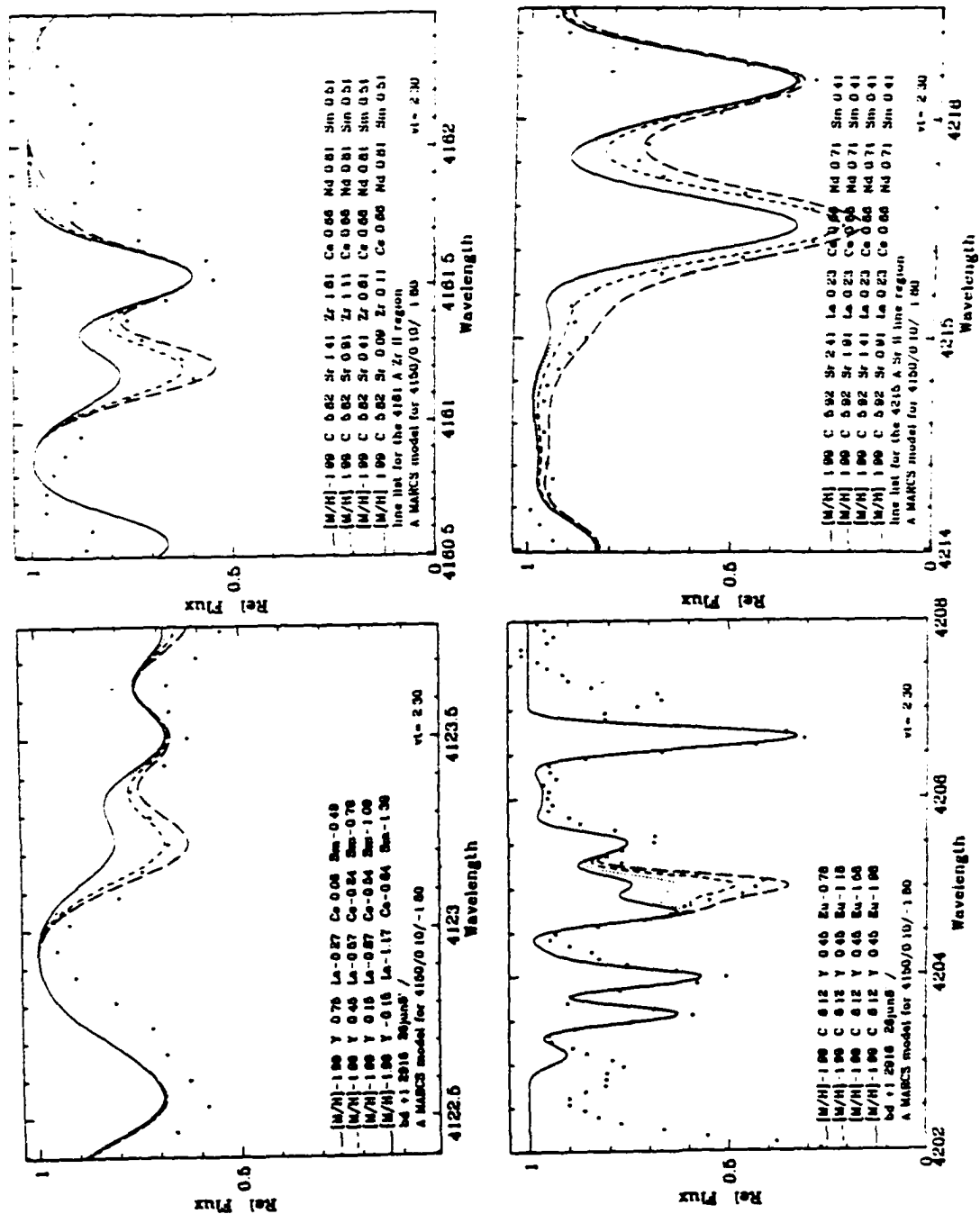
Figure A.2.1 Spectral syntheses for B+012916 (4150/0.10/-1.99/2.30)

139

Figure A.2.2 Spectral syntheses for B+060648 (4500/1.10/-2.10/2.00)

140

Figure A.2.3 Spectral syntheses for B+092870 (4600/1.40/-2.37/1.50)

141
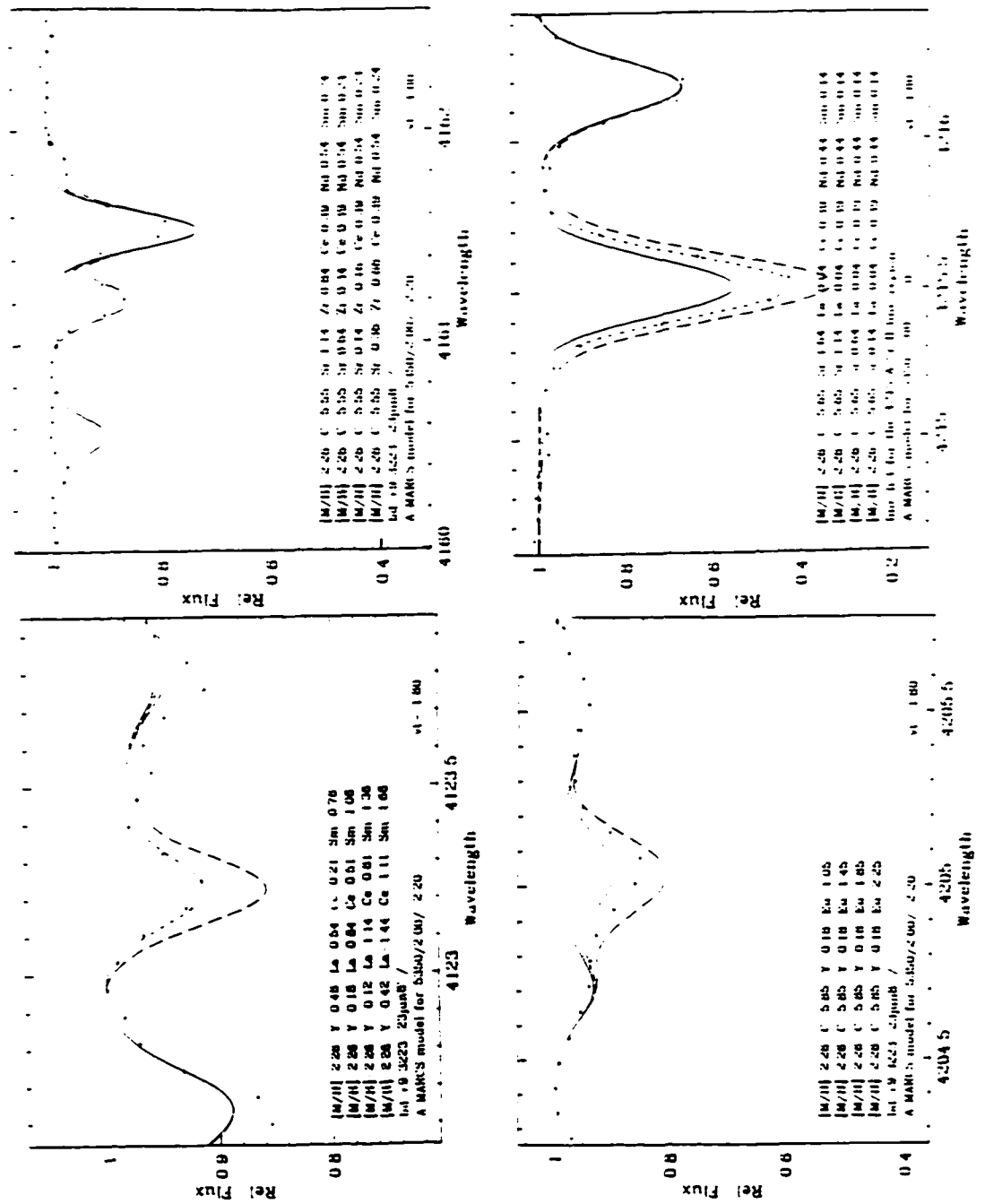
Figure A.2.4 Spectral syntheses for B+093223 (5350/2.00/-2.26/2.00)
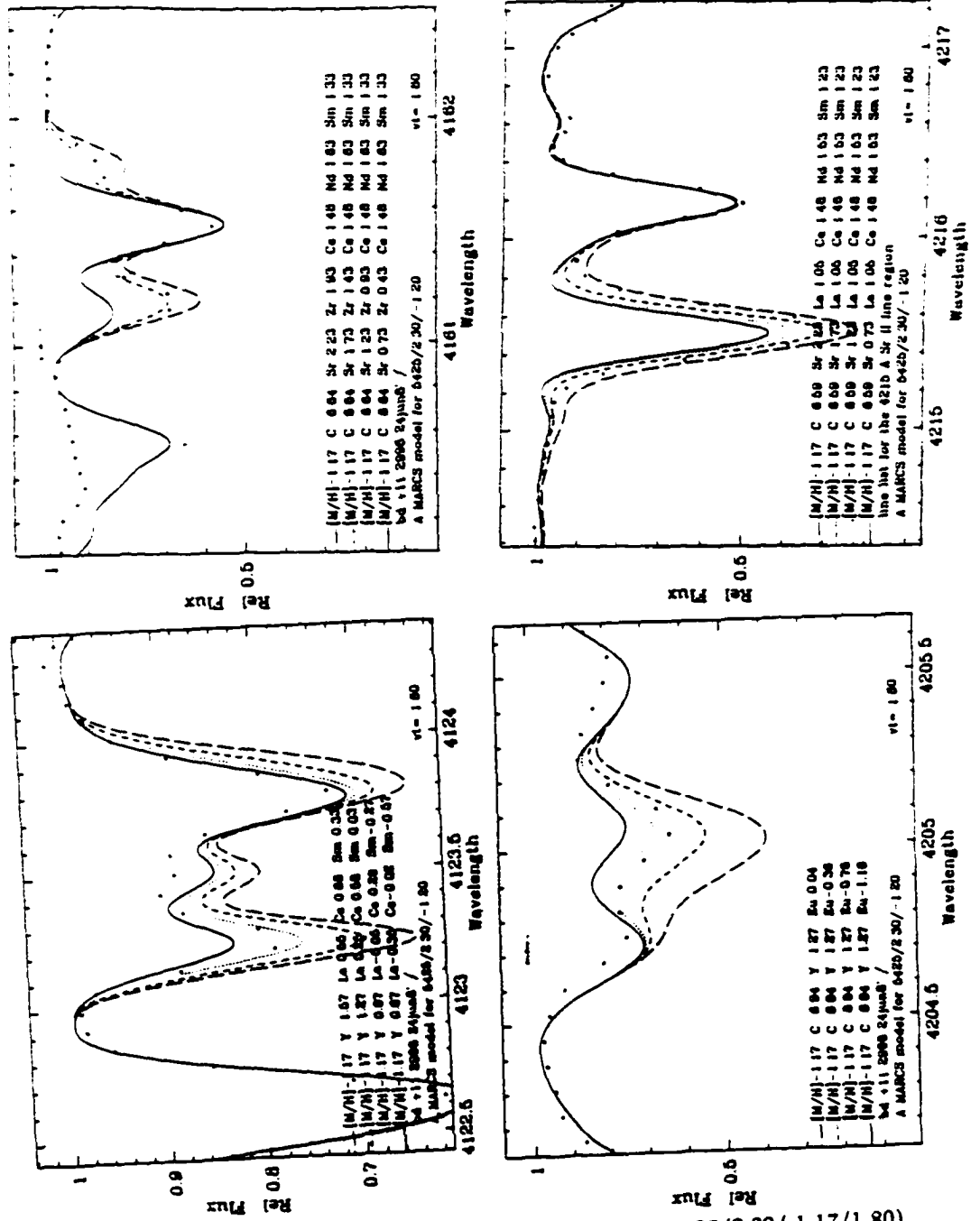
Figure A.2.5 Spectral syntheses for B+112998 (5425/2.30/-1.17/1.80)

Figure A.2.6 Spectral syntheses for B+173248 (5250/2.30/-2.02/1.50)

144
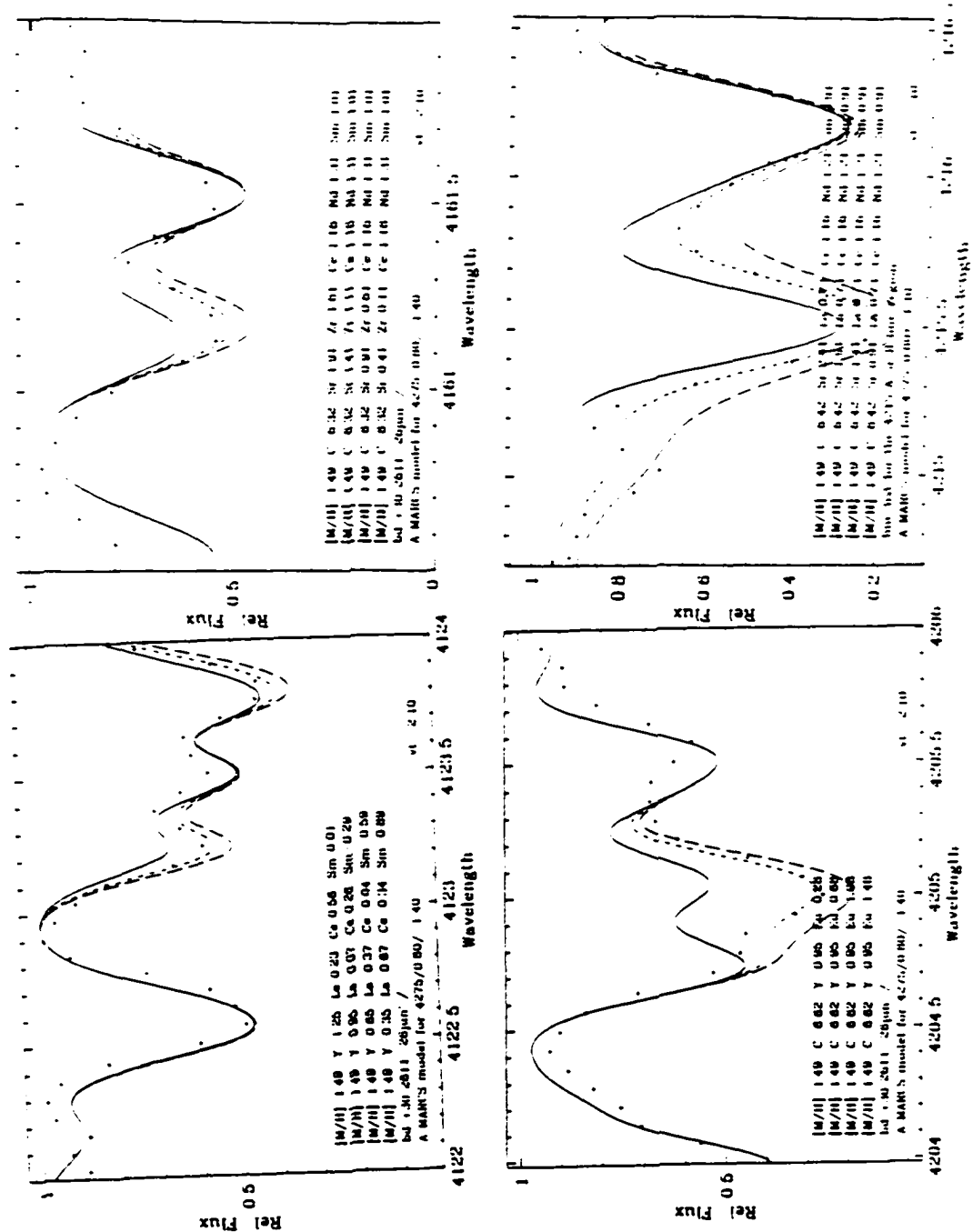
Figure A.2.7 Spectral syntheses for B+302611 (4275/0.80/-1.49/2.10)

145
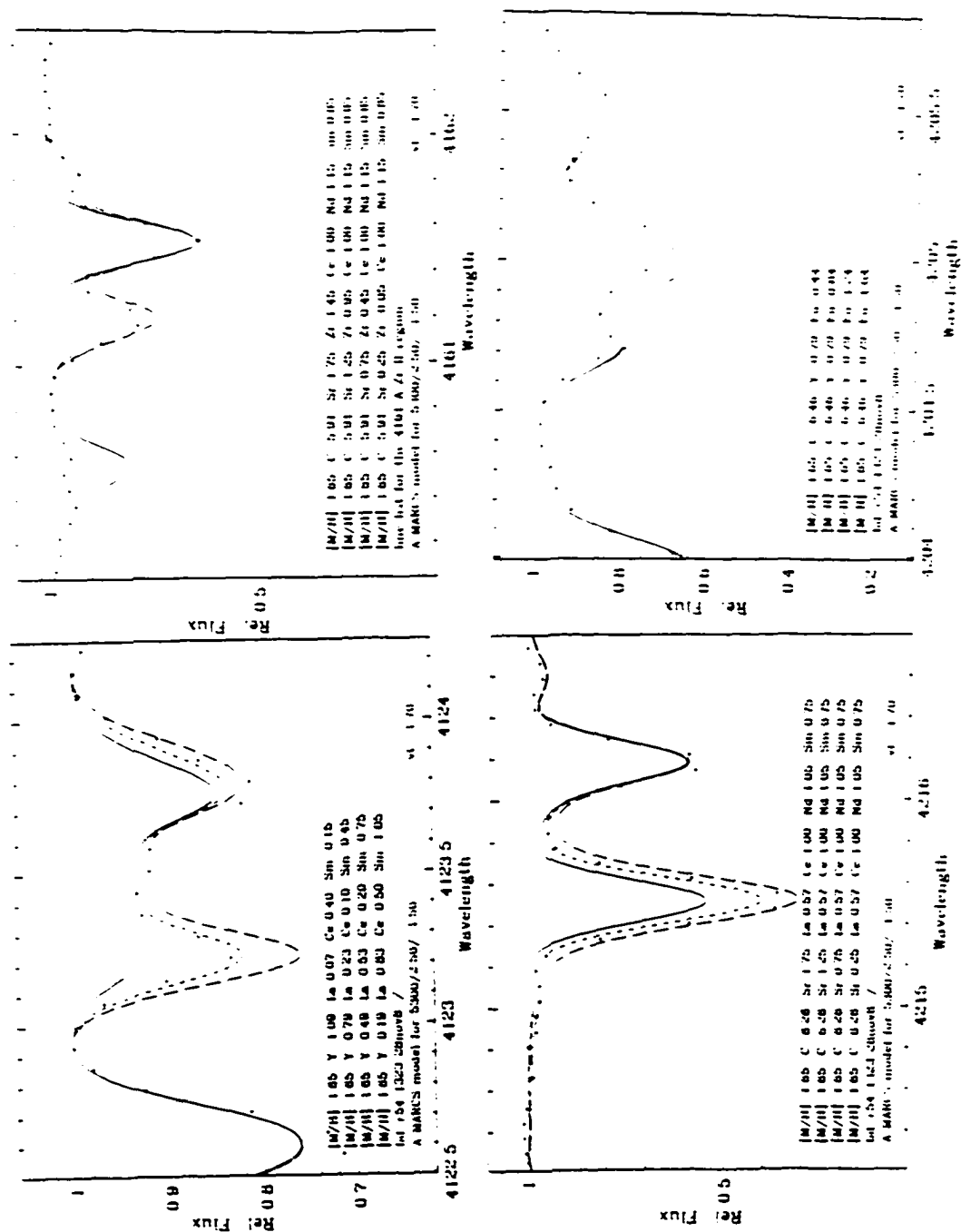
Figure A.2.8 Spectral syntheses for B+541323 (5300/2.50/-1.65/1.70)
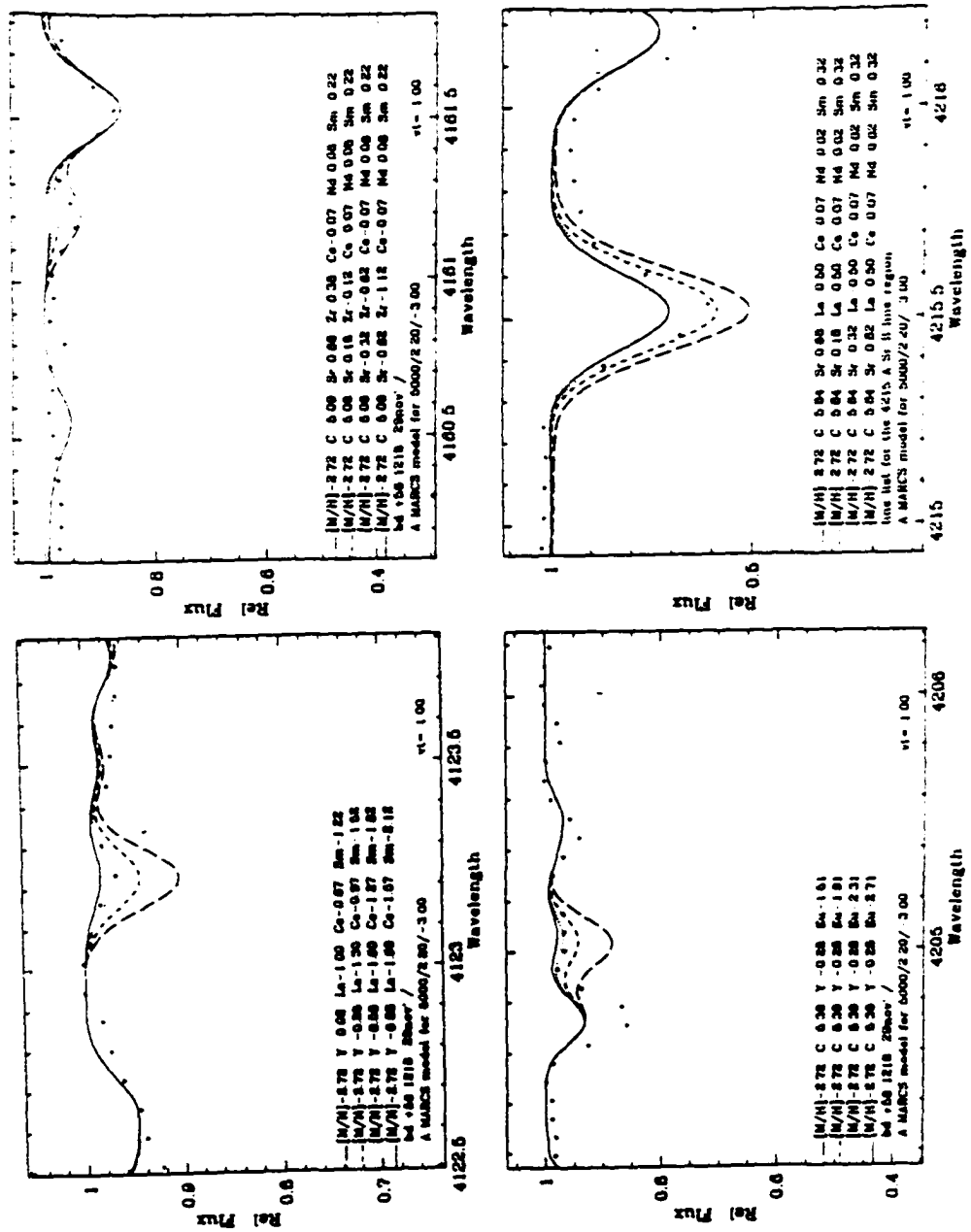
Figure A.2.9 Spectral syntheses for B+581218 (5000/2.20/-2.72/1.00)

147
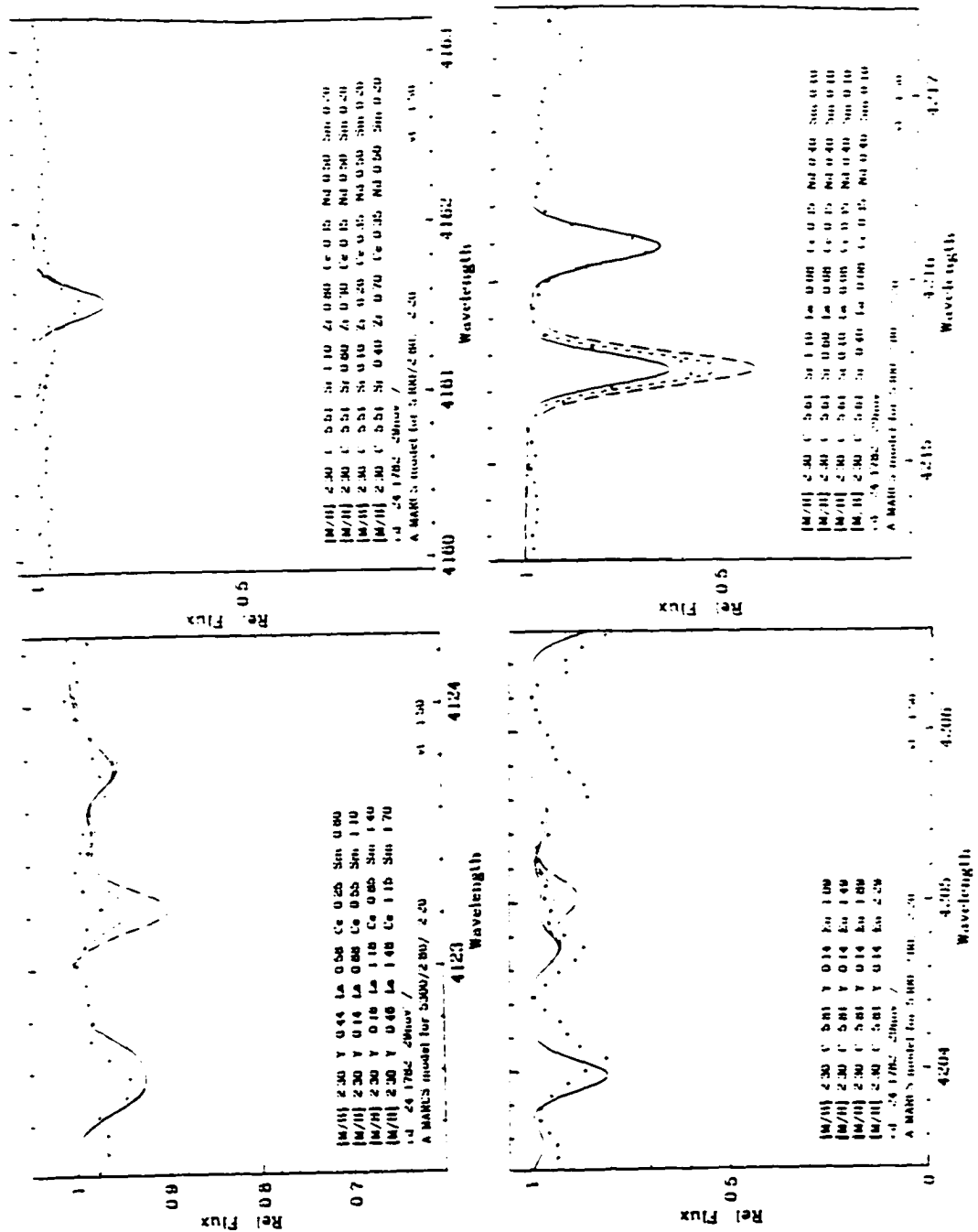
Figure A.2.10 Spectral syntheses for C-241782 (5300/2.80/-2.70/1.50)

Figure A.2.11 Spectral syntheses for HD 20 (5475/2.80/-1.39/2.00)

Figure A.2.12 Spectral syntheses for HD 2665 (5000/2.20/-1.97/1.30)
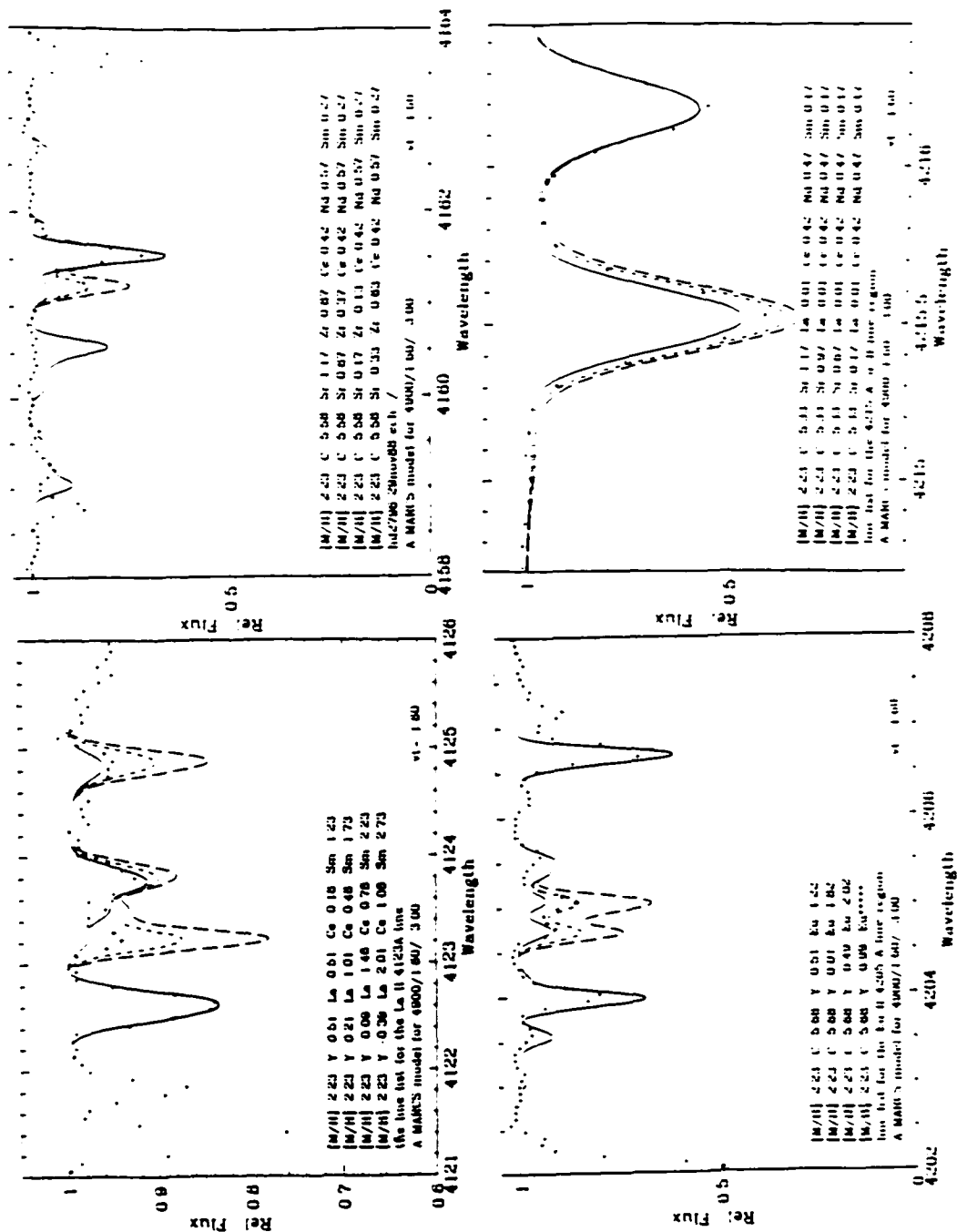
Figure A.2.13 Spectral syntheses for HD 2796 (4900/1.60/-2.23/1.60)
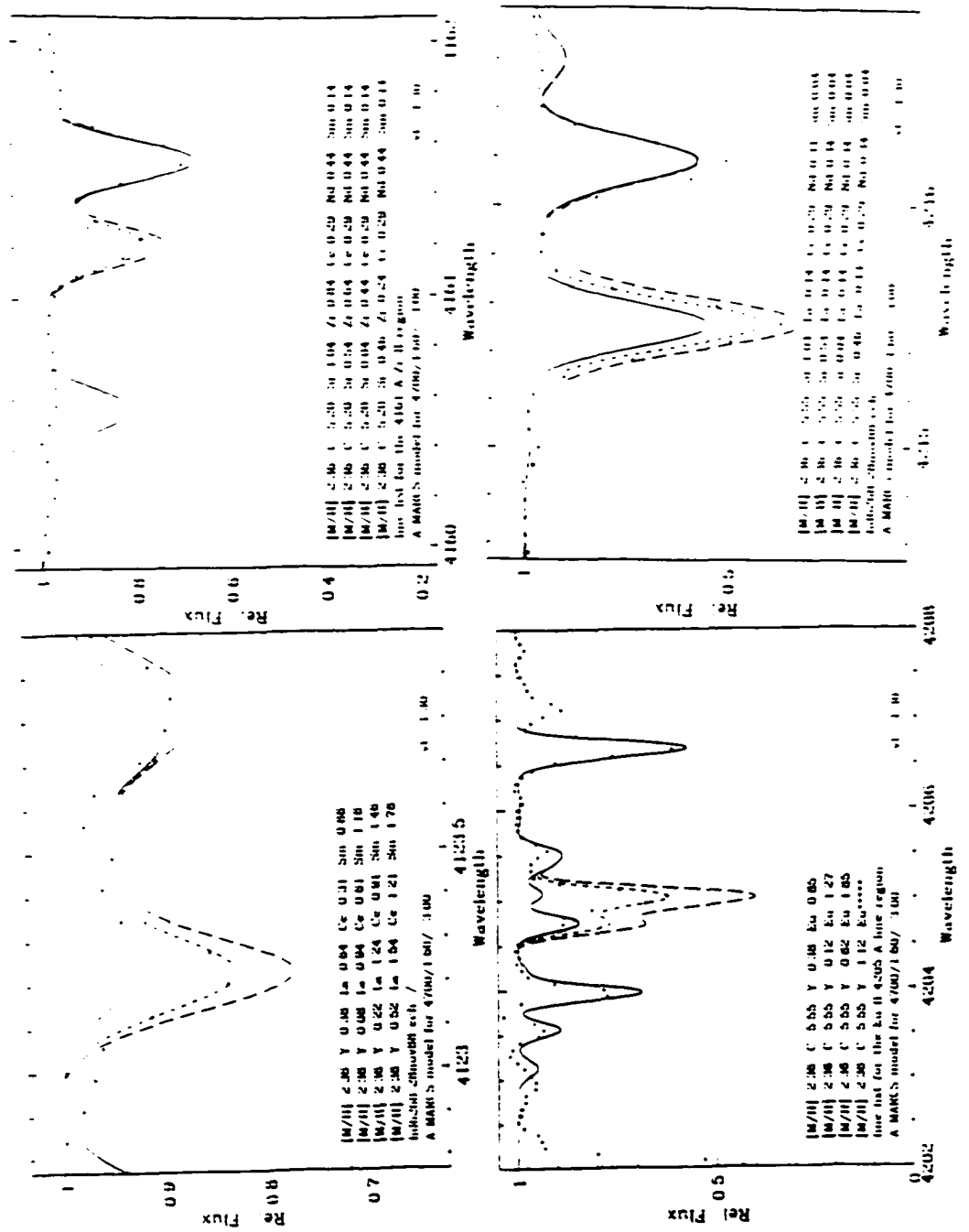
Figure A.2.14 Spectral syntheses for HD 6268 (4700/1.60/-2.36/1.60)
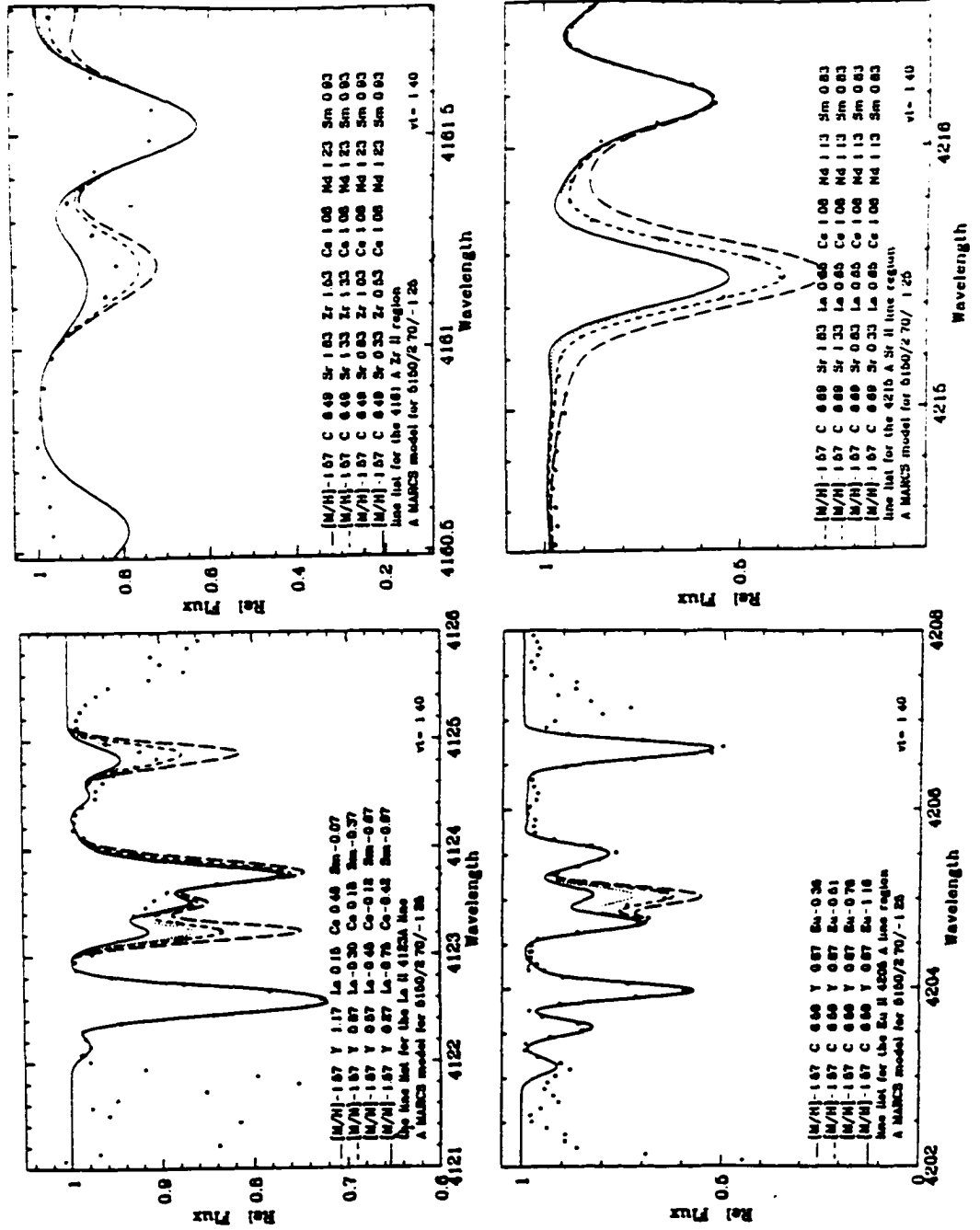
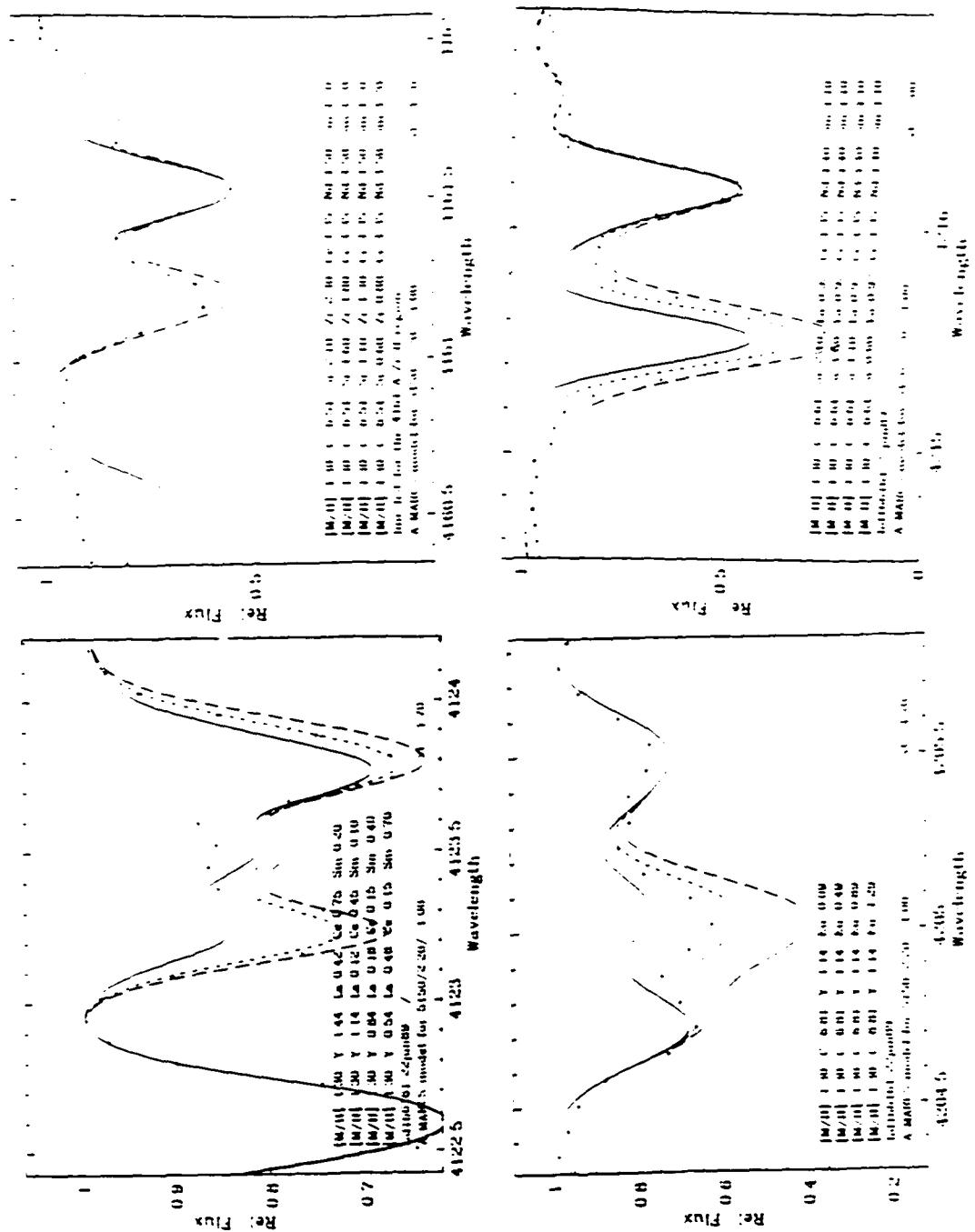Figure A.2.15 Spectral syntheses for HD 6755 (5150/2.70/-1.57/1.40)
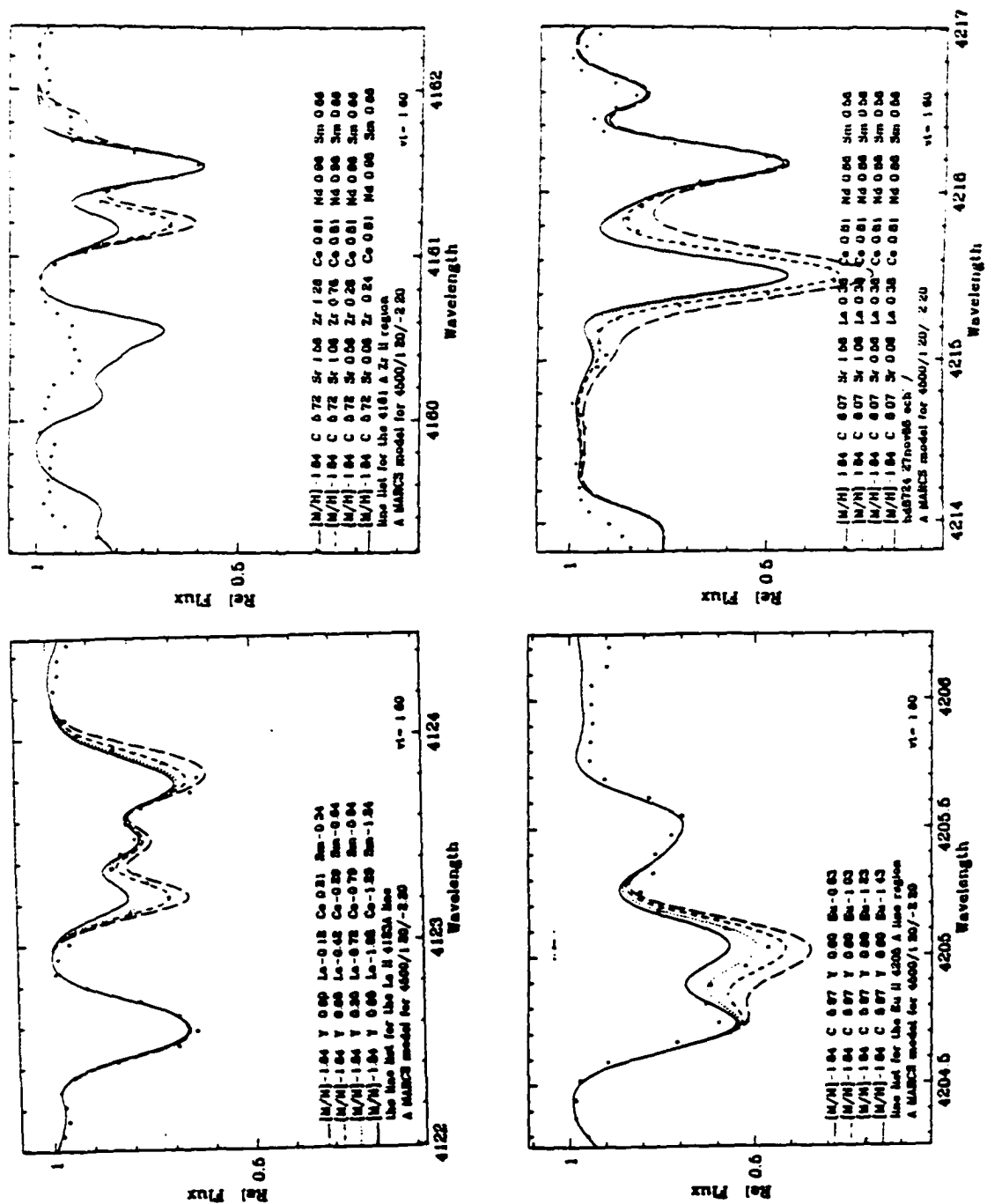
Figure A.2.16 Spectral syntheses for HD 8724 (4500/1.20/-1.84/1.60)
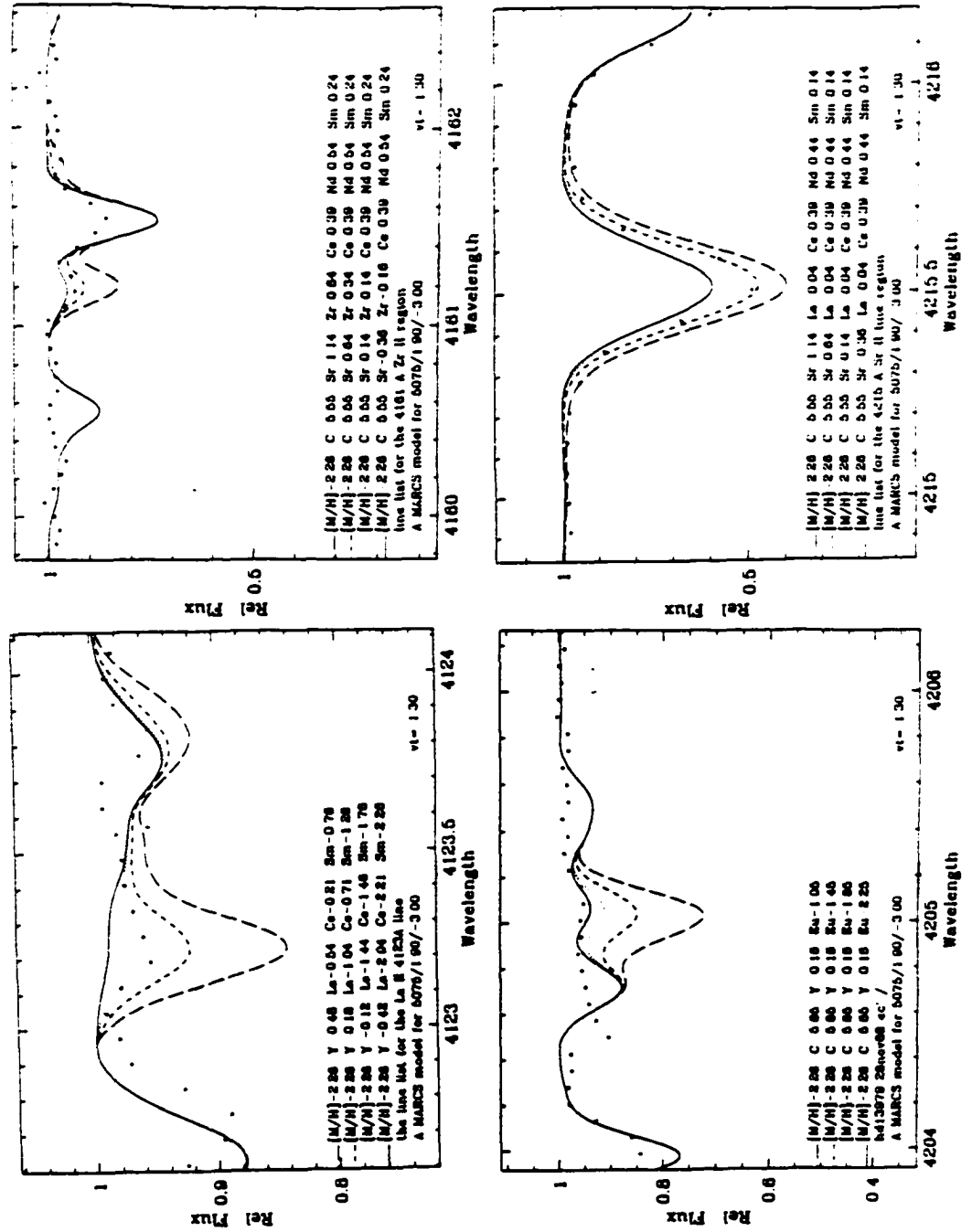
Figure A.2.17 Spectral syntheses for HD 13979 (5075/1.90/-2.26/1.30)

155

Figure A.2.18 Spectral syntheses for HD 25532 (5300/1.90/-1.46/2.30)

156
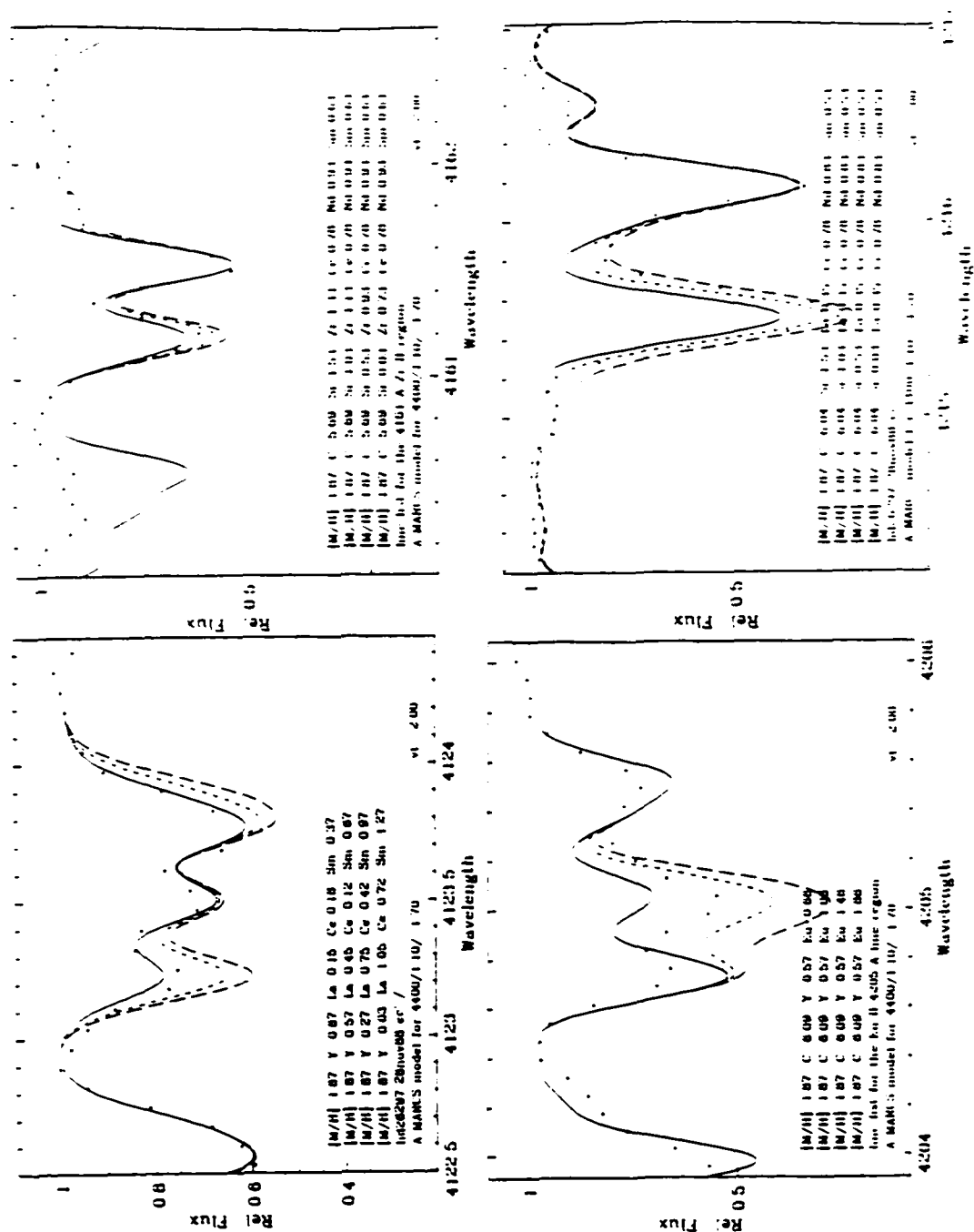
Figure A.2.19 Spectral syntheses for HD 26297 (4400/1.10/-1.87/2.00)
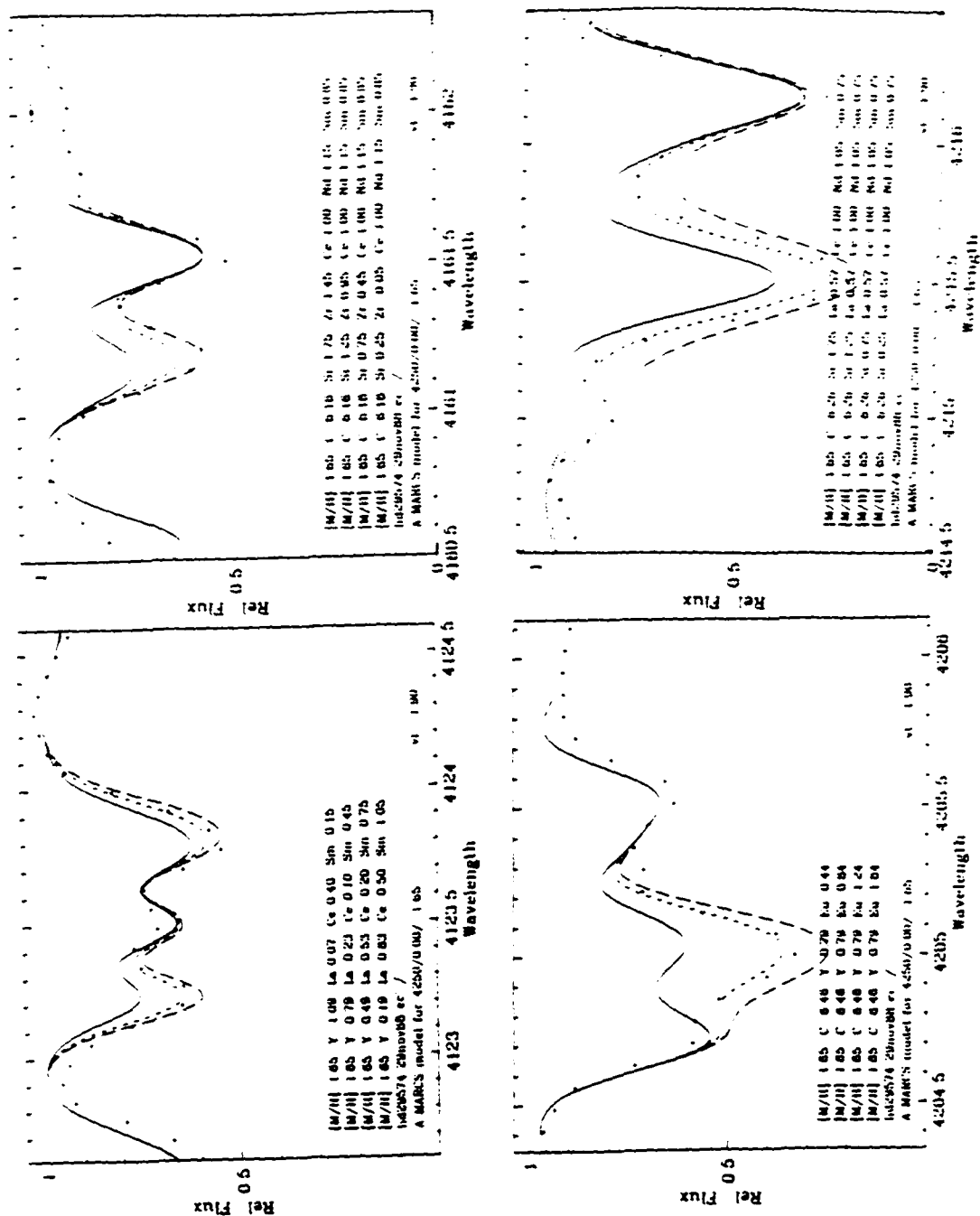
Figure A.2.20 Spectral syntheses for HD 29574 (4250/0.00/-1.81/1.90)
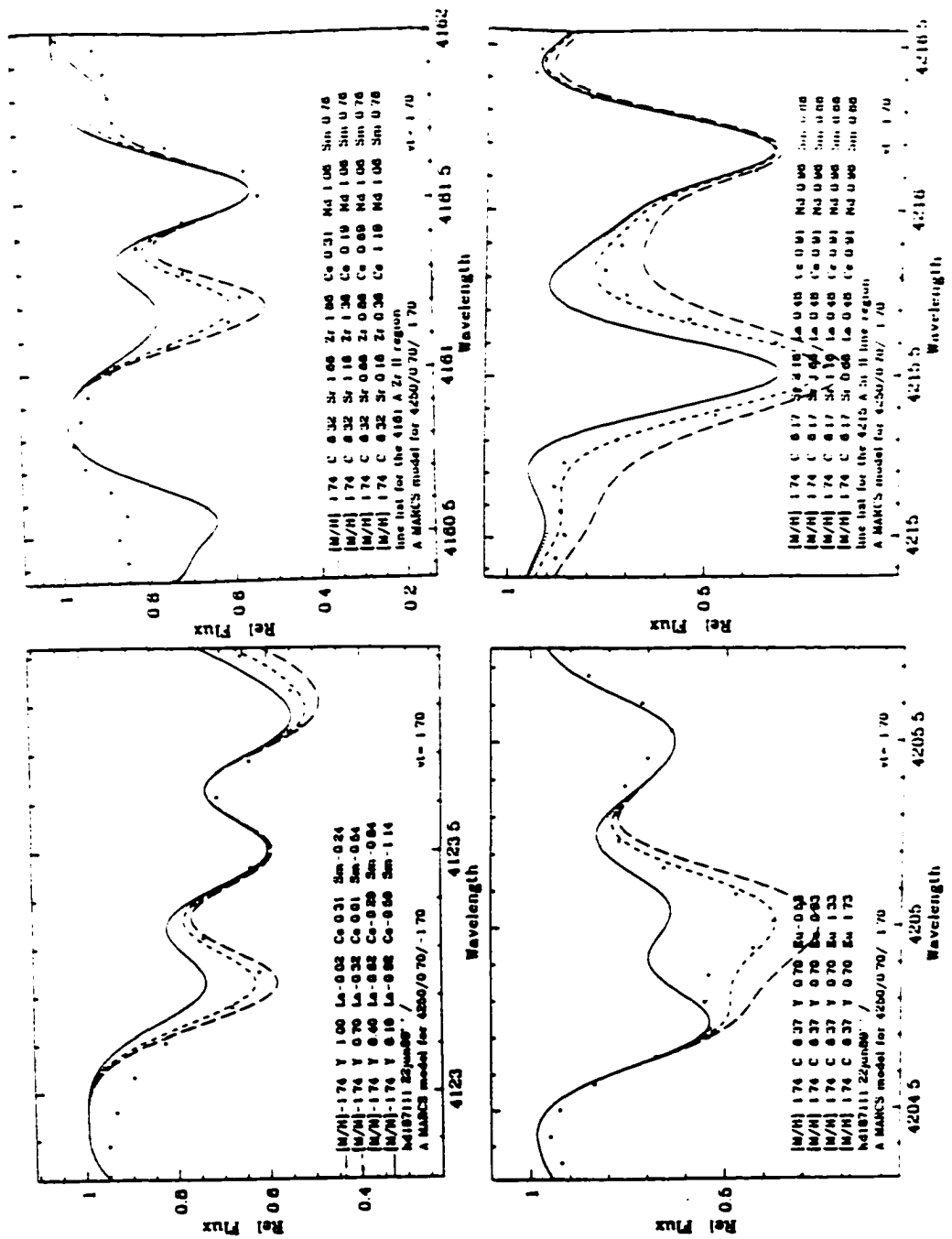
Figure A.2.38 Spectral syntheses for HD 187111 (4250/0.70/-1.74/1.70)
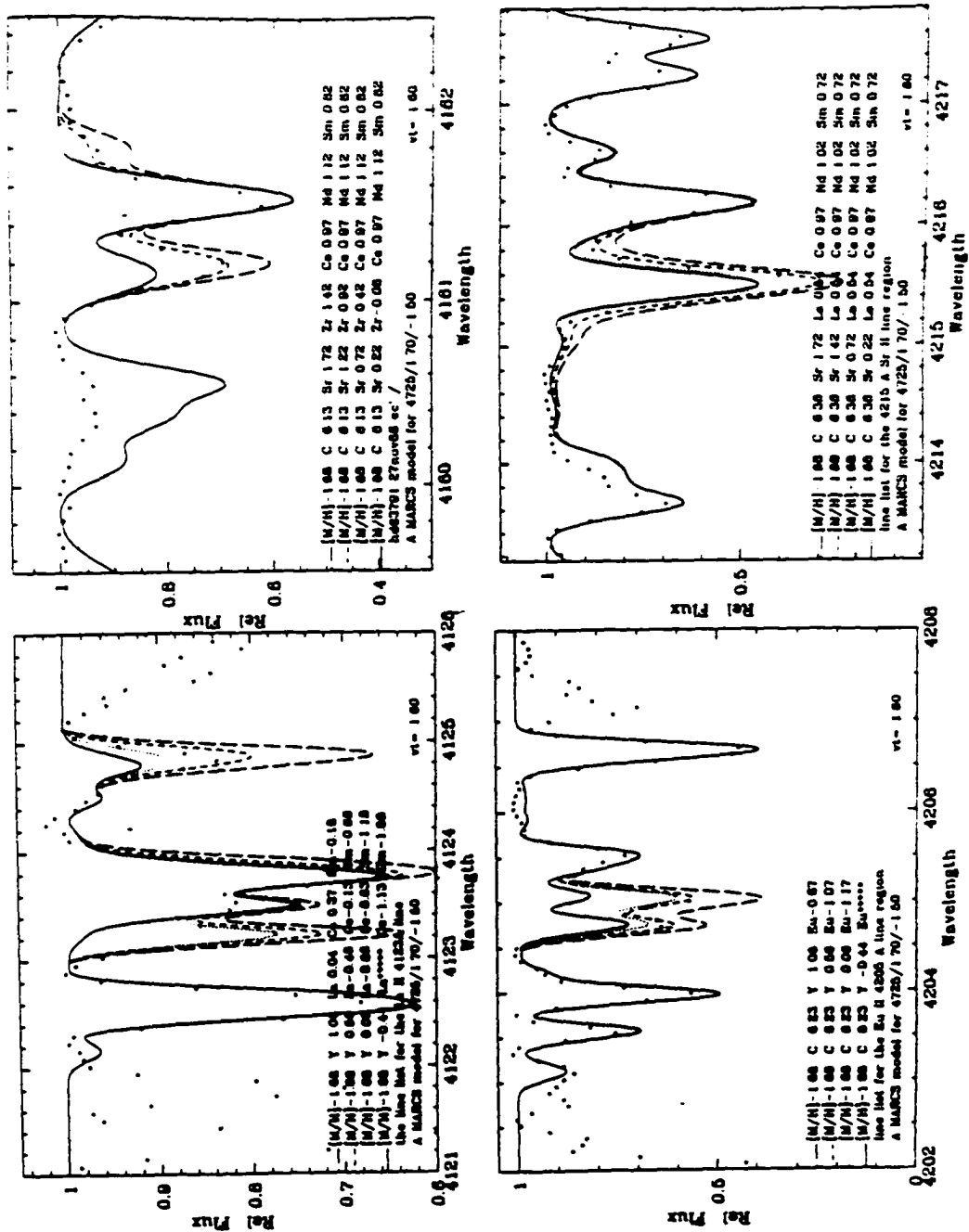
Figure A.2.22 Spectral syntheses for HD 63791 (4725/1.70/-1.68/1.60)
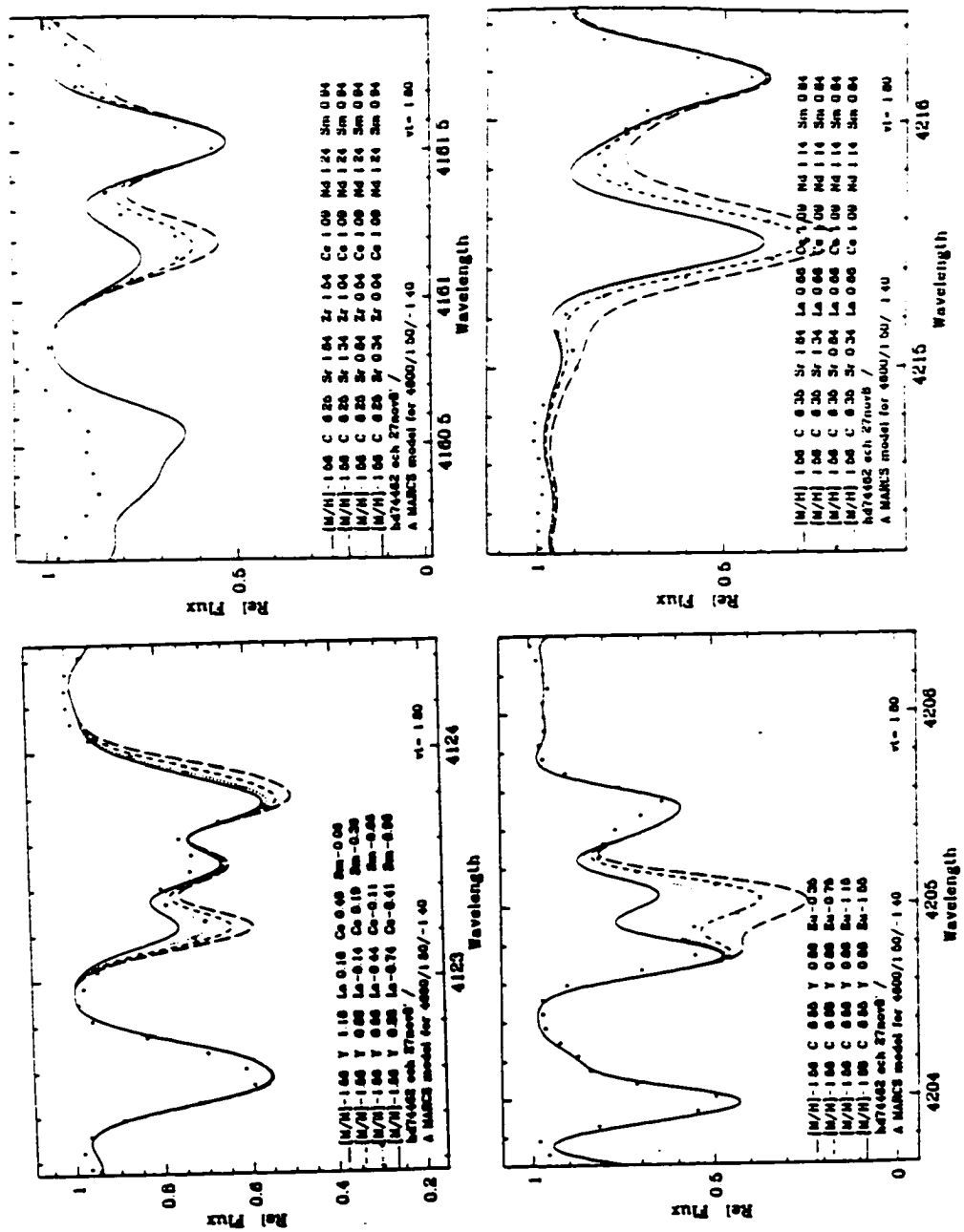
Figure A.2.23 Spectral syntheses for HD 74462 (4600/1.50/-1.56/1.80)
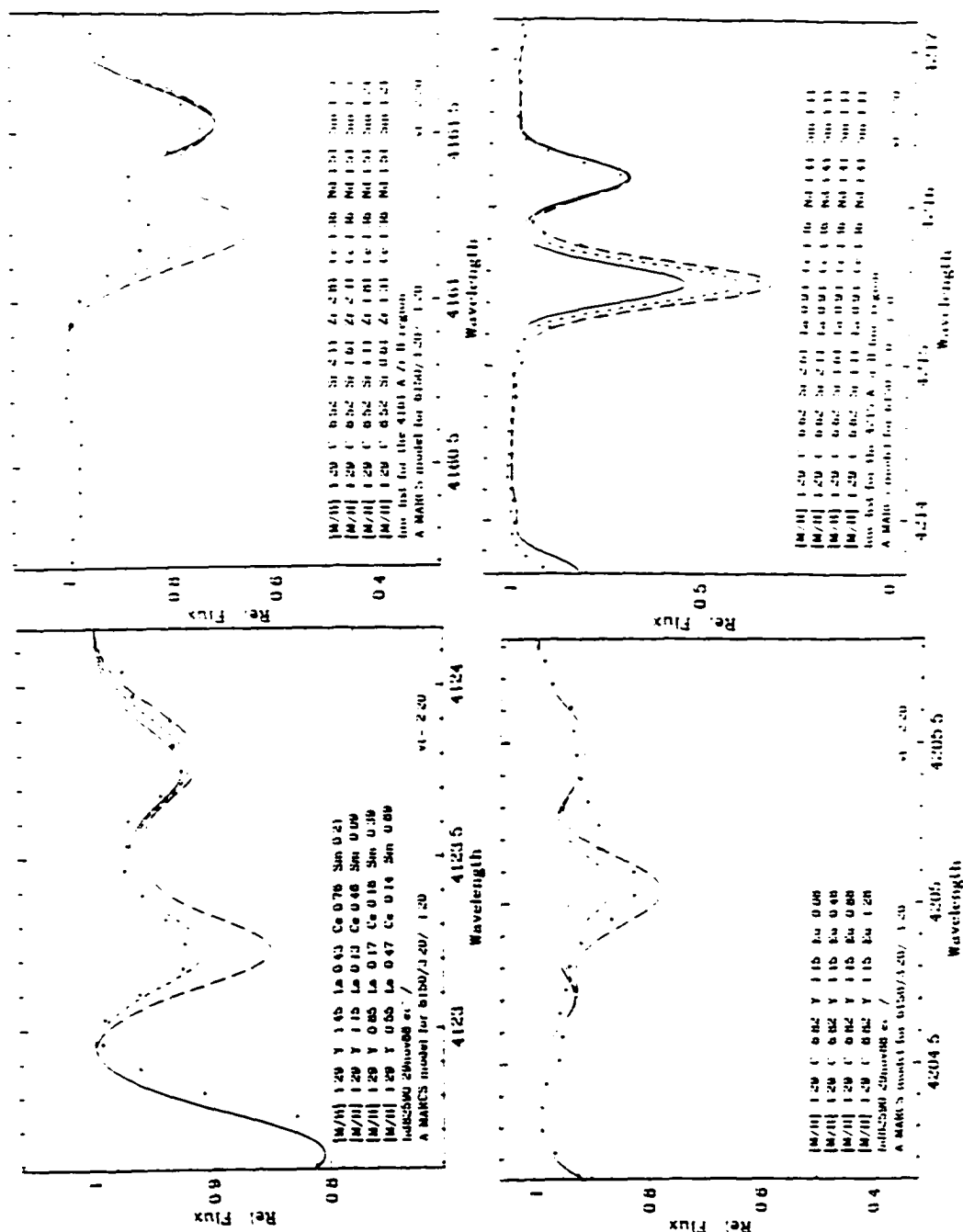
Figure A.2.24 Spectral syntheses for HD 82590 (6150/2.70/-1.32/3.10)

162
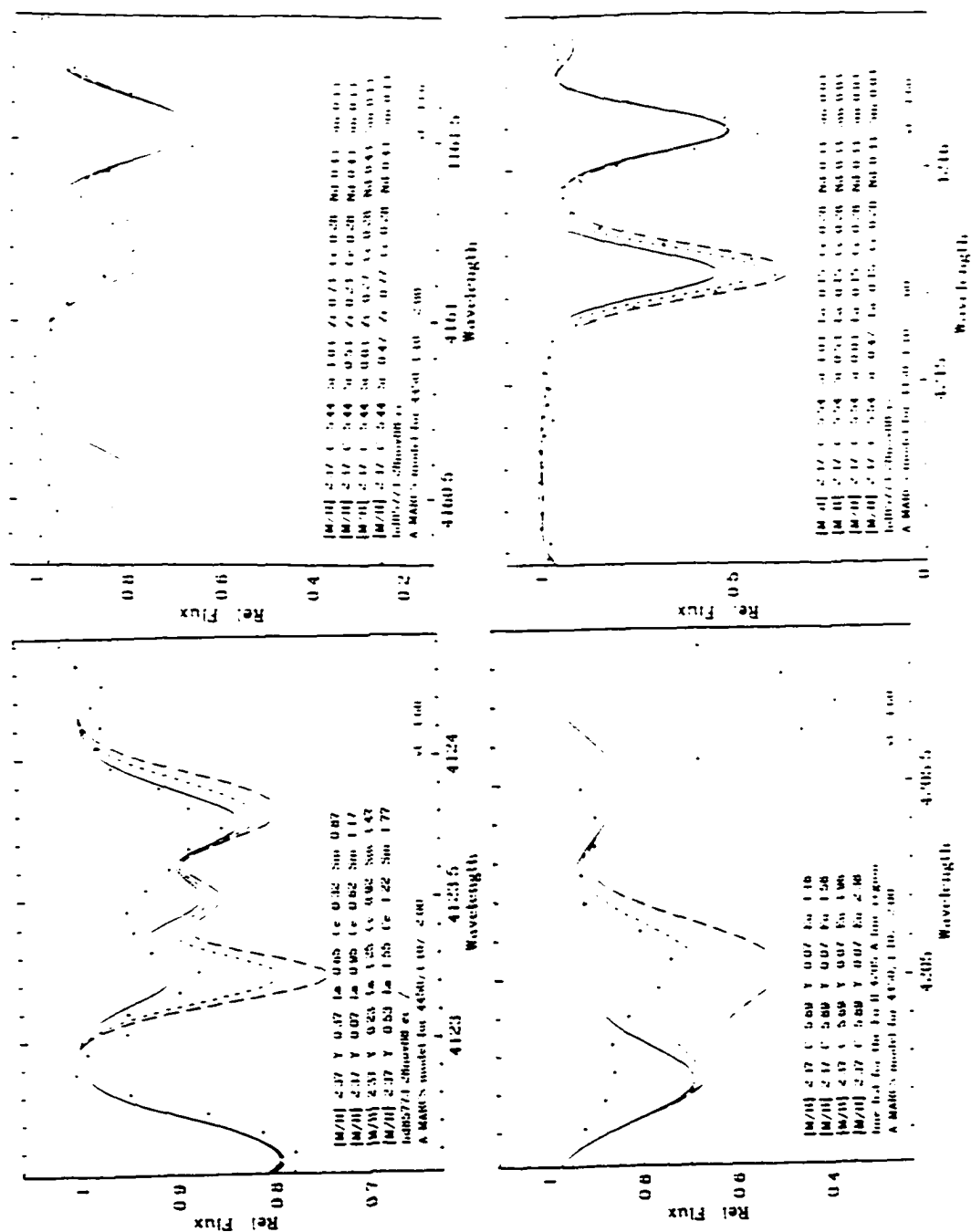
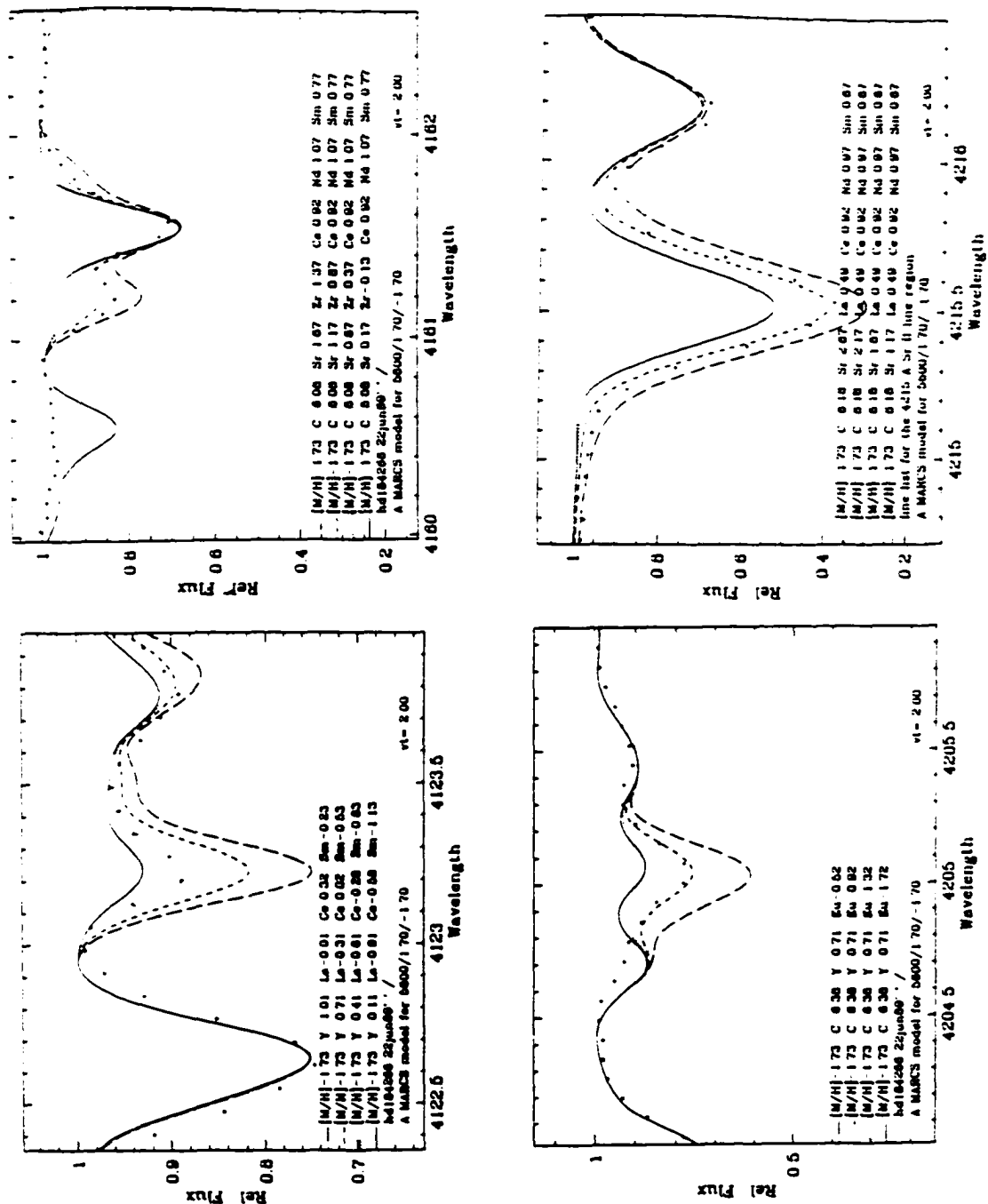Figure A.2.25 Spectral syntheses for HD 85773 (4450/1.10/-2.36/2.10)
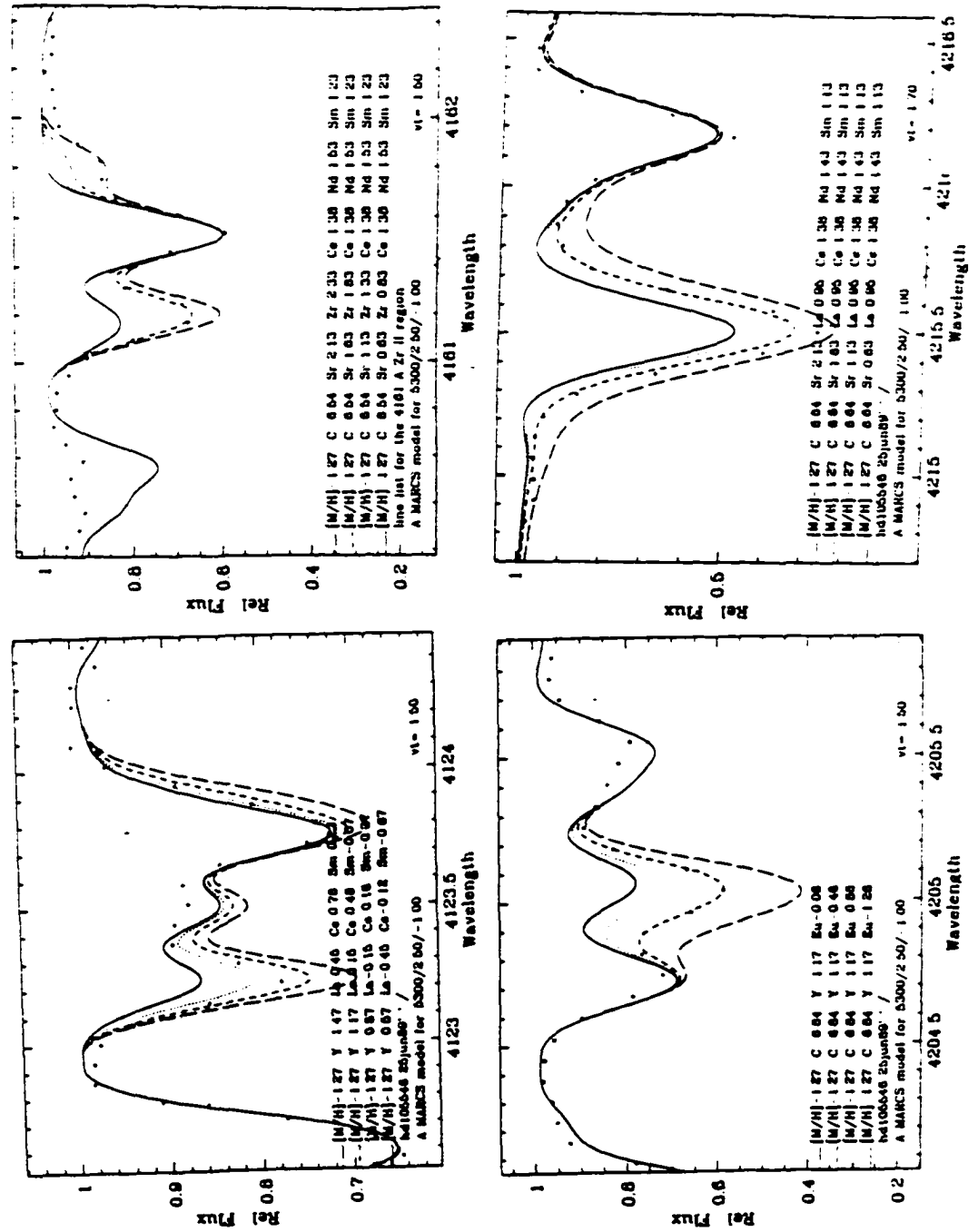
Figure A.2.26 Spectral syntheses for HD 105546 (5300/2.50/-1.27/1.50)

Figure A.2.27 Spectral syntheses for HD 110184 (4250/0.30/-2.56/2.10)

Figure A.2.28 Spectral syntheses for HD 122563 (4625/1.40/-2.71/1.70)

Figure A.2.29 Spectral syntheses for HD 122956 (4600/1.50/-1.78/1.80)
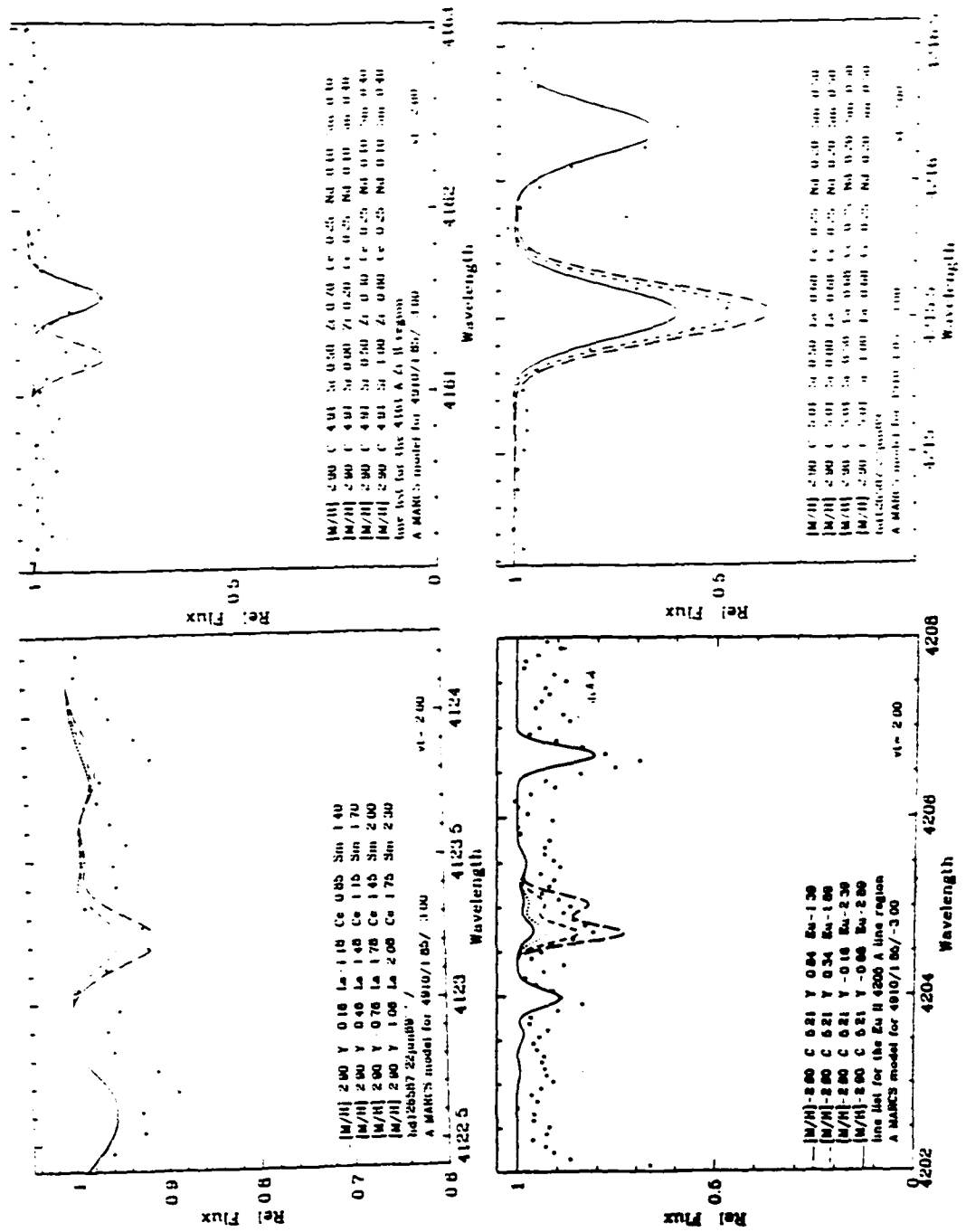
Figure A.2.30 Spectral syntheses for HD 126587 (4910/1.85/-2.85/2.00)

168
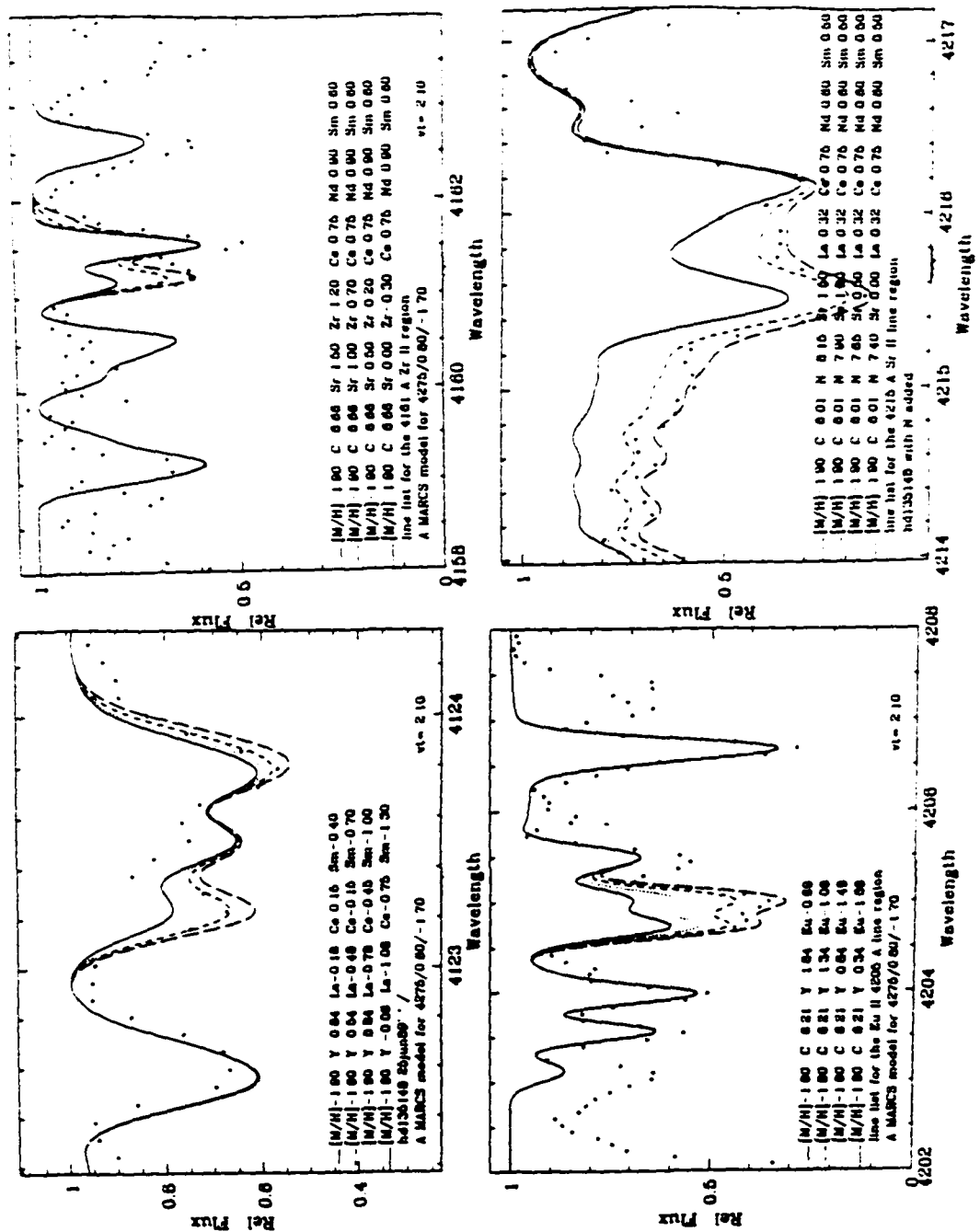
Figure A.2.31 Spectral syntheses for HD 135148 (4275/0.80/-1.90/2.10)
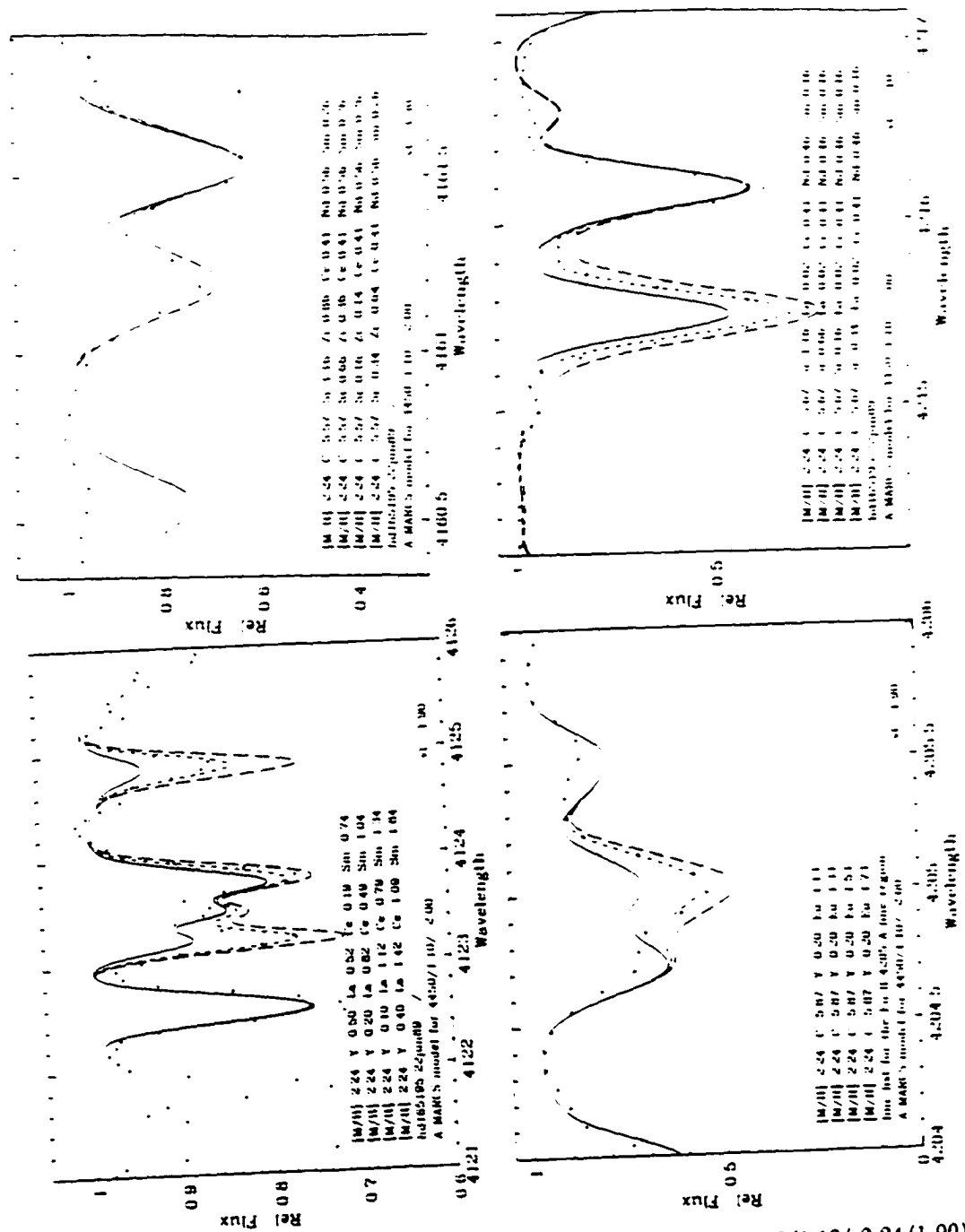
Figure A.2.32 Spectral syntheses for HD 165195 (4450/1.10/-2.24/1.90)

Figure A.2.33 Spectral syntheses for HD 166161 (5150/2.20/-1.30/2.00)

Figure A.2.34 Spectral syntheses for HD 171496 (4700/1.60/-0.91/1.50)
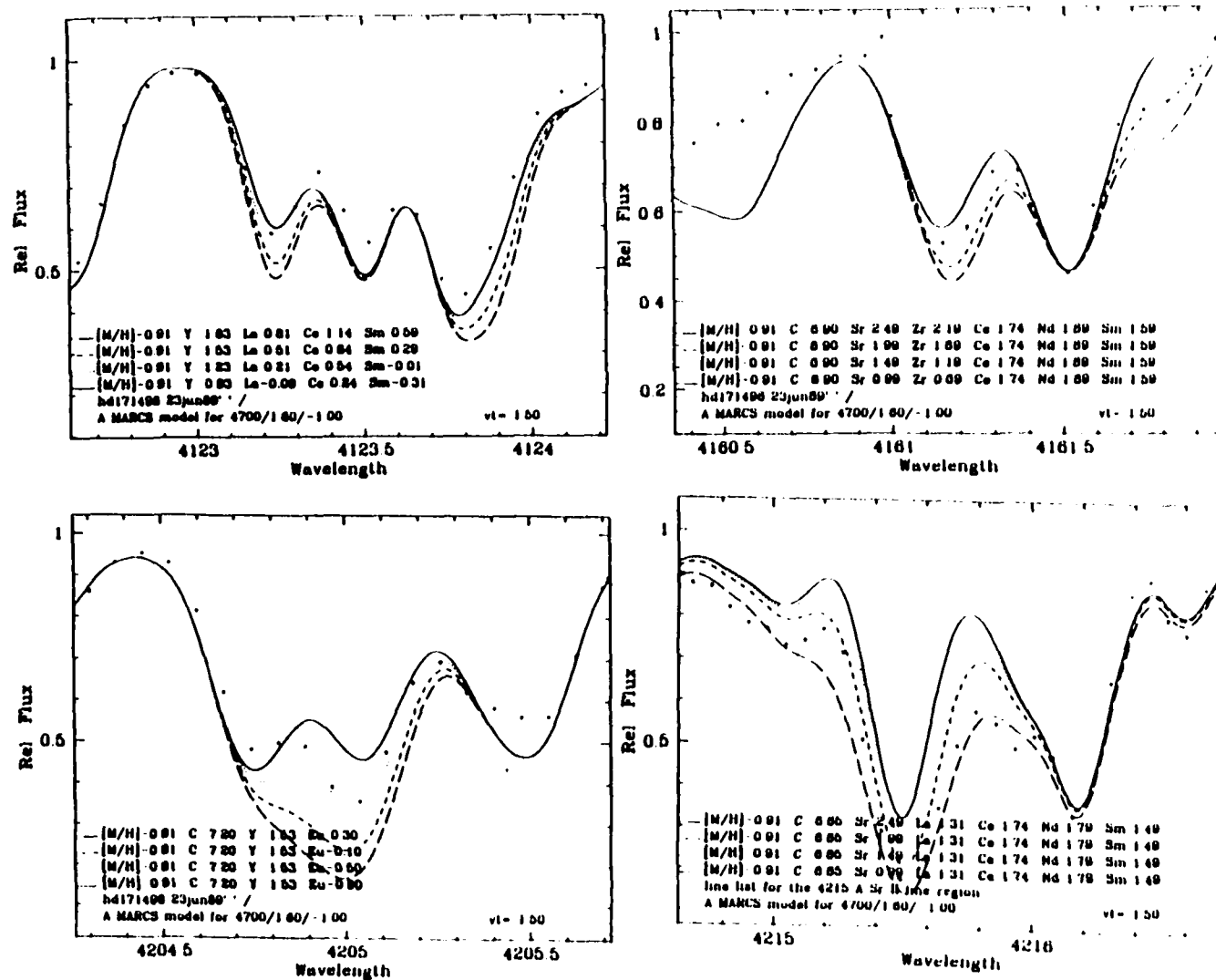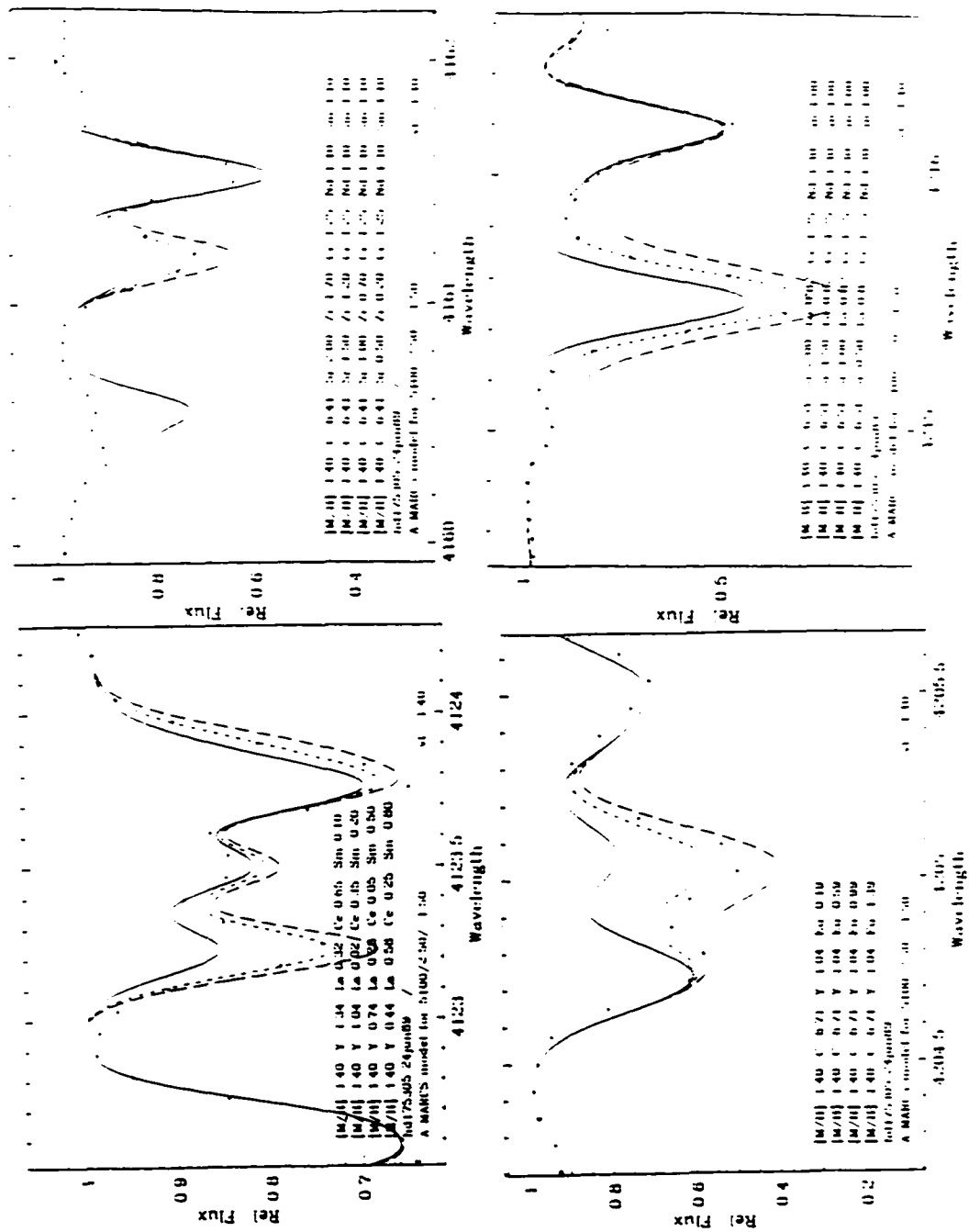
Figure A.2.35 Spectral syntheses for HD 175305 (5100/2.50/-1.40/1.40)

173

Figure A.2.36 Spectral syntheses for HD 184266 (5600/1.70/-1.73/2.00)
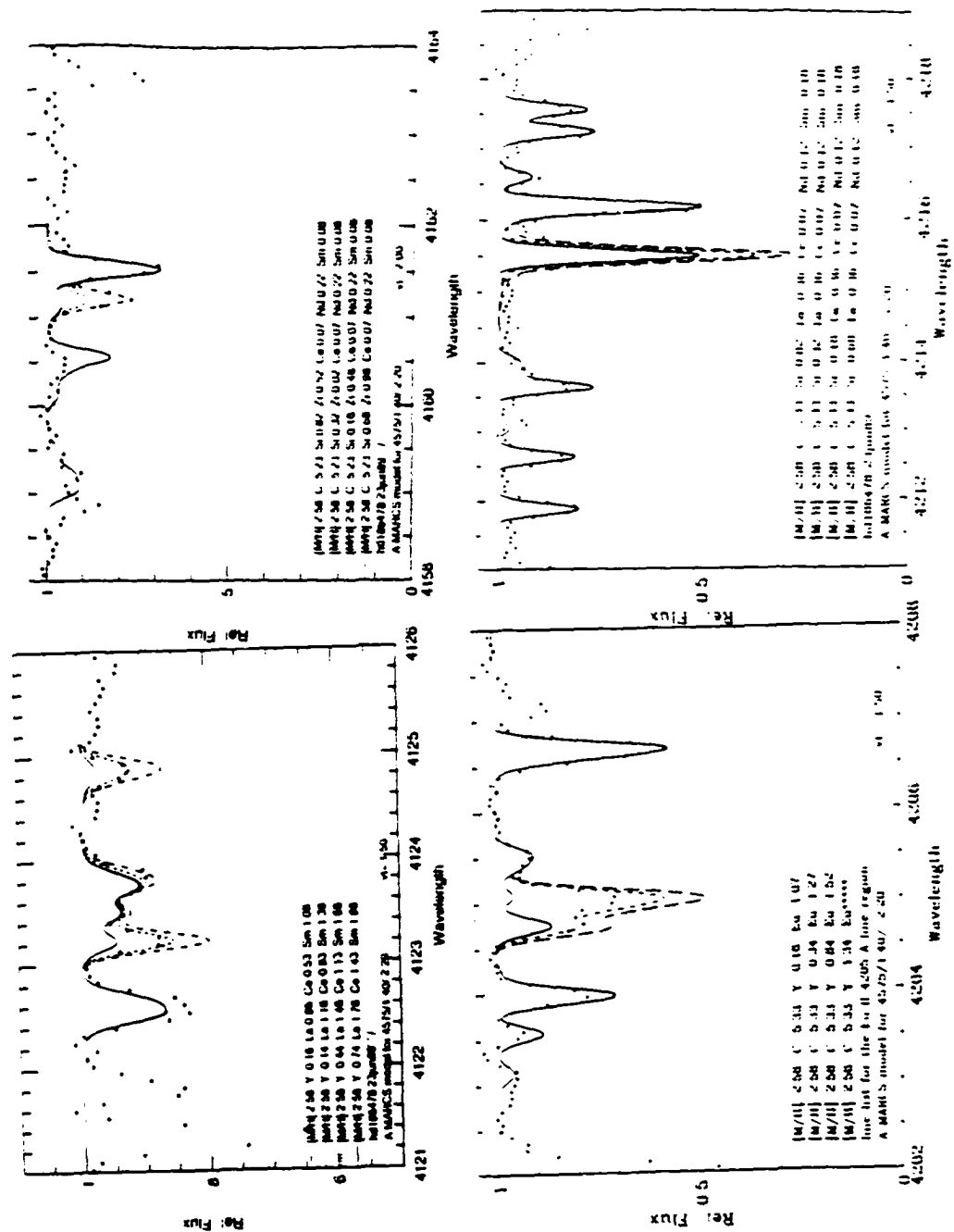
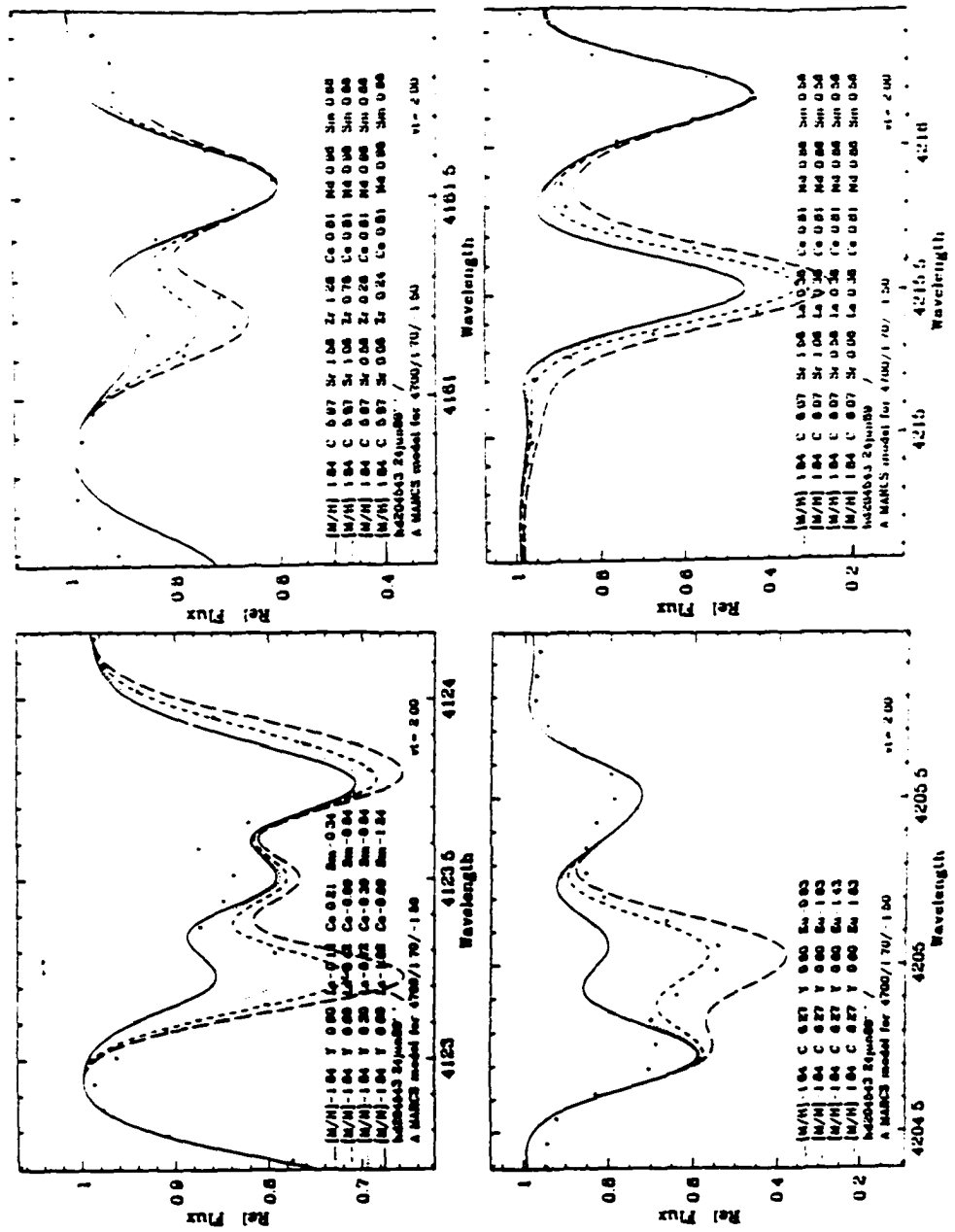Figure A.2.37 Spectral syntheses for HD 186478 (4575/1.40/-2.58/2.00)

Figure A.2.38 Spectral syntheses for HD 187111 (4250/0.70/-1.74/1.70)

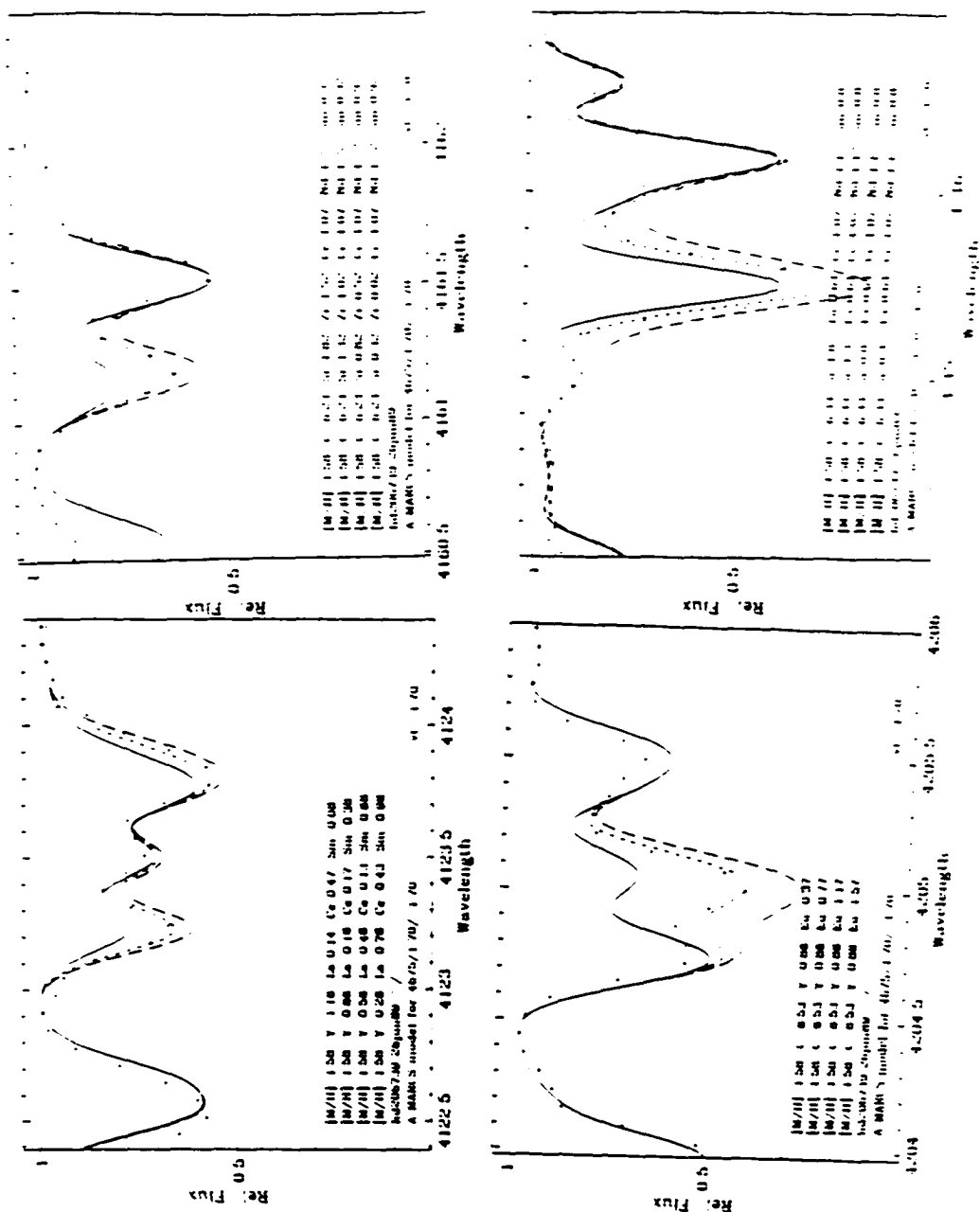Figure A.2.39 Spectral syntheses for HD 204543 (4700/1.70/-1.84/2.00)

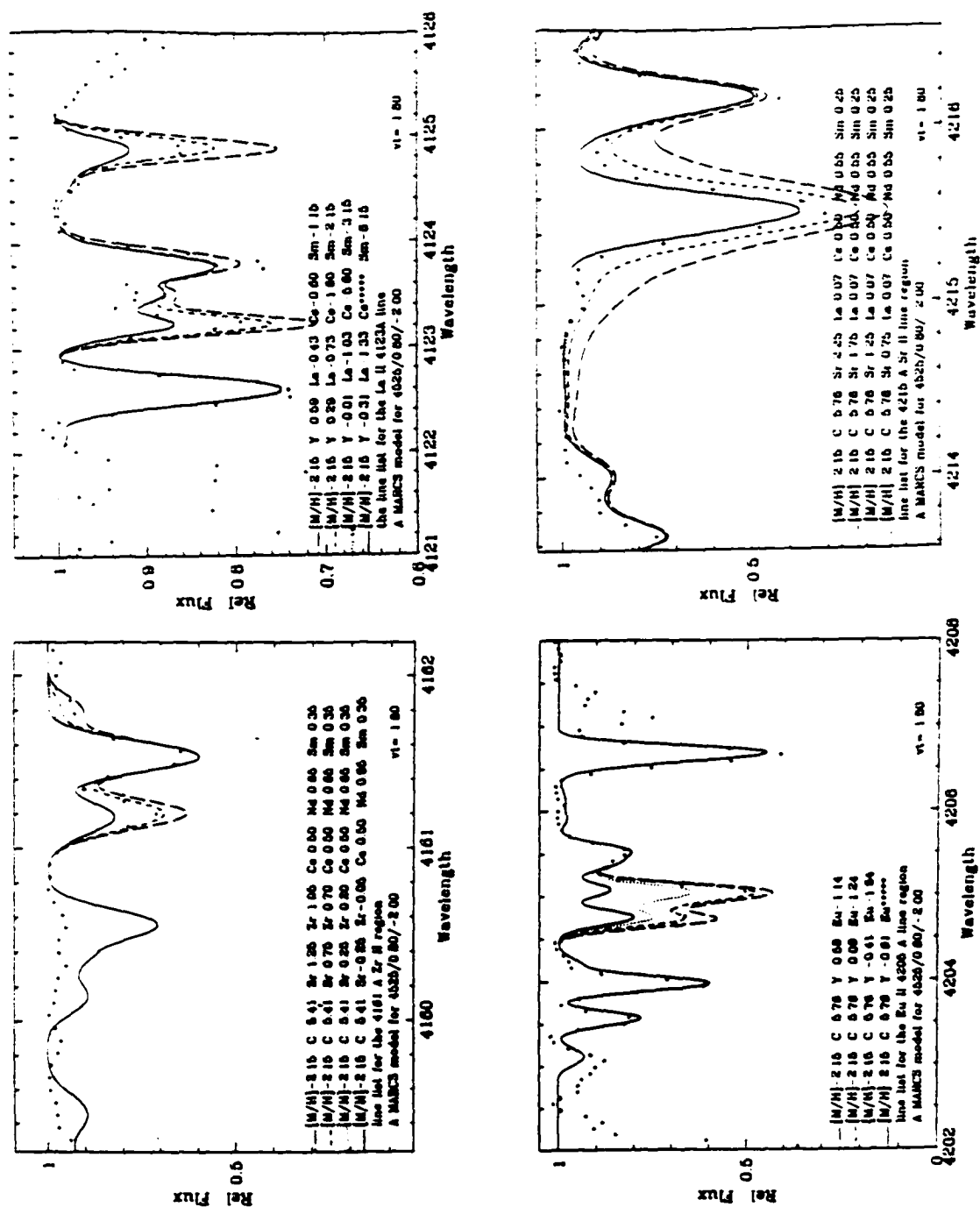Figure A.2.40 Spectral syntheses for HD 206739 (4675/1.70/-1.58/1.70)

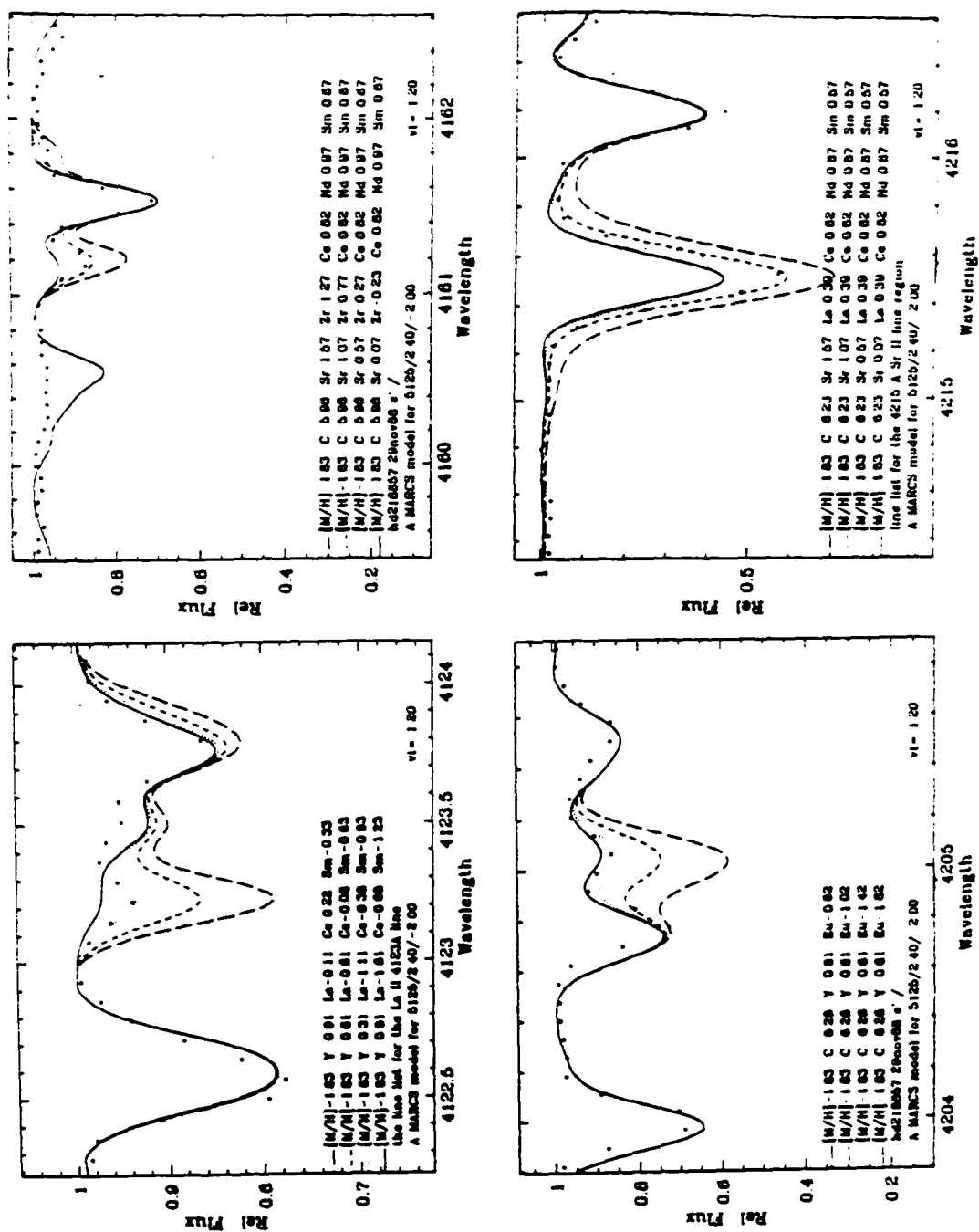Figure A.2.41 Spectral syntheses for HD 216143 (4525/0.80/-2.18/1.80)

Figure A.2.42 Spectral syntheses for HD 218857 (5125/2.40/-1.86/1.20)

Figure A.2.43 Spectral syntheses for HD 220838 (4450/1.20/-1.65/1.90)

Figure A.2.44 Spectral syntheses for HD 221170 (4425/1.00/-2.15/1.50)

Figure A.2.45 Spectral syntheses for HD 232078 (4000/0.30/-1.54/2.60)